# Structural insights into the activation mechanism of the EHD family

Inaugural Dissertation to obtain the academic degree
Doctor of Philosophy (Ph.D)

Submitted to the Department of Biology, Chemistry and Pharmacy
of Freie Universität Berlin

Arthur Melo
born in Brasília-DF/Brazil

Berlin
2017

The present work was carried out between September 2013 and September 2017 at the Max-Delbrück-Center for Molecular Medicine (MDC-Berlin) under the supervision of Prof. Dr. Oliver Daumke.

1. Reviewer: Prof. Dr. Oliver Daumke, Department of Protein Crystallography, Max-Delbrück-Center for Molecular Medicine

2. Reviewer: Prof. Dr. Udo Heinemann, Department of Protein Crystallography, Max-Delbrück-Center for Molecular Medicine

Date of defense: 18.01.2018

# Publication

Part of this PhD thesis has been published in the following manuscript:

**Structural insights into the activation mechanism of dynamin-like EHD ATPases.**

**Melo, A.A.**, Hegde, B.G., Shah, C., Larsson, E., Isas, J.M., Kunz, S., Lundmark, R., Langen, R., and Daumke, O. (2017).

Proceedings of National Academy of Sciences of the United States of America. 114, 5629–5634.

http://doi.org/10.1073/pnas.1614075114

Table of Contents

# 1 Introduction

## 1.1 Biological membranes

Biological membranes comprise an asymmetrical bilayer composed mainly of phospholipids and proteins (Nickels et al., 2015). Eukaryotic as well as prokaryotic cells have their cytoplasm surrounded by the plasma membrane, which separates intracellular components from the environment (Watson, 2015). In contrast, intracellular membranes are particularly important in eukaryotic cells which possess a nucleus and membranous organelles (Fig. 1) (Adl et al., 2012). An extensive network of intracellular membranes functions in protein and membrane sorting, processing and transporting cargoes within vesicles to the plasma membrane and to other compartments (Fig. 1) (Watson, 2015).

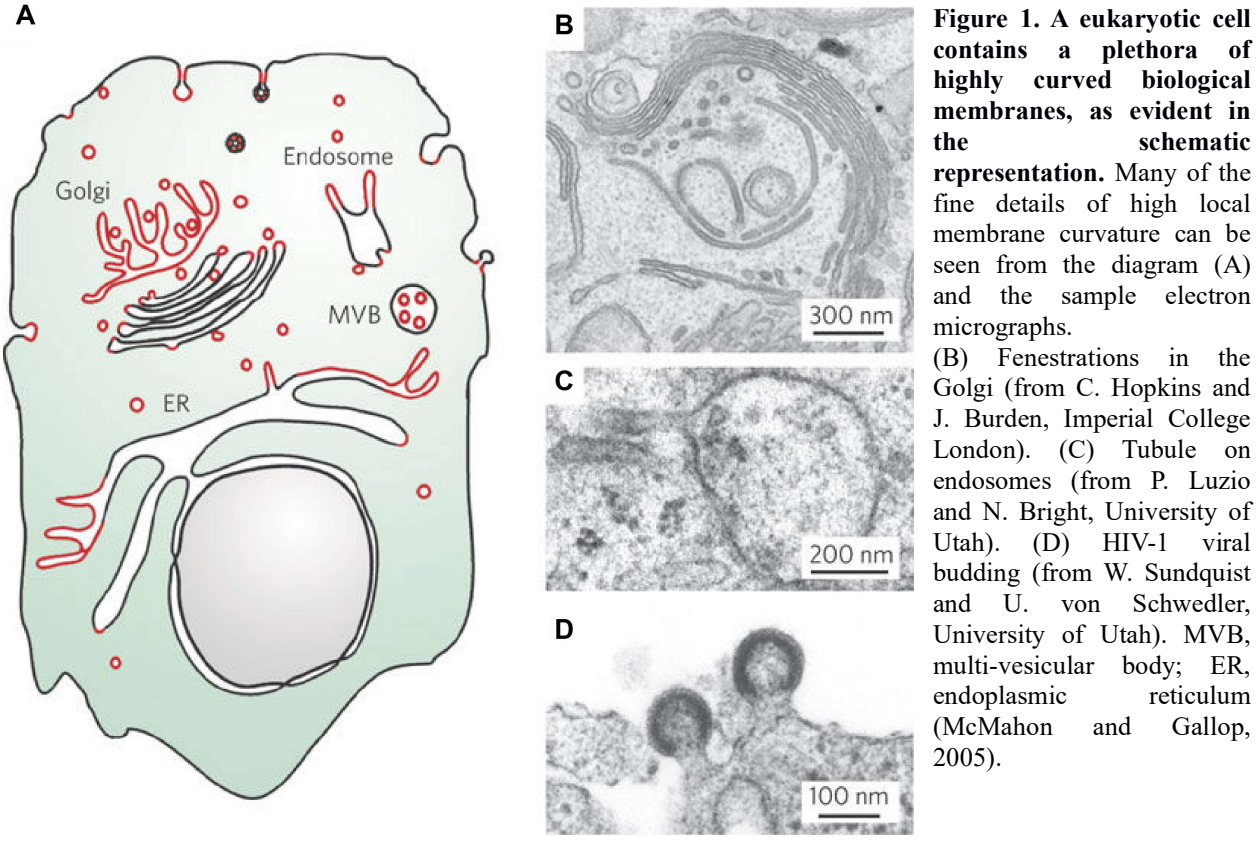


**Figure 1. A eukaryotic cell contains a plethora of highly curved biological membranes, as evident in the schematic representation.** Many of the fine details of high local membrane curvature can be seen from the diagram (A) and the sample electron micrographs. (B) Fenestrations in the Golgi (from C. Hopkins and J. Burden, Imperial College London). (C) Tubule on endosomes (from P. Luzio and N. Bright, University of Utah). (D) HIV-1 viral budding (from W. Sundquist and U. von Schwedler, University of Utah). MVB, multi-vesicular body; ER, endoplasmic reticulum (McMahon and Gallop, 2005).

Cargo transport occurs mainly through the trafficking of membrane vesicles between different organelles within the cell (Fig. 1) (Ross et al., 2008). During this process, membrane remodeling events, such as membrane deformation, fission and fusion, play a critical role (Bonifacino and Glick, 2004). These events rely on protein machineries that are recruited to the target membrane, assemble into scaffolds and execute the membrane deformation process (Bonifacino and Glick, 2004). For example, when vesicles exit certain organelles, a plethora of proteins is recruited to generate the necessary curvature so that membrane fission can occur (Bonifacino and Glick, 2004). At the end of a vesicle path, membranous structures can undergo fusion in order to deliver cargo to the correct compartment (Jahn et al., 2003). These membrane remodeling events rely on many different proteins involved in the recruitment, assembly, and activation of numerous proteins that catalyze membrane fission and/or fusion (Bonifacino and Glick, 2004). Proteins from the dynamin superfamily play a major role in various membrane deformation events (Antonny et al., 2016; Praefcke and McMahon, 2004).

## 1.2 The dynamin superfamily - Cellular and biochemical features

Proteins from the dynamin superfamily are multidomain mechano-chemical GTPases which are implicated in nucleotide-dependent membrane remodeling events (Fig. 2) (Daumke and Praefcke, 2016). Classical dynamins function in the budding of clathrin-coated vesicles (CCVs) at the plasma membrane, cleavage furrow, Golgi and endosome, but also in non-clathrin-mediated budding events at caveolae and phagosomes (Praefcke and McMahon, 2004). Dynamin has three isoforms in mammals: dynamins 1, 2 and 3. Dynamin 1 and 3 are highly expressed in neurons, whereas dynamin 2, is ubiquitously expressed (Cook et al., 1996, 1994). The isoforms mediate cleavage of CCVs for various cellular functions, for example, the recycling of synaptic vesicles in neurons or the uptake of nutrients or signaling factors in almost all other cell types (Praefcke and McMahon, 2004). Dynamin-related proteins (DRPs) are involved in division of organelles such as mitochondria and peroxisomes (McBride and Frost, 2016). OPA1 (optic atrophy 1) and mitofusin are involved in the fusion of the inner and outer mitochondrial membranes, respectively (Cao et al., 2017; Liu and Chan, 2017).

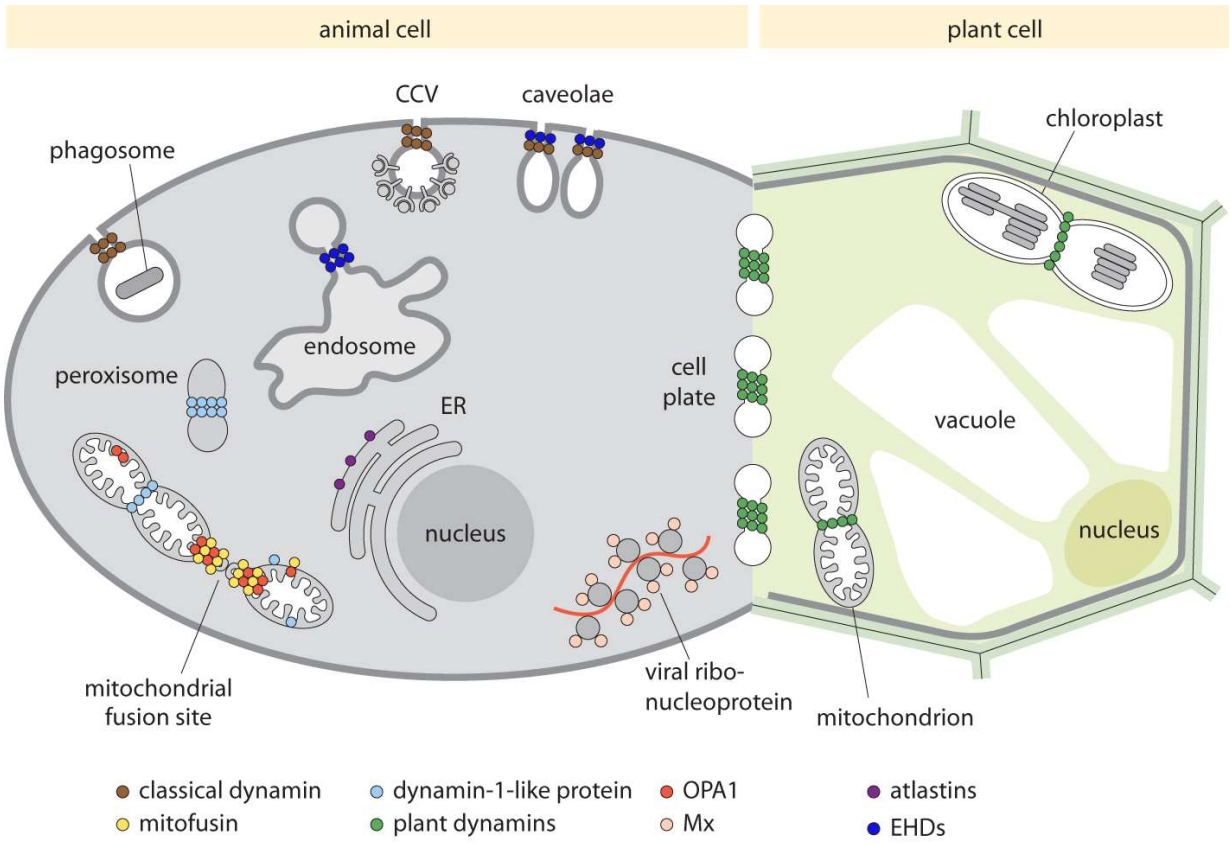


**Figure 2. Dynamin superfamily proteins: Cellular localization and function.** Figure modified from (Steven et al., 2016)

The Mx (Myxovirus-resistance protein) family are induced by interferons and confer resistance against RNA viruses (Haller and Kochs, 2011). In non-infected cells, human MxA localizes to the smooth endoplasmic reticulum, but upon infection, it is thought to interact with viral ribonucleoproteins (Haller and Kochs, 2011). Atlastin tethers and fuses endoplasmic reticulum (ER) tubules stabilized by the reticulons and transiently localizes to newly formed three-way junctions at the ER (Wang et al., 2016). Proteins from the EHD (Eps15-homology domain) family are involved in the regulation of membrane trafficking at caveolae and endosomes (Naslavsky and Caplan, 2011). Plants contain many different dynamin proteins, which are involved in the budding of CCVs, formation of the cell plate or chloroplast division (Fig. 2) (Praefcke and McMahon, 2004).

Dynamin is the best characterized member of the dynamin superfamily. It is recruited as a tetramer from the cytosol to the target membrane, where it oligomerizes into ring-like or helical

structures (Hinshaw and Schmid, 1995). These helical structures stabilize high membrane curvature. Once oligomerized on a suitable membrane template, the basal GTPase activity of dynamin is stimulated up to 200-fold (Stowell et al., 1999). Stimulated GTP hydrolysis in the dynamin oligomer induces conformational changes ultimately resulting in vesicle fission (see later) (Marks et al., 2001; Roux et al., 2006; Sweitzer and Hinshaw, 1998)

Many of the biochemical features identified for dynamins, such as oligomerization at the membrane and membrane-stimulated GTPase activity, have been also found in other members of the family. Importantly, structural studies on dynamin superfamily proteins have helped to elucidate the underlying molecular mechanisms, as outlined in the following.

### 1.2.1 Structural organization of dynamin superfamily proteins

Based on sequence and structure comparisons, five distinct domains have been described in classical dynamins: an N-terminal GTPase domain, a stalk domain, a bundle signaling element (BSE), a Pleckstrin Homology (PH) domain and a Proline-Rich Domain (PRD) (Fig. 3) (Faelber et al., 2013). DRPs share only three of these domains, the GTPase domain, the stalk and the BSE while other dynamin-like proteins, like the EHDs and atlastins, have only the GTPase domain and one helical domain (Daumke and Praefcke, 2016; Heymann and Hinshaw, 2009; Praefcke and McMahon, 2004). In addition, some dynamin superfamily proteins contain regulatory domains that mediate recruitment to specific sites of action. For example, the PRD mediates the recruitment of dynamin to CCVs via interaction with Src-homology 3 (SH3) domains of interaction partners such as the Bin/Amphiphysin/Rvs (BAR)-domain-containing proteins (Soulet et al., 2005). In EHDs, a C-terminal EH domain binds to target proteins containing a linear peptide motif with an Asn-Pro-Phe (NPF) repeat (see below for more details)

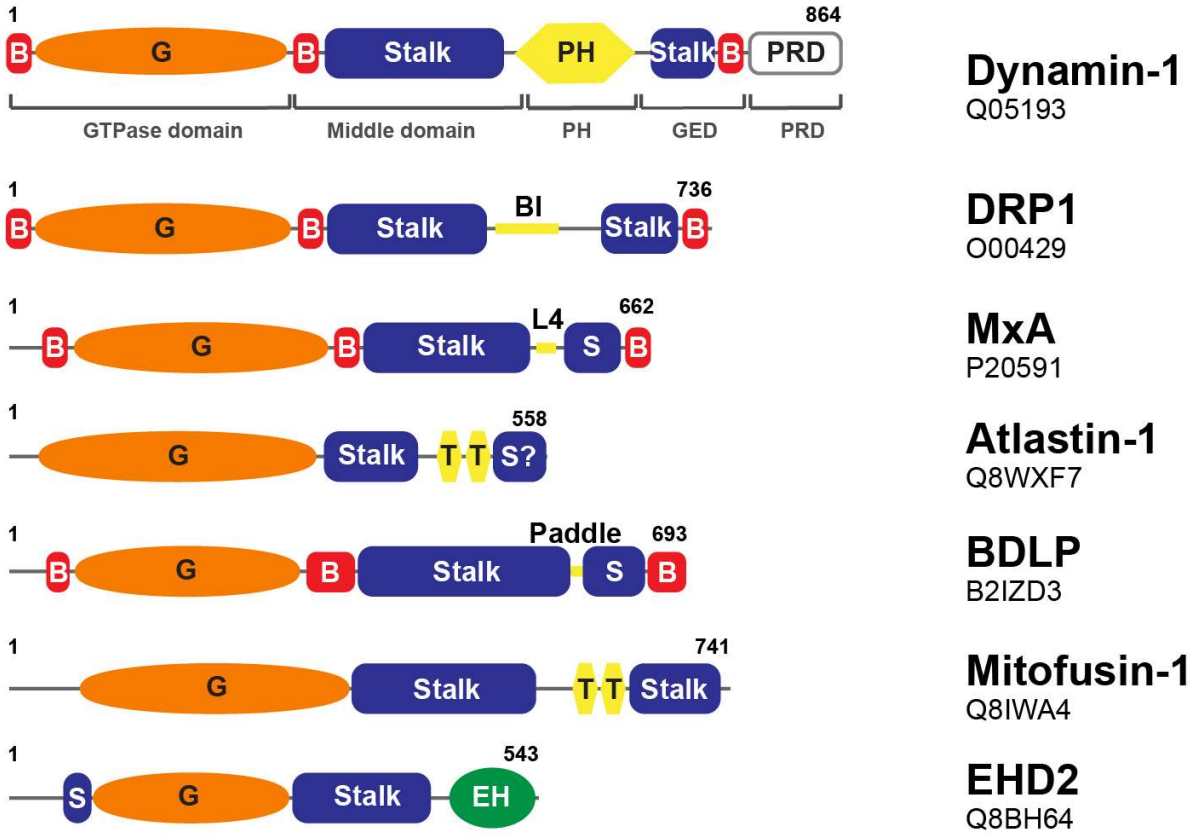


**Figure 3. Domain architecture of human dynamin family members.** Structure-based domain architecture of the indicated proteins of the dynamin superfamily. B, bundle-signaling element (BSE); PH, pleckstrin homology domain; GED, GTPase effector domain; G, GTPase domain; PRD, proline- and arginine-rich domain; T, transmembrane domain; BI, B-insert; L4, Loop 4; EH, Eps15-homology domain. Figure modified from (Faelber et al., 2013).

### 1.2.2 The structure of dynamin reveals an unexpected architecture of the helical domains

Dynamin has a size of approximately 100 kDa (Faelber et al., 2011). A crystal structure of almost full length (fl) human dynamin 1 revealed details of the domain architecture (Fig. 4) (Faelber et al., 2011; Ford et al., 2011).

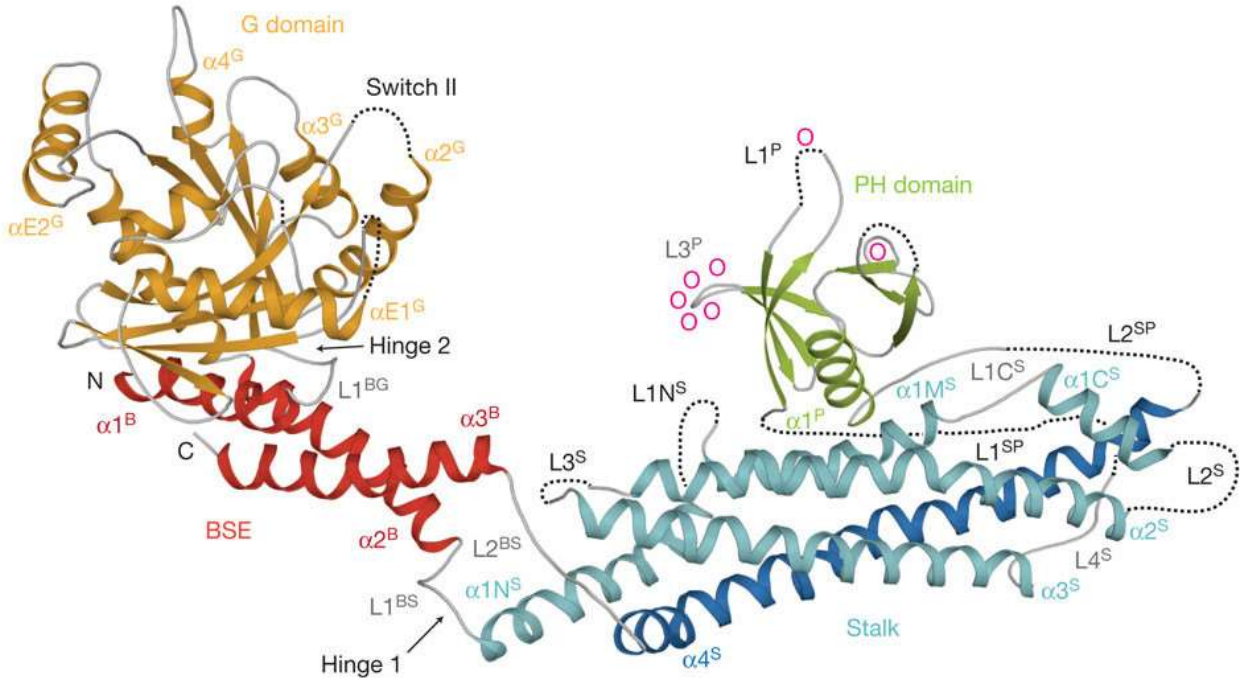


**Figure 4. Structure-based domain architecture of human dynamin 1.** Ribbon-type representation of human dynamin 1. Regions not resolved in the crystal structure are indicated by dashed lines. Domains, distinct secondary structure elements and N and C termini are labeled. Lipid-binding residues are indicated as O. The GTPase domain is colored in orange, the BSE in red, the stalk domain in blue and the PH domain in green.

The GTPase domain, is an extended form of the canonical GTPase domain fold observed in Ras and other G proteins (Fig. 4 and 5, see section 1.2.3 for further structural details) (Vetter and Wittinghofer, 2001). In direct contact with the GTPase domain is a helical domain called BSE. It is composed of a three helix bundle and connected to the GTPase domain via two conserved proline residues, Pro32 and Pro294 (hinge 1 and 2) (Faelber et al., 2011; Ford et al., 2011; Reubold et al., 2015). Surprisingly, the three BSE helices α1–3 are derived from different regions within the protein sequence. For example, α1 is located at the very N-terminus of dynamin, α2 follows the GTPase domain and α3 is positioned at the very C-terminal region (Fig. 4). Hydrophobic residues of all three helices participate in an extensive network forming the core of this domain (Faelber et al., 2011).

Following the BSE, a second helical domain, the stalk of dynamin, is composed of an antiparallel four-helix bundle (Faelber et al., 2011; Ford et al., 2011; Gao et al., 2010; Reubold et al., 2015). Despite its extended structure, the hydrophobic core of the stalk appears to mediate a high degree of stability (Faelber et al., 2011).

The PH domain is located between α3 and α4 of the stalk. It is further described in section 1.2.6. The C-terminal PRD of dynamin was not included in the crystal structure and is thought to be unstructured (Faelber et al., 2011).

In the following sections, the molecular functions of these domains are discussed in more detail.

### 1.2.3 The GTPase domain in the dynamin superfamily

The GTPase is the most highly conserved domain in the dynamin superfamily. Compared to the canonical Ras-like GTPase domain fold, additional α-helices and β-strands are present in the GTPase domain of dynamin superfamily proteins (Fig. 5) (Reubold et al., 2005). The core of the GTPase domain consists of an eight-stranded β-sheet containing six parallel strands and two antiparallel strands. The β-sheet is surrounded by seven α-helices and two single-turn helices (Fig. 5) (Reubold et al., 2005).

The GTPase domain of dynamin and dynamin-related proteins promotes nucleotide hydrolysis, an important feature for their membrane remodeling activity (Antonny et al., 2016). The GTPase domain has low affinity for GTP and even lower for GDP, hence they do not require guanine nucleotide exchange factors (GEFs) for nucleotide release (Daumke and Praefcke, 2016).

The GTPase domain of dynamins, as that of other GTPases, contains five conserved motifs (G1-G5) that are involved in nucleotide-binding (Fig. 6A and B) (Saraste et al., 1990). The G1 motif – P-loop - with the sequence GxxxxGKS/T, binds to the β-phosphate (Fig. 6A and B). The P-loop contributes with the Ser/Thr to the binding of the $Mg^{2+}$ ion, which is crucial for nucleotide hydrolysis, as well as the Thr (Thr65 in dynamin) of the G2 motif and the conserved Asp in the G3 motif (Fig. 6A and B). Residues in the G2 and G3 motifs directly contact the γ-phosphate. The motifs G2 and G3 are part of the switch I and switch II regions, respectively, which are regions that undergo nucleotide-dependent conformational changes (Fig. 6B) (Daumke and Praefcke, 2016).

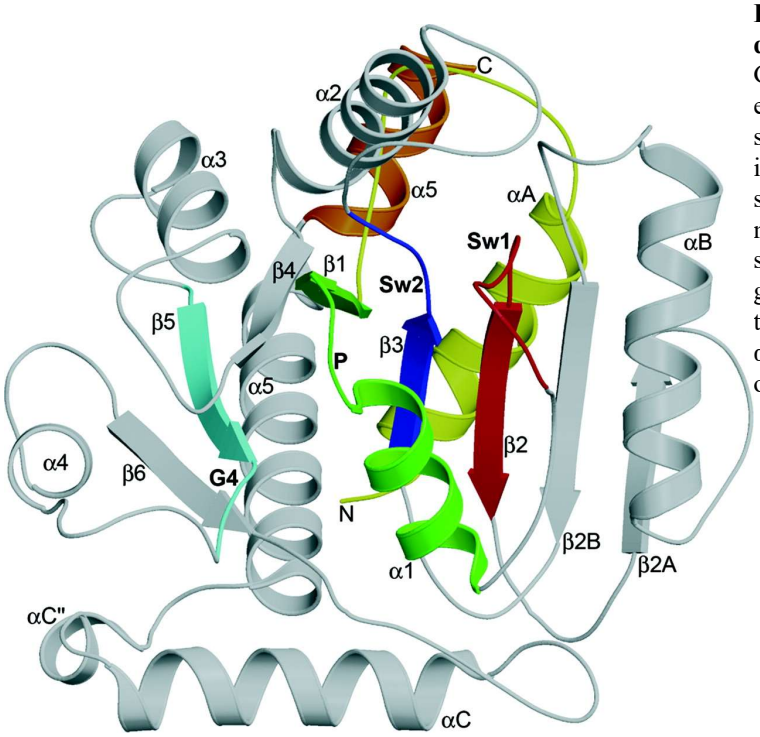


**Figure 5. Overall fold of the GTPase domain of dynamin 1.** The core of the GTPase domain of dynamin 1 consists of an eight-stranded β-sheet containing six parallel strands and two antiparallel strands. The sheet is surrounded by seven α-helices and two single-turn helices. The nucleotide-binding motifs together with the attached secondary structure elements are colored as follows: green, P-loop; red, switch 1; blue, switch 2; turquoise, G4. The N- and C-terminal helices αA and α5 are highlighted in yellow and orange, respectively (Reubold et al., 2005).

The G4 motif is conserved among the superfamily and is responsible for mediating the specificity to the guanine base of the GTP (Fig. 6A and B). The Asp of the G4 motif interacts with the guanine base of the GTP (Fig. 6B). The G5 motif is not well conserved between different dynamin superfamily proteins and interacts in various ways with the guanine base and/or ribose (Fig. 6B) (Daumke and Praefcke, 2016).

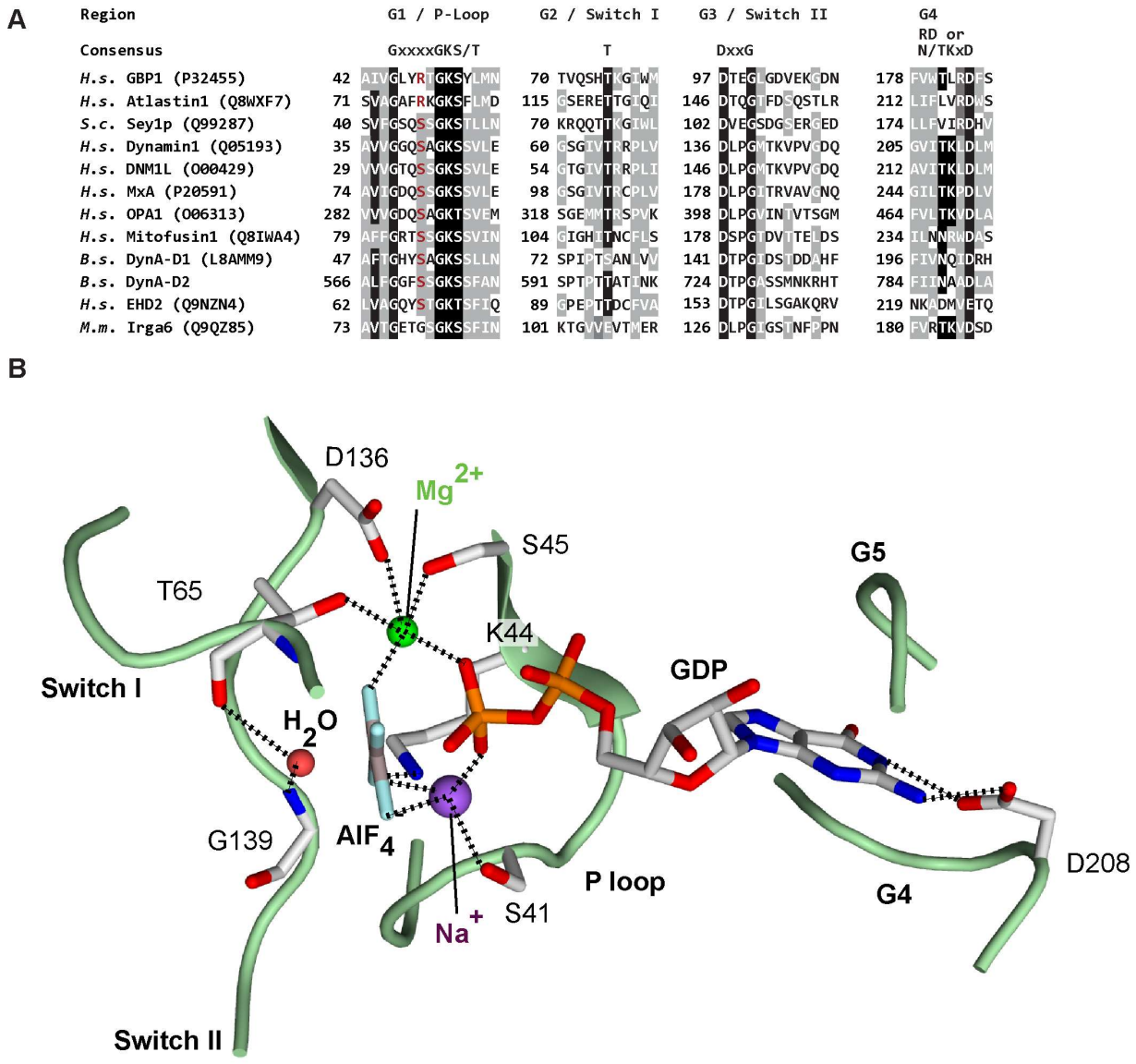


**Figure 6. Nucleotide binding and catalysis of dynamin superfamily proteins.** (A) Sequence alignment of dynamin superfamily proteins in the G1–G4 motifs. Conserved canonical residues are highlighted in black or dark gray, other conserved residues in light grey. The catalytic arginine and serines in the P-loop are shown in red. For DynA from *B. subtilis*, the sequence of both GTPase domains is shown. (B) Details of the interactions of the G1–G5 motifs in the catalytic site of the GDP-$AlF_4$-bound dynamin (pdb 2X2E) are shown, with hydrogen bonds indicated by dashed lines. Figure modified from (Daumke and Praefcke, 2016).

## 1.2.4 Dimerization via the G-interface stimulates GTP hydrolysis

The GTPase domain of dynamin superfamily proteins can dimerize across a conserved interface, the G–interface (Chappie et al., 2010). The formation of such interface is crucial for

the assembly stimulated GTPase activity of dynamin superfamily proteins. In dynamin, the G-interface involves residues in the P-loop, the two switch regions, the "*trans* stabilizing loop" and the G4 motif (Fig. 7) (Chappie et al., 2010; Daumke and Praefcke, 2016). The "*trans* stabilizing loop" is the region that reaches across the G-interface and stabilizes the P-loop and switch I conformations for hydrolysis (Fig. 7A) (Chappie and Dyda, 2013). In the resulting GTPase dimers, the active sites face each other, thereby sequestering the nucleotides from the solvent and reciprocally stabilizing the switch regions, whereas the BSEs extend in opposite directions from the dimer core (Fig. 7A and B) (Chappie et al., 2010).

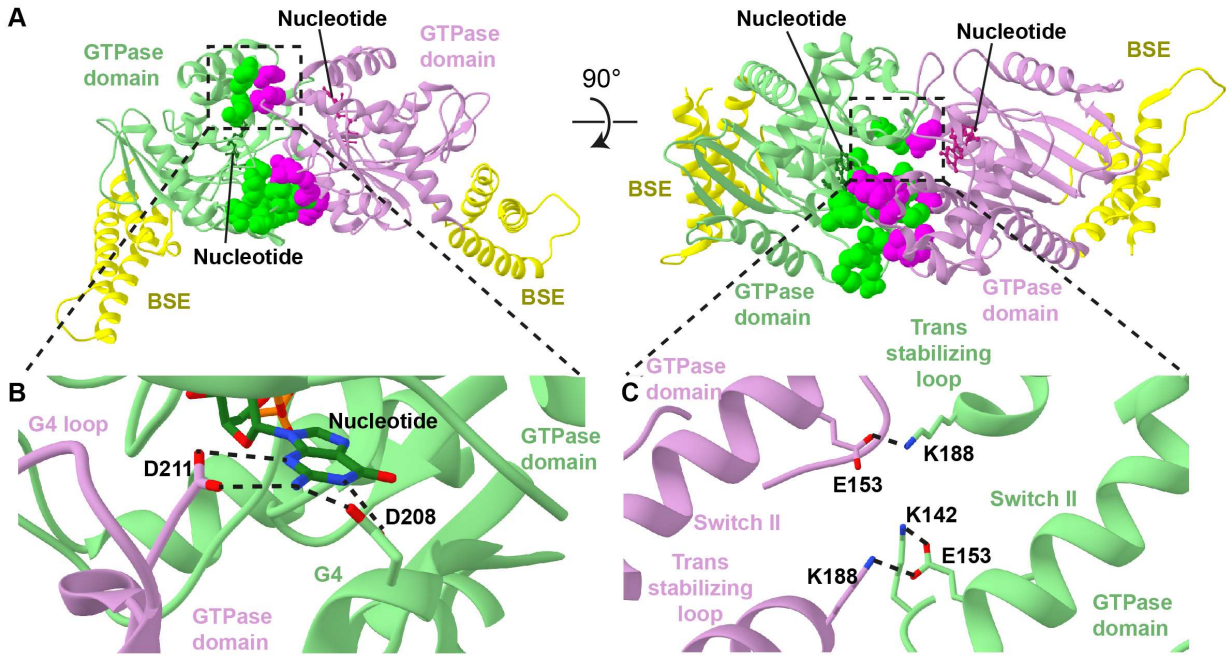


**Figure 7. G-interface of human dynamin 1. (**A) Structure of GDP-$AlF_4$--stabilized GG dimer (PDB 2X2E) shown from the side (left) and top (right). The GTPase domains of individual monomers are colored in green and purple. The BSE is colored in yellow. Structural interactions that stabilize the GG dimer and residues involved in *trans* contacts between monomers are depicted as spheres. (B-C) Detailed interactions between key residues involved in GTPase domain dimerization. Dashed lines indicate hydrogen-bonding interactions.

The interactions within the G–interface includes a *cis/trans* coordination of the guanine base by the G4 motif, interactions of switch I and P-loop with the "*trans* stabilizing loop" and symmetric salt bridges responsible for anchoring the nucleotide base of the dimer in *trans* (Fig. 7B and C) (Chappie et al., 2010).

In all GTPases, efficient hydrolysis requires the correct positioning of a water molecule for an in-line $S_N2$ attack on the γ-phosphate, neutralization of a negative charge that develops between

the β- and γ-phosphates in the transition state of GTP hydrolysis and the stabilization of the switch regions within the catalytic core (Li and Zhang, 2004; Paduch et al., 2001). These conditions can be achieved in dynamins through the formation of the G–interface, which results in the reciprocal activation of the individual monomers (Gasper et al., 2009).

Crystal structures of the dynamin and dynamin-related protein GTPase domains in the different nucleotide-states revealed the details of how GTP hydrolysis is achieved within the superfamily (Cao et al., 2017; Chappie et al., 2010; Rennie et al., 2014). In dynamins, the negative charge neutralization between the β- and γ-phosphate in the transition state is thought to be achieved via a potassium ion present in the G–interface which coordinates the $AlF_4$-, the β-phosphate of the nucleotide and the switch I (Chappie and Dyda, 2013). This mechanism of hydrolysis differs from the known mechanism of GTP hydrolysis in small Ras-like G proteins, where a catalytic GTPase-activating protein (GAP)-arginine finger compensates the negative charge between the β- and γ-phosphate (Scheffzek et al., 1997).

### 1.2.5 Identification of the power stroke in dynamin and closely related proteins

For several dynamin superfamily members, nucleotide hydrolysis in the GTPase domain was shown to translate into a mechanical movement of the adjacent helical domain, as indicated by large scale structural rearrangements upon GTP hydrolysis and/or phosphate release (Daumke and Praefcke, 2016). It was shown that these structural changes vary considerably among the different family members, as outlined below.

In the crystal structures of dynamin bound to the non-hydrolysable GTP analogue GMPPCP, the GTPase transition state mimic GDP-$AlF_4$- and GDP, the BSE domain adopts two different conformations relative to the GTPase domain (Chappie et al., 2010). When bound to GDP-$AlF_4$-, GDP or in the absence of nucleotide, the BSE is in the closed conformation, whereas in the GMPPCP-bound form, it is rotated by 70° around the conserved Pro294 in the hinge region between GTPase domain and BSE, therefore, adopting the open conformation (Fig. 8). It has been suggested that the movement from the open conformation to the closed acts as a power

stroke during membrane remodeling, which is important for membrane fission (Antonny et al., 2016; Daumke and Praefcke, 2016).

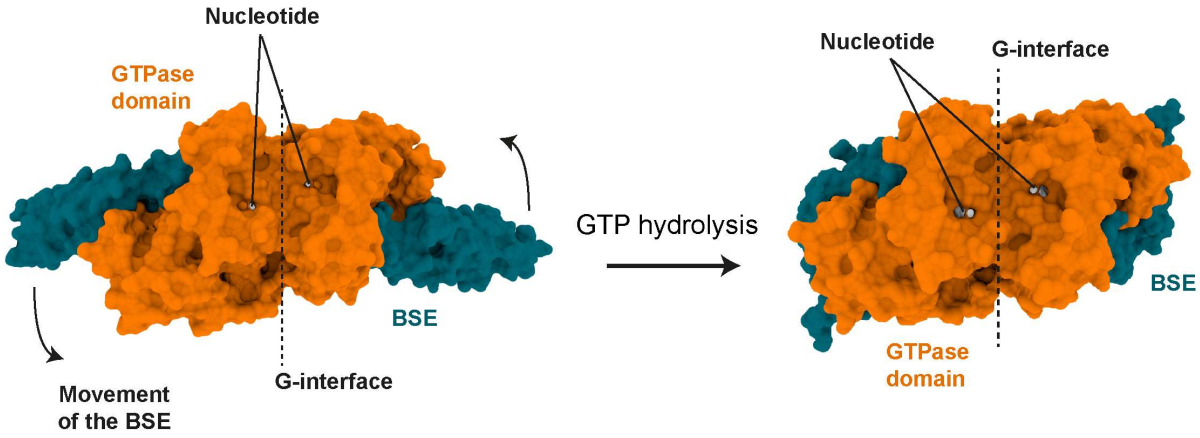


**Figure 8. The dynamin powerstroke.** Surface representation of a dynamin BSE constructs bound to GMPPCP (left, PDB: 3ZYC) and GDP-$AlF_4$- (right, PDB: 2X2E) highlighting alternative BSE conformations. The GTPase domain is colored in orange and the BSE in dark cyan. The black line points to the nucleotide (white). The dash line represents the GTPase dimer via the G-interface .The black arrow depicts the 70° rotation of the BSE in the transition-state complex.

In a similar way to what was observed for the classical dynamin structures, the crystal structures from the dynamin-related protein 1A of *Arabidopsis thaliana*, AtDRP1A, showed an open BSE in the GDP-$AlF_4$--bound form and a closed BSE, 95° rotated around the conserved Pro303, in the presence of GDP. As suggested for dynamin, it is believed that the BSE movement occurs upon GTP hydrolysis and Pi release, and acts as a power stroke during membrane remodeling , promoting the fission of vesicles (Yan et al., 2011).

An open and a closed conformation was also shown for the MxA protein in the GMPPCP- and GDP-bound state. Associated with GTP binding and hydrolysis, the BSE moves around the conserved Pro340 that corresponds to Pro294 in dynamin (Fig. 9). In the GMPPCP-bound crystal structure, the electron density for the BSE is only fully resolved in one of the two subunits of the dimer, due to crystal packing effects. A model based on the well defined subunit is shown in Fig. 9 (Rennie et al., 2014). Another biochemical study confirmed that MxA employs a related mechanism of dimerization and GTP hydrolysis to the classical dynamin which is critical for its antiviral activity (Dick et al., 2015)

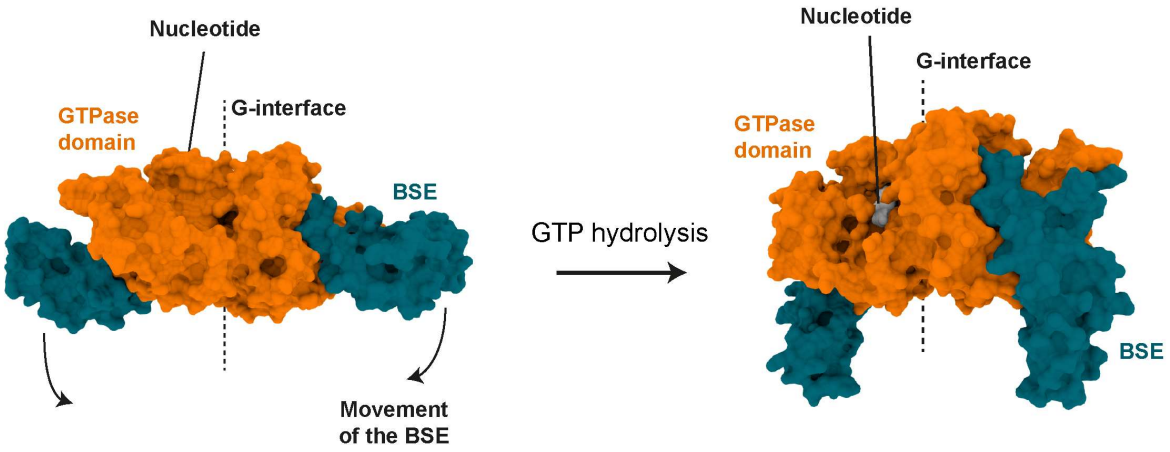


**Figure 9. GTP binding and hydrolysis induce a conformational change in the BSE of MxA.** Surface representation of the stalkless MxA bound to GMPPNP (left, PDB: 4P4S) and GDP (right, PDB: 4P4T) shows alternative BSE conformations. The GTPase domain is colored in orange and the BSE in dark cyan. The black line points to the nucleotide (white). The dash line represents GTPase dimerization via the G-interface .The black arrow depicts the rotation of the BSE upon nucleotide hydrolysis (Rennie et al., 2014).

For DRP1 (also known as dynamin-like 1 – DNML1) dimeric GTPase domain/BSE structures were obtained in an open BSE conformation bound to the GTP analogue GMPPCP and GDP-$AlF_4$- (Kishida and Sugio, 2013). A closed BSE conformation was obtained for the nucleotide-free monomeric form (Wenger et al., 2013) and also for the full-length structure (Fröhlich et al., 2013). Mutagenesis data suggested a related mechanism compared to the classical dynamin, in which nucleotide hydrolysis promotes the closing of the BSE (Wenger et al., 2013).

### 1.2.6 Membrane binding of dynamin superfamily proteins

The membrane-binding site of dynamin superfamily proteins is generally localized at the tip of the helical domains. Some of the dynamin superfamily proteins have a specialized domain for membrane binding, such as the PH domain in dynamins (Faelber et al., 2011). Others, like atlastin and mitofusins have predicted transmembrane helices at this position (Byrnes et al., 2013; Cao et al., 2017). MxA and DRP1 bind to membranes via an extended loop at the tip of the stalk (Fröhlich et al., 2013; Gao et al., 2011).

The PH domain of the classical dynamins binds to phosphatidylinositol-4,5-biphosphate (PIP2) and inserts into the outer leaflet of the lipid bilayer via a variable loop (Sundborger and

Hinshaw, 2014). This domain was first identified in pleckstrin and later also in other proteins mediating intracellular signaling (Haslam et al., 1993). It is a globular domain composed by a seven-stranded β sandwich of two orthogonal antiparallel β-sheets which is closed at one corner by a C-terminal α-helix (Ferguson et al., 1994). Opposite to this helix are three loops that vary the most among PH domains (Lemmon, 2007). The basic fold is very similar to other PH domains (Scheffzek and Welti, 2012).

Instead of a PH domain, MxA has a 45 amino-acid loop, loop L4, at the same sequence position as the PH domain in dynamin (Faelber et al., 2013). This loop is unstructured in the MxA crystal structure and was demonstrated to mediate membrane interaction with preference for negatively charged lipid surfaces (Gao et al., 2011; von der Malsburg et al., 2011).

In a similar fashion to MxA, DRP1 has a long and mostly unstructured loop of more than 100 amino-acids, the B insert. It interacts with cardiolipin (CL) and enhances DRP1 oligomerization and assembly-stimulated GTP hydrolysis (Bustillo-Zabalbeitia et al., 2014). The B insert is also important for interactions with a mitochondrial adaptor proteins that can regulate DRP1 function in mitochondrial membranes (Bustillo-Zabalbeitia et al., 2014; Clinton et al., 2016).

### 1.2.7 Oligomerization in dynamin superfamily proteins

As described in the previous section, membrane binding has been shown to induce the oligomerization of dynamin superfamily proteins into helical oligomers. Crystal structure analyses on dynamin, MxA and DRP1 provided a detailed molecular description of the oligomerization mechanism which will be described in a chronological order in the following section.

#### 1.2.7.1 Oligomerization of MxA reveals a criss-cross arrangement of the stalks

The structural details of oligomerization were initially described in the isolated MxA stalk crystal structure and later for the full length MxA (Gao et al., 2010, 2011). These studies showed that the stalk is the central assembly hub and mediates oligomerization of MxA into filaments. Two adjacent stalks were shown to assemble in a criss-cross fashion via a highly conserved central interface, interface-2 (Fig. 10) (Gao et al., 2010, 2011). Mutations in this interface result in a monomeric protein that fails to oligomerize (Gao et al., 2011). This indicates the central importance of this interface for dimer and oligomer formation. Two additional interfaces, interfaces-1 and 3 (Fig. 10), were also shown to be important for further oligomerization of stalk dimers. Interface-1 mediates interactions with the neighboring stalk dimer above interface-2 (Fig. 10). Interface-3 is non-symmetric and mediates lateral contacts between stalks oriented in parallel (Fig. 10). It involves loop L1, which interacts with residues in the neighboring stalk. Still in the interface-3, loop L4 is in the vicinity of the corresponding loop L4 from an opposing molecule (Fig. 10) and might represent a low-affinity interaction site (Gao et al., 2010). The identified oligomerization sites in interface-3 allow some flexibility of the assembly, which results in different diameters of the helical oligomers (Gao et al., 2011; Haller et al., 2010) .

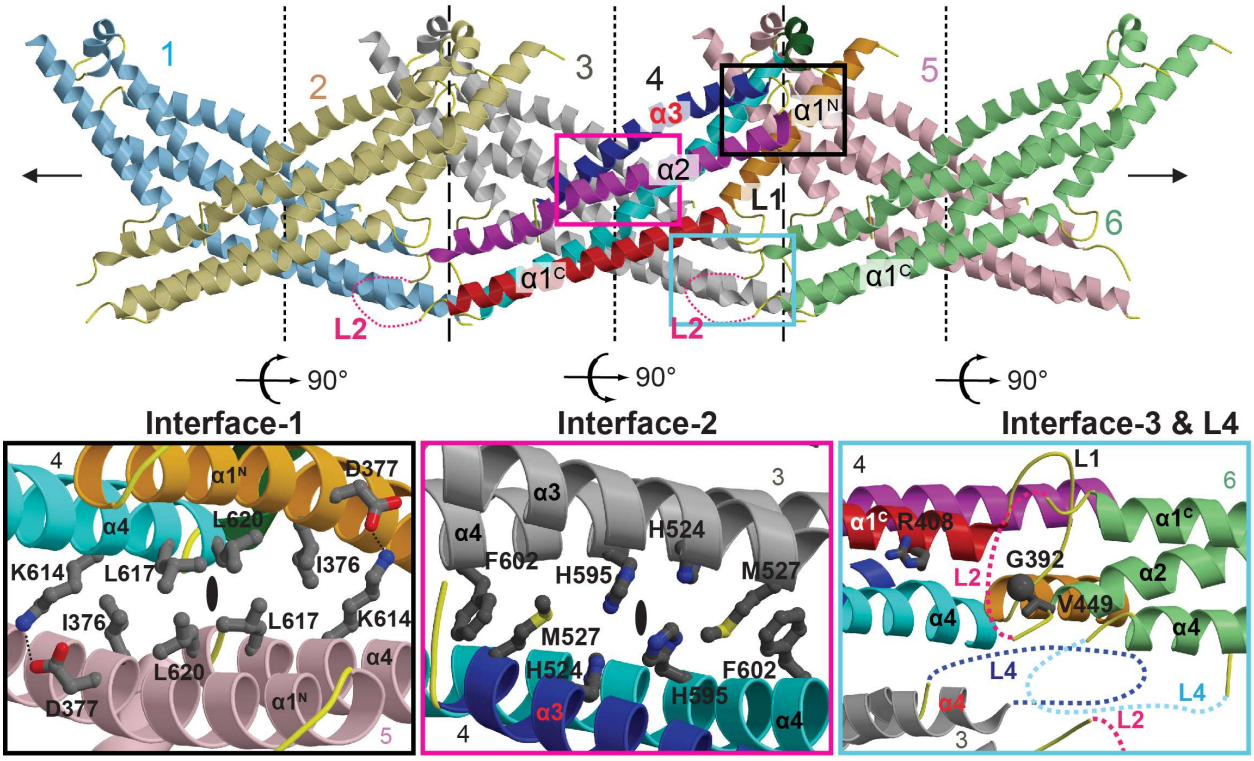


**Figure 10. Oligomerization via the MxA stalk.** Ribbon-type representation of six oligomerized MxA stalks. The parallel non-crystallographic pseudo-two-fold axes across interface 1 and interface 2 are indicated by black dashed lines. Regions not resolved in the structure are indicated by dashed lines. Figure modified from (Gao et al., 2010)

### 1.2.7.2 Dynamin shows a related oligomerization mode compared to MxA

Similarly to the MxA stalks, the dynamin 1 stalks in the crystals were arranged in a criss-cross fashion resulting in a linear stalk filament (Faelber et al., 2011). The highly conserved interface-2 also locates in the center of the stalk and assembly via this interface results in an extended dynamin dimer that serves as building block for dynamin oligomers (Reubold et al., 2015). Interfaces-1 and -3 were only later observed in the crystal structure of the dynamin 3 tetramer (Reubold et al., 2015). In this structure, dynamin dimers further assemble into tetramers via interface-1 and interface-3 (Fig. 11). Interface-1 at the top of the stalk features four hydrophobic residues that are highly conserved in the dynamin superfamily (Fig. 11). The main contributors for interface 3 are loop L1 of the 'inner' and loop L2S of the 'outer' stalks (Fig. 11), which mediate an intricate interaction network involving all four stalks (Fig. 11) (Reubold et al., 2015).

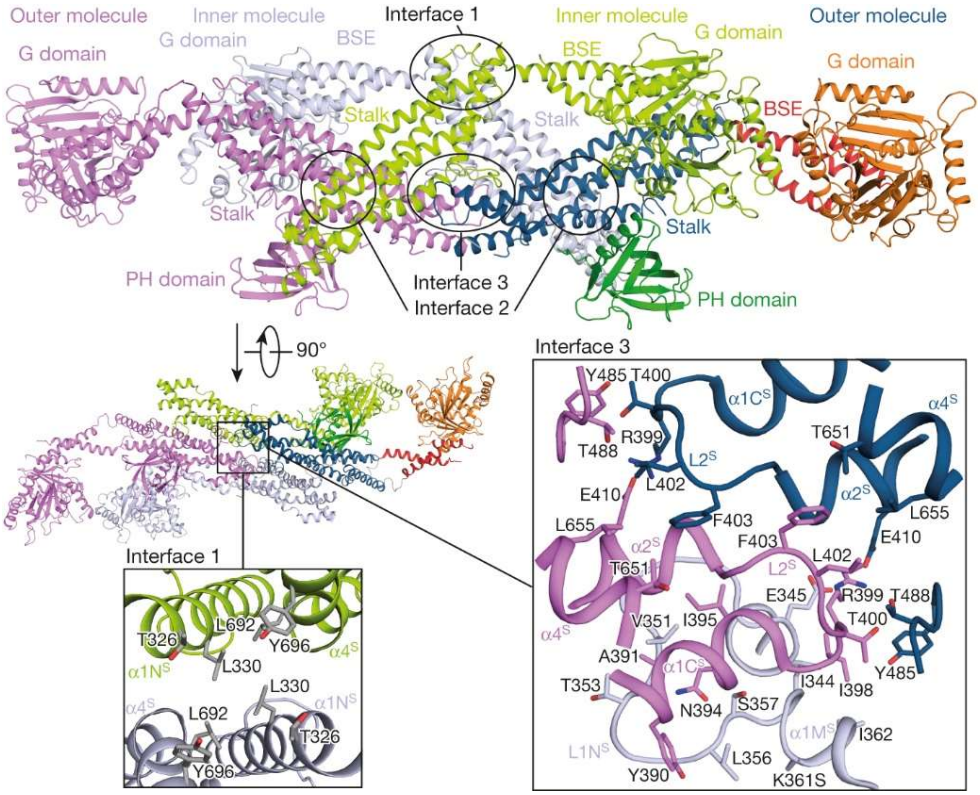


**Figure 11. The crystal structure of the dynamin tetramer.** Four molecules in the tetramer are colored separately; in the molecule on the right each domain is individually colored. The tetramer consists of two dimers, each formed via the central interface-2. The two dimers are connected via interfaces-1 (left box) and -3 (right box) to build the tetramer. One inner molecule is omitted from the detailed view for clarity. Figure from (Reubold et al., 2015).

### 1.2.7.3 A unique oligomerization interface in DRP1?

In the crystal structure of the nucleotide-free DRP1, the four molecules in the asymmetric unit assemble into two dimers via interface-2 in the center of the stalks (Fröhlich et al., 2013). The interface-2 includes both hydrophobic contacts and salt bridges resulting in a criss-cross stalk dimer. The DRP1 dimers within the crystal stacked on each other via an additional interface in the stalk, referred to by Fröhlich and colleagues as the interface-4 (Fröhlich et al., 2013). It is located at the opposite side of interface-2 and has low sequence similarity to dynamin and MxA, but is highly conserved in DRPs (Faelber et al., 2011; Fröhlich et al., 2013; Gao et al., 2011). In the DRP1 oligomer, all GTPase domains and the B–inserts were located at opposing sides of the oligomer. The oligomerization model, based on the crystal structure and low resolution EM reconstruction of DRP1 on membrane tubules, proposes that the stalks assemble with a

neighboring stalk to form a double layer filament that further assemble into a helix with a pitch of 14.4 nm (Fröhlich et al., 2013). Two double filaments, extending next to each other around the lipid tubule, account for the observed two-start helix with a 28.8 nm helical pitch. In this model, the GTPase domains of each double stalk filament dimerize across helical turns with GTPase domains of the neighbouring filament allowing nucleotide-dependent rearrangements of adjacent filaments (Fröhlich et al., 2013).

### 1.2.8 Membrane remodeling mechanism in the dynamin superfamily

Dynamin superfamily proteins have the ability to assemble into regular oligomers around membranes and other templates, therefore acting as scaffolds for membrane remodeling. The classical dynamin can self-assemble around microtubules or the neck of clathrin-coated vesicles into regular rings or spirals (Takei et al., 1995). Similar ring-like assembly at membranes was also shown for MxA (Haller et al., 2010; von der Malsburg et al., 2011), DRP1 (Ingerman et al., 2005), EHD1 (Pant et al., 2009) and 2 (Daumke et al., 2007; Shah et al., 2014), OPA1 (Ban et al., 2010) and Bacterial dynamin-like protein (BDLP) (Low et al., 2009). These membrane remodeling activities *in vitro* were shown to relate to their function in membrane remodeling (Antonny et al., 2016; Byrnes et al., 2013; Daumke and Roux, 2017). In this section, the relation between oligomerization, GTP hydrolysis and conformational changes to membrane fission and fusion by dynamin, atlastins, BDLP and mitofusins are introduced.

#### 1.2.8.1 A power stroke drives constriction in helical dynamin oligomers

Several studies of the past decades have focused on understanding the mechanism of dynamin-mediated membrane fission in which several models have been proposed. Currently, one model in particular has gained traction in the field. In this model, the dynamin tetramer is recruited from the cytosol to the membrane (see 1.2.6) which releases the PH domain from its autoinhibitory site and promote oligomerization (see 1.2.7.2 and 1.2.8). The GTPase domains bind to GTP which induces dimerization via the G-interface across helical filaments (see 1.2.4) (Chappie et al., 2011). The BSE senses the nucleotide loading status and adopts an open

conformation in the presence of GTP and moves to a closed conformation in the presence of GDP-$AlF_4$- or in the absence of nucleotide (see 1.2.5) (Fig. 8) (Chappie et al., 2010, 2011). This movement acts as a power stroke for dynamin upon GTP hydrolysis and can trigger relative sliding of the helical turn around the membrane, leading to constriction and fission (Fig. 12) (Chappie et al., 2011; Faelber et al., 2011; Ford et al., 2011). In this model, it is less clear how disassembly occurs. Two hypotheses have been suggested: First, once fission has occurred, dynamin could disassemble since the tubular membrane template has been consumed. Second, the stresses appearing in the dynamin coat under constriction could cause it to break apart. In these two cases, disassembly would be a consequence of fission and/or constriction, and GTP hydrolysis energy would primarily be spent in generating constriction force (Antonny et al., 2016) .

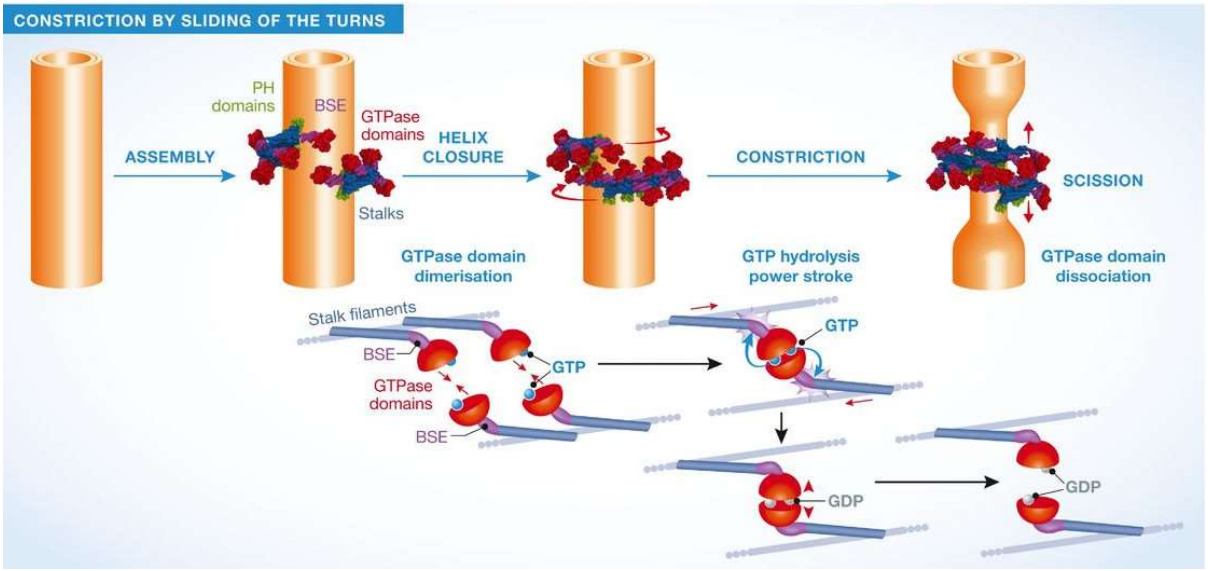


**Figure 12. The constriction/ratchet model.** In this model, constriction is realized by active sliding of the helical turns and fission by spontaneous fusion of the membrane. The one ring state presented is proposed to be the most common *in vivo*. Figure from (Antonny et al., 2016)

### 1.2.8.2 Model for atlastin-mediated membrane fusion

Two crystal structures of atlastin show that the helical domains can adopt two different conformations relative to the GTPase domain in different nucleotide states (Fig. 13) (Byrnes et

al., 2013). This movement was shown to be different from what was observed for the classical dynamin and MxA (Bian et al., 2011; Byrnes and Sondermann, 2011; Byrnes et al., 2013). In the GDP-bound open conformation, the two helical domains point in opposite directions with the GTPase domain dimer in the center (Fig. 13, left). In the GMPPNP-bound closed conformation, the helical domains extend in parallel and directly contact each other (Fig. 13, right). The closed conformation was also obtained for a second crystal structure in the GDP-bound state, suggesting that the two conformations are of similar energy and can be stabilized by different crystal contacts (Daumke and Praefcke, 2016). Studies revealed that the movements of the helical domains are a response to GTP binding and hydrolysis, supporting a model where GTP hydrolysis and helical domain movement control the tethering and fusion of opposing ER membranes (Byrnes et al., 2013).

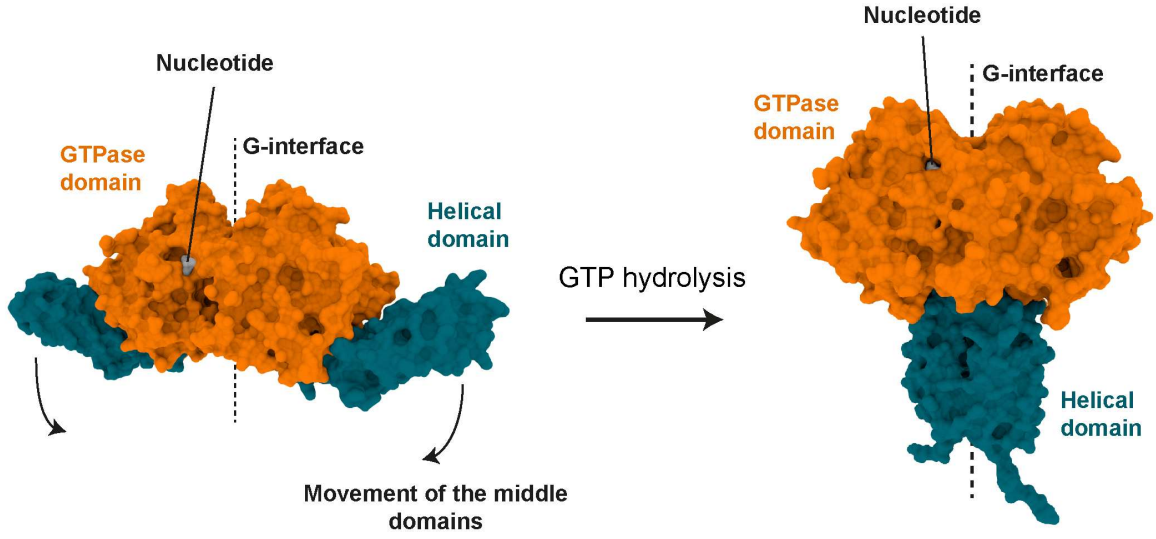


**Figure 13. Conformation changes on atlastin.** The atlastin-1 dimer are shown in the open (left) and close (right) conformations. The GTPase domains (orange) dimerize via the G-interface and the helical domains (dark cyan) undergo a large conformational change. In the GDP-bound state the protein can adopt open (left) and close (right) conformations. In the GMPPNP-bound state, as well as the GDP-$AlF_4$--bound state, the protein adopts a tightly closed conformation (Byrnes et al., 2013). The GTPase domains are colored in orange, the helical domains in dark cyan and cyan and the "paddle" in dark red. The black arrow represents the opening of the helical domains. The black dash line represents the GTPase dimerization via the G-interface. The nucleotide is colored in white.

The introduced model of ER membrane fusion by atlastins is based on structural and biochemical studies. Initially, monomeric atlastins at the ER bind to GTP and assume the open conformation (Byrnes and Sondermann, 2011). Next, atlastin monomers rapidly form a GTP-dependent dimer with the nucleotides buried at the G-interface (Byrnes and Sondermann, 2011;

Byrnes et al., 2013; Liu et al., 2015). This dimer is weak and transient, and may adopt either a conformation corresponding to the open conformation or a conformation where the GTPase domains are dislodged from the helical domains and are free to rotate (Byrnes et al., 2013). Hydrolysis converts the dimers into a high-affinity state characterized by a tight interaction between the helical domains in the closed conformation (Byrnes et al., 2013; Moss et al., 2011). Next, inorganic phosphate and GDP were suggested to be released in a consecutive manner, causing the dissociation of the atlastin dimers into monomers. Dissociation may occur in the GDP-bound state or in the nucleotide-free state, in which atlastin remains in the monomeric form (Byrnes and Sondermann, 2011). The entire series of events can occur with atlastin molecules sitting in the same membranes (*cis* interactions) or in different membranes (*trans* interactions), although only *trans* interactions can result in the tethering and fusion of opposing membranes (Liu et al., 2015). Multiple GTPase cycles are required for a successful fusion event, since the transition state dimer formed by atlastin molecules often completes the cycle of GTP hydrolysis and converts back into monomers before having induced fusion (Liu et al., 2015).

#### 1.2.8.3 BDLP and mitofusin may feature a unique membrane fusion mechanism

The BDLP from the cyanobacterium *Nostoc punctiforme* dimerizes via the GTPase domains in the GDP-bound form (Low and Löwe, 2006). The two helical domains of each monomer are comparable to the helical domains of dynamin-related proteins. These domains are in the closed conformation with the tips from opposing molecules contacting each other in the closed conformation. The tip of the helical domains contains the membrane binding region, the "paddle" domain, which are in contact in the closed conformation (Fig. 14, left). In the presence of GMPPNP and liposomes, BDLP oligomerizes at the surface of liposomes leading to the formation of membrane tubules. A cryo-EM reconstruction of GTP-bound BDLP on membrane tubules revealed a large scale opening of the helical domains, which extend parallel to each other, while the "paddle" inserts into the membrane (Fig. 14, right) (Low et al., 2009).

In the GTP-bound state, BDLP is thought to allow oligomeric assembly on membranes, and upon GTP hydrolysis. Low and Löwe suggested that BDLP oligomerization on one membrane

leaflet promotes high membrane curvature, as a prerequisite to undergo membrane fusion (Low and Löwe, 2006). The recycling of the oligomer back to the closed form promotes membrane fusion (Daumke and Praefcke, 2016; Low et al., 2009). This model is consistent with the structural conformations obtained for BDLP, but does not include interactions of BDLP molecules across two fusing membranes. The architecture of the BDLP GTPase domain and the first helical domain has striking similarities to the recently published crystal structure of the mitofusin (Mfn1) dimer (Daumke and Roux, 2017). The orientation of the first helical domain relative to the GTPase domain is almost identical in the closed BDLP structure and the Mfn1 construct (Daumke and Roux, 2017). It has been suggested that mitofusins may undergo a similar opening of the helical domains, as observed for BDLP.

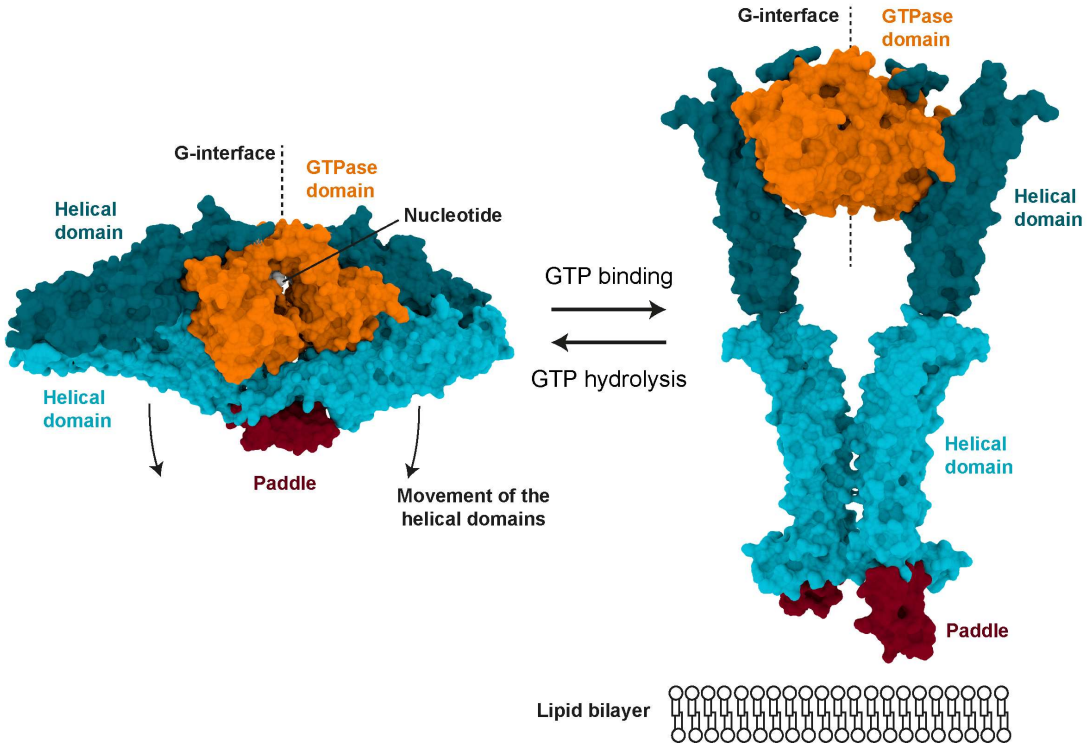


**Figure 14. Closed and open BDLP structures.** The structure of the closed BDLP-bound to GDP (left) was obtained by X-ray crystallography while the open GMPPNP-bound structure was obtained by cryo-EM reconstruction of BDLP oligomerized around a tubular membrane template at a resolution between 11 and 17 Å. The GTPase domains are coloured in orange, the helical domains in dark cyan and cyan and the "paddle" in dark red. The black arrow represents the opening of the helical domains. The black dash line represents the GTPase dimerization via the G-interface. The nucleotide is colored in white.

Furthermore, sequence comparisons indicate that the deleted stretch of sequence of the Mfn1 construct may form a second helical bundle corresponding to the other lower part of the helical

domain in BDLP, whereas the paddle in BDLP may correspond to the predicted transmembrane region of Mfn1 (Cao et al., 2017). Based on this observation, BDLP and mitofusins may have a similar mechanism for membrane fusion.

In addition, mitofusins might relate to the model of membrane fusion by atlastins (see section 1.2.8.2) (Liu et al., 2015). Thus, GTPase domain dimers may initially form in *trans* across two adjacent membrane surfaces to allow tethering. A nucleotide hydrolysis-dependent power stroke may then pull the membranes together, allowing membrane fusion (Cao et al., 2017). This model is consistent with recent cryo-electron tomography analyses, in which elongated protein densities, possibly corresponding to open forms of the mitofusin molecules, were reported to contact each other across fusing mitochondrial membranes (Brandt et al., 2016). However, the low resolution data of this study precludes the elucidation of the exact protein conformation.

### 1.2.9 Autoinhibition and activation in the dynamin superfamily

Activation of dynamin is influenced by lipid binding, self-assembly and the binding of SH3 domain containing proteins to the PRD (Barylko, 1998; Barylko et al., 2010; Sundborger and Hinshaw, 2014; Zheng et al., 1996). In the crystal structures of the dynamin 1 and 3, the PH domains bind to a conserved surface of the stalk, the interface-4 (Faelber et al., 2011; Reubold et al., 2015). It consists of the interaction between the the stalk and the PH domain and was present in the dynamin 1 crystal structure and in only two of the four molecules in the dynamin 3 tetramer (Faelber et al., 2011; Reubold et al., 2015). It was postulated that the interface-4 prevents oligomerization of dynamin in solution. In order to promote oligomerization, the PH domains of the cytosolic dynamin tetramer bind to the membrane tubule and are thought to break autoinhibiotry contacts (Fig. 11) (Reubold et al., 2015). The protein can then further oligomerize around the membrane tubule via the interfaces-1 to -3 (Fig. 10 and 11) (Faelber et al., 2011; Gao et al., 2010).

The PH domain acts as an autoinhibitory domain by sterically blocking the oligomeric assembly of dynamin (Bethoney et al., 2009; Ramachandran et al., 2009; Reubold et al., 2015). Mutations on this domain are linked to human diseases, such as centronuclear myopathy (CNM) and Charcot–Marie–Tooth (CMT) neuropathy (Fig. 15) (Durieux et al., 2010). Some CNM

mutations promotes activation of GTP hydrolysis and oligomerization even in the absence of lipids, which suggests hyperactivation of dynamin as a cause for this diseases (Kenniston and Lemmon, 2010). It was suggested that upon release from its autoinhibitoy site, the PH domain shifts along the stalk to bind the membrane tubule, assuming a position where it cannot block oligomerization (Fig. 15) (Reubold et al., 2015; Srinivasan et al., 2016). Using a construct that lacks the PH domain, dynamin assembles into regular oligomers even in the absence of membranes, due to the absence of the autoinhibitory PH domain (Reubold et al., 2015). A similar phenotype may be observed for the disease-relevant mutations in CNM, since it affects the interface between the stalk and PH domain and may break the autoinhibitory interaction and promote uncontrolled oligomerization, thereby leading to the disease (Reubold et al., 2015).

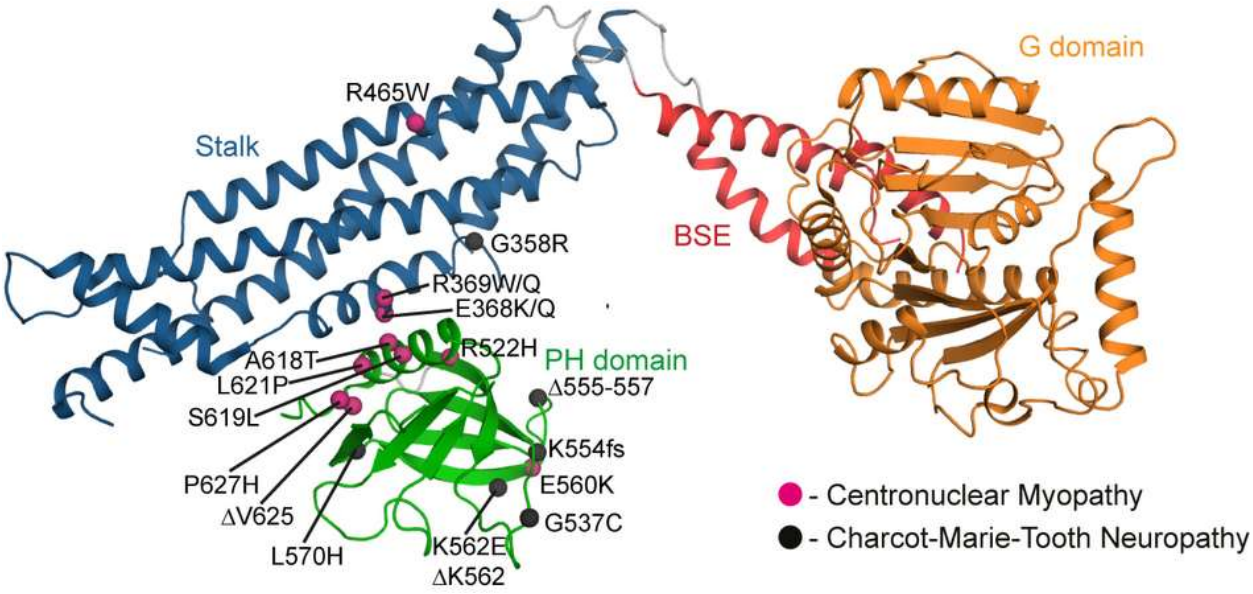


**Figure 15. Disease-related mutations in dynamin.** Localizations of mutations leading to Charcot–Marie–Tooth neuropathy (black balls) and centronuclear myopathy (pink balls) are plotted onto a dynamin 3 monomer. Note that the majority of the mutations are located at the site between the stalk and the PH domain. Figure from (Reubold et al., 2015).

The activation process of DRP1 involves translocation from the cytosol to the mitochondrial outer membrane (MOM) and assembly into rings or spirals at the MOM, leading to membrane constriction and dynamin 2-dependent fission (Hoppins et al., 2007; McBride and Frost, 2016). In mammalian cells, other mitochondrial proteins have been proposed to be essential for mitochondrial recruitment and regulation of DRP1 and therefore activation. The mitochondrial fission factor (Mff) and the mitochondrial dynamics proteins (MiD), MiD51 and MiD49, have

been implicated both in DRP1 recruitment and in stimulation of the fission process. Activation of DRP1 by Mff is independent of lipid interactions and coordinates DRP1 self-assembly, which enhances its GTPase activity (Clinton et al., 2016).

MiD proteins can function as negative effectors of DRP1 to create a pool of mitochondrial DRP1 responsive to specific triggers (Labbé et al., 2014). *In vitro*, MiD51 strongly inhibits DRP1 assembly and its GTPase activity and the addition of ADP relieves this inhibition and promotes DRP1 assembly into spirals with enhanced GTP hydrolysis, suggesting that this may be relevant for DRP1 regulation in cells (Labbé et al., 2014; Losón et al., 2014). MiD51 can act concurrently with Mff in the DRP1-mediated fission processes by activating or inhibiting the rate of DRP1 GTP hydrolysis.

A possible scenario is that MiD49 and MiD51 engages with, and facilitates, DRP1 assembly at the mitochondrial outer membrane by inhibiting its GTPase activity and that Mff stimulates DRP1 GTPase activity, which points to its role in the constriction phase of fission (Osellame et al., 2016).

## 1.3 EHD protein family

EHD proteins are dynamin superfamily members involved in the regulation of different membrane trafficking pathways at the plasma membrane and internal membranes (Caplan et al., 2002; Grant and Caplan, 2008; Moren et al., 2012). These proteins consist of an N-terminal dynamin-related GTPase domain, a helical domain and a C-terminal EH domain. EHDs are exclusive to eukaryotes, with 4 members in mammalians (EHD1-4) and one in *C. elegans, D. melanogaster, A. thaliana* and some parasites from the genus *Trypanosoma, Plasmodium* and *Toxoplasma* (Daumke et al., 2007). In contrast to the fission and fusion activity observed for most dynamin superfamily proteins, studies of EHDs rather indicated different function in stabilizing membrane curvature, although for some EHDs, membrane fission activity was suggested (Moren et al., 2012; Shah et al., 2014).

### 1.3.1 Cellular functions of mammalian EHDs

Proteins from the EHD family were shown to be important proteins for the regulation and control of endocytic recycling (Naslavsky and Caplan, 2011). In this process, the Early Endosome (EE) is the first compartment on the way of internalized cargo from the plasma membrane (Gruenberg, 2001). The primary function of endocytic recycling is the sorting of internalized cargo to different compartments within the cell (Grant and Donaldson, 2009). These processes occur by mechanisms that include the generation of new lipids on membranes and recruitment of different EHD interaction partners (Giridharan et al., 2013). In this section, the different functions of mammalian EHD proteins in the endosomal compartment will be described.

EHD1 localizes to the Endocytic Recycling Compartment (ERC) and plays an important role on the recycling of cargo from the ERC to the plasma membrane (Grant and Caplan, 2008). It was shown to be involved in the recycling of transferrin and major histocompatibility complex class I (MHC-1) (Naslavsky, 2004), cystic fibrosis transmembrane conductance receptor (CFTR)

(Picciano et al., 2003), AMPA receptor from the ERC to the plasma membrane (Park, 2004) and β1 integrins (Jovic et al., 2007).

EHD2 was shown to localize to caveolar structures at the plasma membrane. Caveolae are flask-like shaped organelles at the plasma membrane involved in regulating membrane homeostasis, signaling and cellular mechanoprotection (Parton and Collins, 2016). EHD2 interacts with some specificity with PIP2-containing membranes, which may contribute to its recruitment to the plasma membrane (Daumke et al., 2007; Simone et al., 2013). It was shown that EHD2 constitutes an important structural component of caveolae and is involved in the control of their stability and turnover (Moren et al., 2012). It also functions in myogenesis and muscle repair (Marg et al., 2012; Posey et al., 2011).

EHD3, as EHD1, localizes to the ERC where is involved on the recycling of receptors from the EE to the ERC or in retrograde transport from the endosomes to the Golgi (Naslavsky et al., 2009). It has also been implicated on the stabilization of tubular recycling endosomes (TRE) (Bahl et al., 2016).

EHD4 was originally identified as Pincher (pinocytic chaperone), due to its involvement in pinocytic endocytosis of functionally specialized NGF/TrkA endosomes (Shao et al., 2002). It localizes to the EE and is involved in the control of trafficking and regulates exit of cargo towards both the recycling compartment and the late endocytic pathway (Sharma et al., 2008).

Thus, a variety of different functions in membrane trafficking have been revealed for EHDs. As outlined in the following, structural studies further contributed to an understanding of the exact role of EHDs in these processes

### 1.3.2 Domain architecture of EHDs

Lee and colleagues first showed for Receptor-mediated endocytosis 1 (Rme-1), the EHD homolog in *C. elegans,* that its GTPase domain can bind and hydrolyze ATP, but not GTP, and that hydrolysis was necessary for oligomerization at endosomes (Lee et al., 2005). Further studies showed that this was a conserved feature of the EHD family (Daumke et al., 2007; Moren et al., 2012; Shah et al., 2014). Daumke and colleagues solved the crystal structure of EHD2 bound to the ATP analogue AMPPNP (Fig. 16B) (Daumke et al., 2007). This work revealed numerous insights into the structure and function of EHD proteins, e.g. the domain architecture, their nucleotide binding mode, the dimerization interface via the GTPase domains, the position of the EH domains and the membrane binding mode (Daumke et al., 2007). In the following sections, structural features of EHD2 will be introduced.

EHD2 has an approximate size of 60 kDa and is composed of a GTPase domain, a helical domain and an EH domain (Fig. 16A) (Daumke et al., 2007).

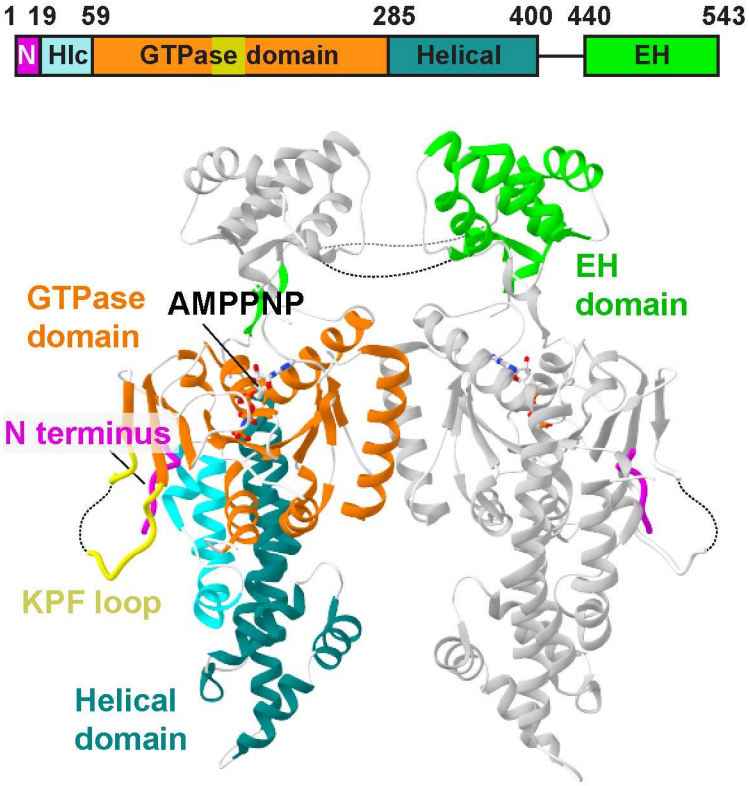


**Figure 16. Structure-based domain architecture of mouse EHD2.** The domain architecture of mouse EHD2, top. Ribbon-type representation of mouse EHD2 dimer bound to the ATP analogue AMPPNP, bottom. The regions not resolved in the crystal structure are indicated by dash lines. The domains of one monomer are labelled and colored according to "A", while the other monomer is colored in gray. In order to facilitate the visualization of the N terminus, it is colored in magenta in both monomers.

The GTPase domain of EHD2 resembles the dynamin GTPase domain fold (Daumke et al., 2007). As in dynamin, the nucleotide is bound via five distinct G-motifs (G1–G5) (Fig. 17) (Daumke et al., 2007). The GTPase domain of EHD2 is bound to AMPPNP (Fig. 17) (Daumke et al., 2007). A methionine which directly follows the G4 motif sterically restricts binding of the amino group of the guanine base. These features may contribute to the specificity for ATP instead of GTP. The GTPase domain contains a unique dimerization interface that is different from the canonical G-interface of dynamin (Daumke et al., 2007).

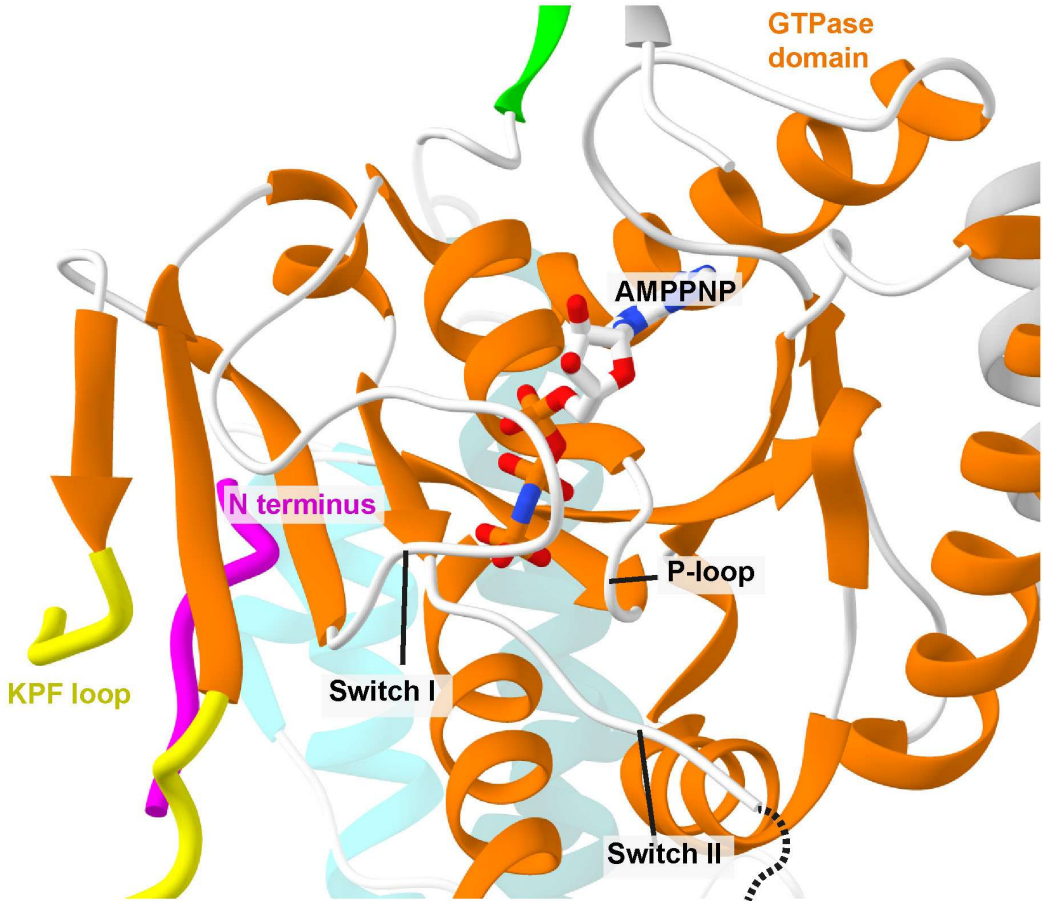


**Figure 17. The nucleotide binding pocket of mouse EHD2.** Details of the interactions of the G-motifs (P-loop, Switch I and II) with AMPPNP (pdb 4CID) are shown. The domains are colored according to (Fig. 16A). The regions not resolved in the crystal structure are indicated by dash lines.

Accordingly, the G–interfaces were not formed in the EHD2 structure, but pointed in opposite directions in the dimer (Fig. 18). At the distal side of the GTPase domain, a unique and highly conserved motif spanning the loop residues 110-135 in EHD2 was first described as KPFxxxNPF motif. Currently, the motif is denominated as KPF loop (Fig. 16-18) which comprises the most highly conserved motif in this loop (Appendix I) (Moren et al., 2012).

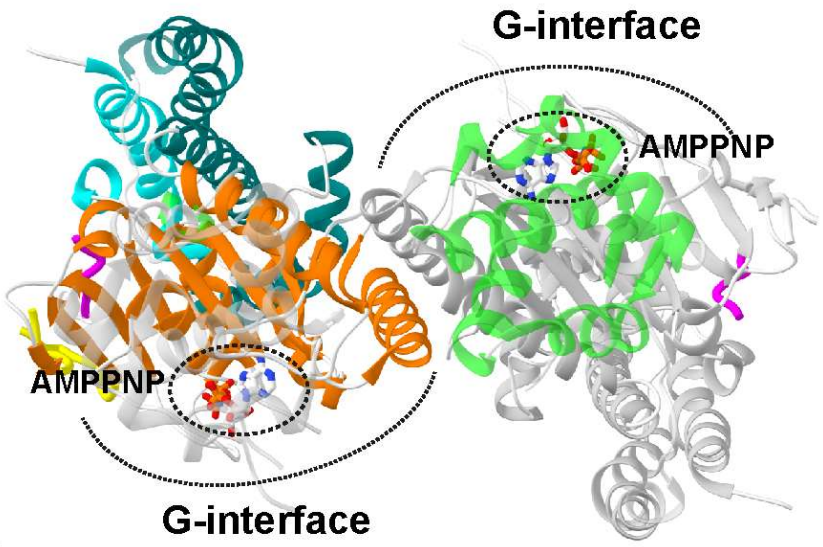


**Figure 18. The G-interfaces of EHD2 point in opposite directions.**
Ribbon-type representation of mouse EHD2 dimer bound to the ATP analogue AMPPNP are depicted from the top. The molecules are colored according to Fig. 16. Note that the nucleotides and the G-interfaces of the monomers point in different directions. This was suggested by Daumke and colleagues to mediate a linear filamentous assembly of the EHD2 dimers upon release of the EH domain (Daumke et al., 2007).

The helical domain is composed of helix α1 and α2 from the N-terminal region and helices α8 to α12 following the GTPase domain (Daumke et al., 2007). The C-terminal EH domain comprises two EF hands (helix-loop-helix motifs) and is known to bind to linear NPF or related motifs via two interaction pockets (Daumke et al., 2007; Kieken et al., 2007). In the EHD2 structure, the EH domains are located on top of opposing GTPase domains and interacts with a Gly-Pro-Phe (GPF) motif at the flexible linker that connects the helical domain to the EH domain (Fig. 19, black box). This linker contains two conserved motifs, GGAFD/E, which is stabilized in a hydrophobic groove of the GTPase domain, and the GPF motif, which interacts with one of the two interacting pockets of the other monomer. The conserved Asp in the G4 motif of EHD2, Asp225, contacts the C-terminal region of the EH domain (Fig. 19, blue box).

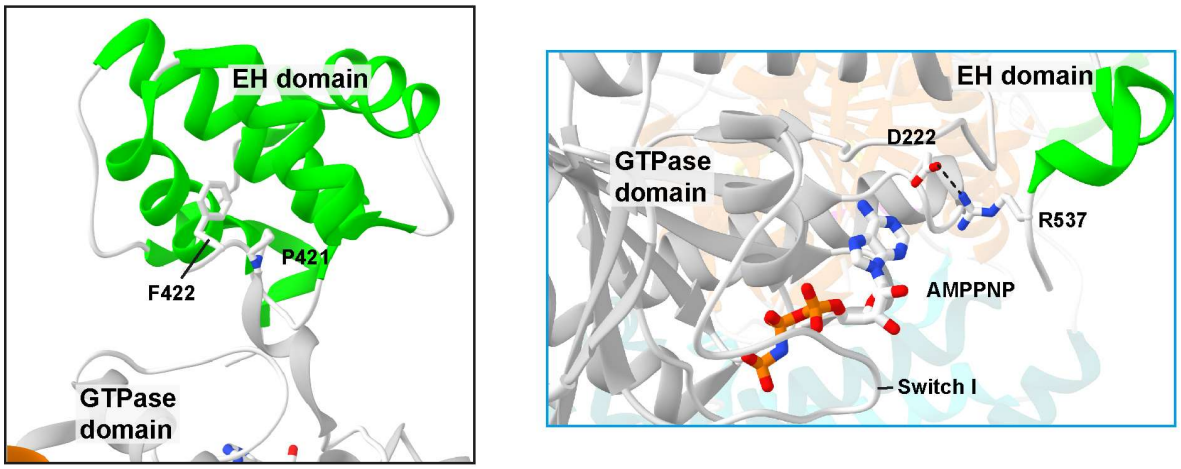


**Figure 19 Interactions of the EH domain in mouse EHD2.** Details of the interactions of the EH domain with the Gly-Pro-Phe (GPF) motif (black box) at the flexible linker that connects the helical domain to the EH domain and of the C-terminal Arg537 with the Asp222 of the G4 motif of the other monomer (blue box) are shown. The domains are colored according to Fig. 16.

In the dynamin superfamily, the EH domain can only be found in the EHD proteins (Naslavsky and Caplan, 2011). It has been suggested to mediate the recruitment of the proteins to different cellular locations. For example, EHD1 was shown to interact with many different proteins involved in the endosomal trafficking, such as Rabenosyn-5 (Naslavsky, 2004), MICAL-L1 (Sharma et al., 2009), PACSIN1 and PACSIN2 (Braun et al., 2005; Giridharan et al., 2013), Rab11-FIP2 (Naslavsky et al., 2006), SNAP29/GS32 (Xu et al., 2004) and the myoferlin homolog Fer1L5 (Posey et al., 2011). EHD2 interacts with the insulin-responsive glucose transporter (GLUT4) in rat adipocytes (Park et al., 2004), EHBP1 (Guilherme et al., 2004), with myoferlin to regulate myoblast fusion (Doherty et al., 2008) and proteins located at caveolae, such as PACSIN2 and Cavin1 (Moren et al., 2012; Senju et al., 2015). EHD3 interacts with PACSIN1 and 2 (Braun et al., 2005), Rab11-FIP2 (Naslavsky et al., 2006) and Ankyrin-B (Gudmundsson et al., 2010). EHD4 interacts with the C terminus of the adaptor protein Numb (Smith, 2004), PACSIN1 and 2 (Braun et al., 2005), type VI collagen (Kuo et al., 2001) and Cadherin 23 in cochlear hair cells (Sengupta et al., 2009). This shows the large number of interactions described for mammalian EHD proteins mainly via the EH domain.

### 1.3.3 Dimerization and oligomerization

In contrast to most dynamin superfamily members, EHD proteins form a stable dimer in solution through a highly conserved interface which is unique to the EHD family (Fig. 20 and Appendix I) (Daumke et al., 2007). The interface involves helix α6 and is formed by conserved contacts involving Trp238, which is buried in a hydrophobic groove at the GTPase domain and between Arg231 and Tyr233 (Daumke et al., 2007).

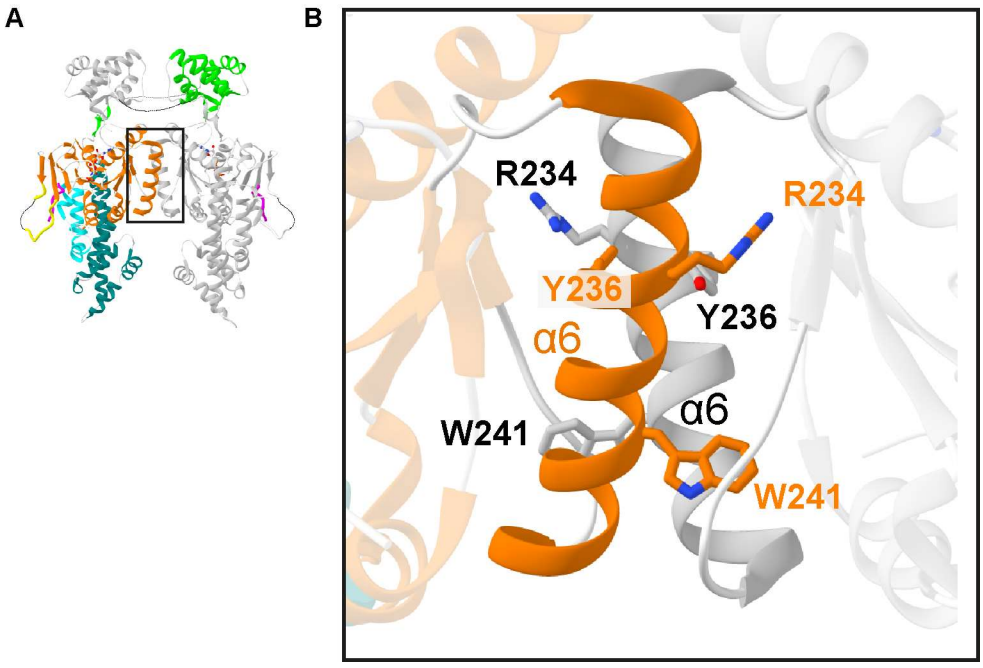


**Figure 20. Dimerization interface of mouse EHD2.** (A) Ribbon-type representation of mouse EHD2 bound to AMPPNP, as shown in Fig. 16. (B) Details of the interactions between helices α6 of the GTPase domains.

Currently, there is no structural data available for the EHD oligomer. The existing oligomerization model is based on the models described for dynamin superfamily proteins and *in vivo* data (Daumke et al., 2007; Moren et al., 2012). During recruitment of dimeric EHD2 to the membrane, it is suggested that the EH domain is released from the top of the opposing GTPase domain monomer to bind to the KPF loop of the next dimer. This release would allow oligomerization via the G–interface and form a scaffold on membranes (Daumke et al., 2007). Later, studies have shown that EHD2 oligomerization is highly dependent on ATP-binding and

on the KPF loop (Moren et al., 2012; Shah et al., 2014). In contrast, the EH domains are not involved in oligomerization of EHD2 (Moren et al., 2012).

### 1.3.4 Membrane binding and remodeling

EHDs oligomerize on membranes in ring-like structures and remodel liposomes *in vitro* into lipid tubules (Daumke et al., 2007; Moren et al., 2012; Pant et al., 2009; Shah et al., 2014). The binding and assembly of the EHD oligomer on liposomes is ATP-binding-dependent and leads to a 10-fold stimulation of its basal ATPase activity (Daumke et al., 2007). This rate is much lower than what is observed for dynamin under similar conditions (Daumke et al., 2007; Faelber et al., 2013). For EHDs, it has been suggested that their membrane remodeling activity can be linked to membrane fission or the stabilization of tubular membrane structures.

Based on the crystal structure of EHD2 bound to AMPPNP, Daumke and colleagues found that residues at the tip of the helical domain are important for membrane interaction (Daumke et al., 2007). Different membrane binding sites were described for EHDs. Shah and colleagues have shown that residues Lys324, Lys327, Lys328, Lys329 and Phe322 at the tip of the helical domain have important roles for lipid binding, since their mutation led to the cytoplasmic distribution of EHD2 in cells and reduced binding to liposomes *in vitro* (Shah et al., 2014). Also, residues at the N terminus were shown to insert into the outer leaflet of the membrane and may create membrane curvature by a wedging mechanism (Campelo et al., 2008; Shah et al., 2014). In another work, the EH domain of EHD1 was shown to bind directly and preferentially to an array of phospholipids, with a preference to phosphatidylinositol-3-phosphate (PIP3). The residue Lys483 on the opposite face of the NPF-binding pocket is critical for this interaction (Naslavsky et al., 2007). Together, these results reveal that EHD proteins interact with membranes via the charged residues at the tip of the helical domain. However, the regulation of of membrane binding is still unclear.

### 1.3.5 Autoinhibition and activation

Recently, it was shown that the deletion of the N-terminal region of EHD2 results on the increase of its membrane recruitment *in vivo* (Shah et al., 2014). In the EHD2 crystal structure, the first 18 N-terminal residues were not included due to the lack of connecting electron density before residue 19 (Daumke et al., 2007). Later, the highly conserved first 8 residues of the N terminus were shown to fold towards a hydrophobic groove at the distal side of the GTPase domain (Fig. 21).

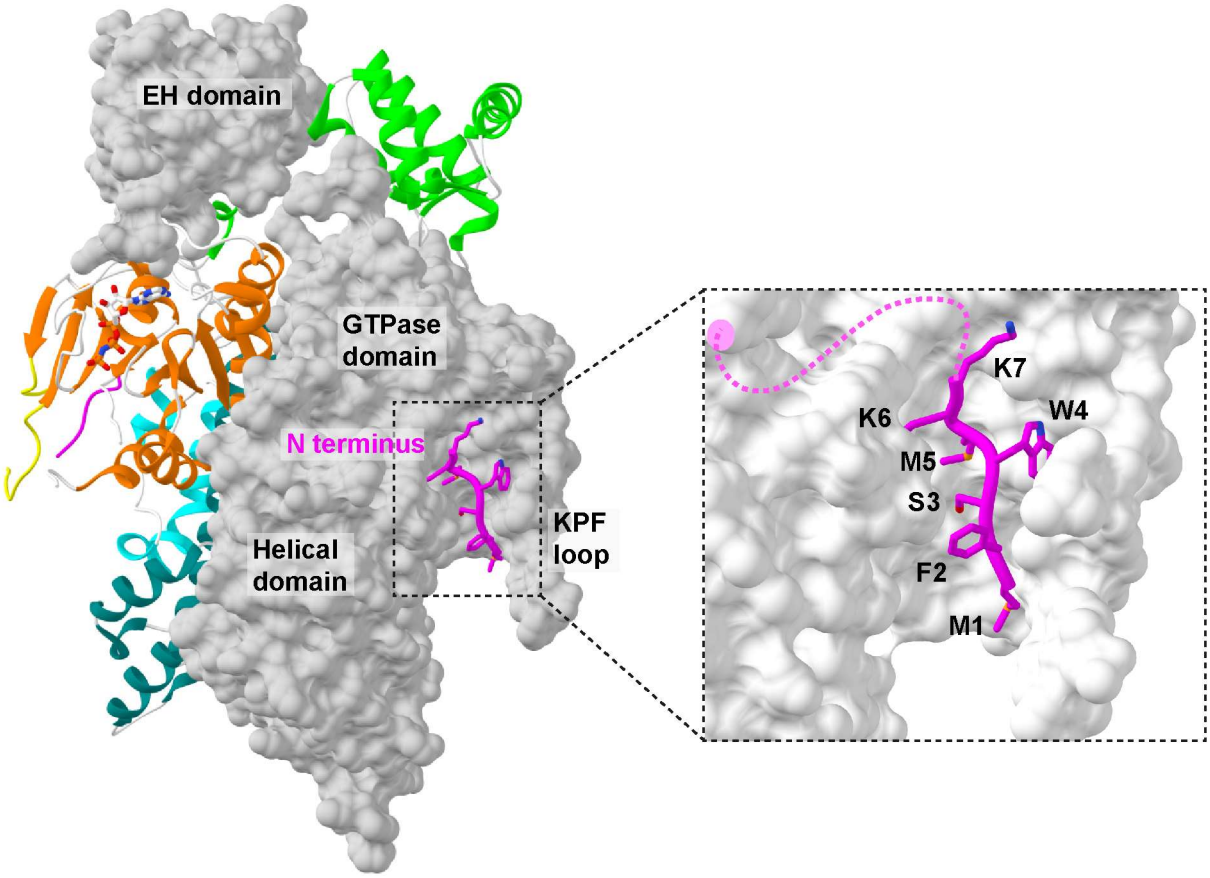


**Figure 21. The N terminus folds inside a hydrophobic groove of the GTPase domain.** Ribbon and surface representation of the EHD2 structure (pdb 4CID) coloured according to Fig. 16. Detailed view of the N terminus (magenta) bound to the hydrophobic groove in the GTPase domain (black box).

In the presence of membranes, those N-terminal residues exit the pocket and are able to insert into liposomes. Counter-intuitively, the release of the N terminus from the hydrophobic pocket, but not its membrane insertion, appears to be responsible for the increased recruitment of EHD2 to the membrane (Shah et al., 2014). This suggests an autoinhibitory role of the N terminus.

The EH domain was also suggested to act as an autoinhibitory module by blocking the further assembly via the G–interface. Its release may be triggered by nucleotide-loading or binding of an interaction partner, therefore allowing the formation of the G-interface and oligomerization (Daumke et al., 2007; Moren et al., 2012; Shah et al., 2014). The involvement of the EH domain and the N terminus on the regulation of EHD2 have been shown, although the mechanism of autoinhibition and activation in EHD proteins remains unclear.

# 2 Scope of the thesis

In the past years, large efforts have been made to determine crystal and cryo-EM structures of dynamin superfamily proteins. Several studies revealed insights into the autoinhibited structures of dynamin and closely related proteins, representing their cytoplasmic, non-oligomerized conformation. In these structures, autoinhibitory domains were shown to bind via intra- or intermolecular interactions to specific sites in the protein, therefore blocking the further assembly. Membrane binding or the binding of interaction partners, in turn, was shown to release the inhibition allowing recruitment and oligomerization. The understanding of such activation mechanisms generates valuable insights into basic mechanisms of cell biology and membrane trafficking.

Autoinhibitory contacts have also previously been described for EHD2, where the N terminus was shown to negatively regulate its membrane recruitment, and the EH domain was suggested to block oligomerization. In this thesis, I aimed to understand the exact structural features of this autoinhibitory mechanism in the EHD family, by elucidating the active form of an EHD protein. To this end, I determined the crystal structure of EHD4 in the absence of the N terminus. Indeed, my structural analyses revealed that the solved EHD4 crystal structure was in an active conformation and elucidated a set of domain movements and rearrangements occurring during activation. These structural data were further corroborated by a set of structure-based functional experiments and eventually resulted in an activation model for EHD proteins. A comparison to other peripheral membrane proteins revealed general insights of how membrane recruitment and oligomerization of such proteins is achieved.

# 3 Materials and methods

## 3.1 Materials

### 3.1.2 Instruments

Instruments used in this thesis are listed in the Appendix B.

### 3.1.3 Chemicals

Chemicals used in this thesis are listed in the Appendix C..

### 3.1.4 Enzymes

Enzymes used in this thesis are listed in Appendix D.

### 3.1.5 Kits

Kits used in this thesis are listed in the Appendix E.

### 3.1.6 Bacteria strains

*E. coli* TG1; *E. coli* Rosetta 2 (DE3)

### 3.1.7 Plasmids

pGEX-6P-1 (AmpR, GE Healthcare); pSKB2-LNB (KanR, based on pET28, Merck, Darmstadt, DE; Multiple Cloning Site (MCS) exchanged against that of pGEX-6P-1, PreScission Protease cleavage site, O. Daumke, MDC-Berlin); pEGFP-C3-MCS (KanR, based on pEGFP-C3, Clontech; MCS exchanged against MCS from pGEX-6P-1, O. Daumke, MDC Berlin); pCMV-Myc (AmpR, Clontech); pmCherry-N1 (KanR, Clontech); pET-46 Ek/LIC (AmpR, Novagen).

#### 3.1.8 Media and Buffers

Media used in this thesis and their composition/ordering numbers are listed in the Appendix F. Buffers and their composition are shown in the Appendix G.

## 3.2 Methods

### 3.2.1 Molecular biology

#### 3.2.1.1 Polymerase Chain Reaction (PCR)

DNA fragments were amplified with KOD Hot Start polymerase (Merck Millipore, DE) according to the manufacturer's procedures.

#### 3.2.1.2 Restriction digest

DNA was digested with restriction endonucleases (Type II) from New England Biolabs (NEB) according to the manufacturer's protocol.

#### 3.2.1.3 Agarose gel electrophoresis

1 % agarose gels were prepared and run according to standard procedures.

#### 3.2.1.4 DNA purification

Excised DNA bands were purified using the QIAquick Gel Extraction Kit (Qiagen) according to the manufacturer's protocol.

#### 3.2.1.5 Ligation

Concentration of plasmids and inserts was determined using the absorption at 259 nm. 10 ng plasmid and a three-fold molar excess of insert were ligated using T4 DNA Ligase from NEB according to the manufacturer's protocol.

#### 3.2.1.6 Preparation of chemically competent *E. coli* cells

Chemically competent *E. coli* bacteria were prepared according to (Chung et al., 1989).

#### 3.2.1.7 Transformation of chemically competent *E. coli* cells

Plasmids were transformed using the heat shock method according to standard protocols. *E. coli* TG1 strain was used for plasmid propagation and *E.coli* Rosetta 2 (DE3) strain for protein expression.

#### 3.2.1.8 Storage of *E. coli* cells

For long-term storage of bacteria, 1 mL of a 5 mL LB overnight bacterial culture was mixed with 0.5 mL sterile glycerol and stored at -80 °C.

#### 3.2.1.9 Site-directed mutagenesis

Site-directed mutagenesis was carried out by QuickChange mutagenesis (Strategene) according to the manufacturer's protocol.

#### 3.2.1.10 Constructs

An overview of the constructs used in this thesis can be found in Appendix H.

### 3.2.2 Protein expression and purification

#### 3.2.2.1 Protein over-expression test

Over-expression of desired constructs were tested by adding a single colony of *E. coli* Rosetta 2 (DE3) containing the plasmid of interest to 5 mL LB medium containing appropriate antibiotics during 16 h at 37°C. 100 µL of the overnight pre-culture was transferred to 5 mL LB containing respective antibiotics for 3 h at 37°C and induced with 100 µM isopropyl β-D-1-thiogalactosidase (IPTG) for 2 h at 37°C. Aliquots were taken before (BI) and after (AI) induction and centrifuged for 2 min at 3000 x g. The pellet was resuspended in 1 X sample buffer, heated for 5 min at 95°C and subjected to SDS-PAGE.

#### 3.2.2.2 Protein solubility test

Constructs were expressed by inoculating 1 L TB with 10 mL of an overnight culture of *E. coli* Rosetta 2 (DE3) containing the expression construct in LB medium containing expression constructs. Cultures were grown at 37 °C until an OD600 of 0.5 and then induced with 40 µM IPTG at 18 °C for 16 h. Cells were pelleted by centrifugation at 4500 rpm for 15 min at 4 °C. Bacterial pellets were resuspended in 30 ml resuspension Buffer /1 L of TB in culture and kept at -20 °C until further use. For solubility test, cells were thawed on ice and lysed in a microfluidizer. Following centrifugation (30,000 g, 1 h, 4 °C), cleared lysates were applied to a NiNTA column. The column was then extensively washed with washing buffer and afterwards the bound protein eluted with elution Buffer. The samples were resuspended in 1 X sample buffer, heated for 5 min at 95°C and subjected to SDS-PAGE.

#### 3.2.2.3 Mus musculus EHD4 protein purification

Mouse EHD4 (residues 22-541, $EHD4^{\Delta N}$) and the indicated mutants were expressed from a modified pET28 vector as N-terminal $His_6$-tag fusions followed by a PreScission protease cleavage site, according to (Daumke et al., 2007). Expression plasmids were transformed in *E. coli* host strain BL21(DE3)-Rosetta2 (Novagen). Cells were grown at 37 °C in TB medium, and protein expression was induced at an optical density of 0.5 by the addition of 40 µM isopropyl-β-D-thiogalactopyranoside (IPTG), followed by overnight incubation at 18 °C. Upon centrifugation, cells were resuspended in Resuspension Buffer and lysed in a microfluidizer. Following centrifugation (30,000 g, 1 h, 4 °C), cleared lysates were applied to a NiNTA column . The column was then extensively washed with Washing Buffer and afterwards with Equilibration Buffer. The protein was eluted with Elution Buffer I. Following addition of 150 µg PreScission protease per 5 mg of EHD constructs, the protein was dialyzed overnight against Dialysis Buffer. Following re-application of the protein to a NiNTA column to remove the His-tag, the protein was eluted with Elution Buffer II. The uncleaved protein was concentrated using 50 kDa molecular weight cut-off concentrators (Amicon) and applied to a Superdex200 gel filtration column equilibrated with SEC Buffer. Fractions containing the EHD constructs were pooled,

concentrated and flash-frozen in liquid nitrogen. The purified protein was nucleotide-free, as judged by HPLC analysis.

### 3.2.3 Crystallization and structure determination

#### 3.2.3.1 Protein crystallization

Initial crystallization trials by the sitting-drop vapor-diffusion method were performed at 20 °C, using a Gryphon LCP pipetting robot and Rock Imager storage system. Subsequently, conditions were refined in the 24-well format using hanging drops.

#### 3.2.3.2 *Mus musculus* EHD4

For the ATPγS-bound structure, 1 µl of mouse EHD4$^{\Delta N}$ at a concentration of 10 mg/ml was mixed with 2 µl of the reservoir solution containing 26% sodium polyacrylate 5100, 200 mM $MgCl_2$, 100 mM HEPES/NaOH (pH 7.5) in the presence of 2 mM ATPγS. For the ADP-bound structure, 1 µl of mouse EHD4$^{\Delta N}$ at a concentration of 10 mg/ml was mixed with 2 µl of the reservoir solution containing 900 mM sodium malonate (pH 7) in the presence of 2 mM ADP. Rod-shaped crystals appeared after one day at 20 °C. Crystals were cryo-protected by transfer into a solution containing 50% of the buffer and reservoir components and 20% glycerol and flash-cooled in liquid nitrogen.

#### 3.2.3.3 Data collection

Data were recorded at beamline BL-14.1 at BESSY-II (Berlin) at a temperature of 100 K and a wavelength of 0.9184 Å. Data from single crystals were processed and scaled using the program package XDS (Kabsch, 2010) and XDSAPP (Krug et al., 2012).

#### 3.2.3.4 Protein structure solution

The structure was solved by molecular replacement with Phaser (McCoy et al., 2007) using the individual GTPase domain and helical domain of EHD2 (pdb 4CID) as search models. The model was built using *Coot* (Emsley et al., 2010) and iteratively refined using Phenix (Adams et

al., 2010) with 3 TLS parameters per molecule. For the ATPγS-bound structure, 96% of all residues are in the most favored regions of the Ramachandran plot and 0.5% in the disallowed regions; for the ADP-bound structure, 93.5% of all residues are in the most favored regions of the Ramachandran plot and 1.1% in the disallowed regions as analyzed with Molprobity (Chen et al., 2010).

#### 3.2.3.5 Structural analysis

Crystal structures were analyzed with PyMOL (Molecular Graphics System Version 1.8, Schrödinger, LLC), Chimera (Pettersen et al., 2004) and *Coot.* The molecular morph was created in Chimera. Domain superpositions were performed with *Coot*. The surface conservation plot was calculated and visualized using Chimera. Sequence alignments were performed with Clustal W (Larkin, 2007). Figures were prepared with PyMOL, Chimera and Blender™.

### 3.2.4 Biochemistry and cell biology

#### 3.2.4.1 Sodium dodecyl sulfate polyacrylamide gel electrophoresis (SDS-PAGE)

Proteins were subjected to SDS-PAGE on a NuPAGE® Novex 4-12 % Bis-Tris gels with 1x MES running buffer or 12 % polyacrylamid SDS gels with 1x SDS running buffer in the Xcell Sure Lock system at 180 V until the bromophenol blue dye reached the bottom of the gel. Gels were stained with a Commassie-based staining Solution and destained with Destaining Solution.

#### 3.2.4.2 Isothermal Titration Calorimetry (ITC)

ITC experiments were performed on a MicroCal VP-ITC by titrating 2mM ATPγS solution into a 70 µM EHD4$^{\Delta N}$ solution. The ATPγS solution was prepared by dissolving it in buffer containing SEC Buffer. The resulting heat changes were integrated and fitted to a quadratic binding model, using the supplied Origin Module.

#### 3.2.4.3 EPR power saturation experiments

These experiments were carried out as described in (Shah et al., 2014) at a concentration of approximately 2 mg/mL. Accessibilities to $O_2$ (from air, $\Pi_{Ox}$) and 10 mM NiEDDA ($\Pi_{NiEDDA}$)

were obtained from power saturation experiments using a Bruker EMX X-Band ESR spectrometer fitted with ER4123D dielectric resonator. The depth parameter Φ was calculated from $\Phi = \ln[\Pi_{Ox}/\Pi_{NiEDDA}]$ (Altenbach et al., 1994). The membrane insertion depth was obtained as described in (Shah et al., 2014).

#### 3.2.4.4 Liposome preparation

Liposomes were prepared by mixing 50 µL of Folch liposomes (total bovine brain lipids fraction I from Sigma) (25 mg/mL) to 200 µL of a Chlorophorm/Methanol (1:0.3 v/v) mixture and dried under Argon stream. The liposomes were resuspended in Liposome Buffer and sonicated in water bath for 30 sec.

#### 3.2.4.5 Liposome cosedimentation assays

Liposomes (2 mg/mL) were incubated at room temperature with 10 µM of the indicated EHD4 construct for 10 min in 50 µl reaction volume, followed by a 213,000 g spin for 10 min at 20 °C. The final reaction buffer contained 25 mM HEPES/NaOH (pH 7.5), 300 mM NaCl and 0.5 mM $MgCl_2$. The supernatant and pellet were subjected to SDS-PAGE.

#### 3.2.4.6 ATP hydrolysis assay

ATPase activities of 10 µM of the indicated EHD4 constructs were determined at 30 °C in ATPase Buffer in the absence and presence of 1 mg/ml non-extruded Folch liposomes, using 100 µM ATP as the substrate. Reactions were initiated by addition of protein to the reaction. At different time points, reaction aliquots were 5-fold diluted in reaction buffer and quickly transferred to liquid nitrogen. Nucleotides in the samples were separated via a reversed-phase Hypersil ODS-2 C18 column (250 × 4 mm) with HPLC Buffer. Denatured proteins were adsorbed on a C18 guard column. Nucleotides were detected by absorption at 254 nm and quantified by integration of the corresponding peaks. Rates were derived from a linear fit to the initial reaction (<40% ATP hydrolyzed).

### 3.2.4.7 Electron microscopy

For membrane tubulation assays, 10 µM EHD4$^{\Delta N}$ in Tubulation Buffer were incubated at room temperature for 20 min with 1 mg/ml liposomes. Samples were spotted on carbon-coated copper grids and negatively stained with 2% uranyl acetate. Electron grids were imaged with a transmission electron microscope at 80 kV and acquisition was done with a CCD camera.

### 3.2.4.8 Cell biology and microscopy

These experiments were conducted by our collaboration partner Elin Larsson at the University of Umeå. HeLa cells were grown in DMEM medium supplemented with 10% foetal bovine serum. EHD4-mCherry constructs were transiently transfected before the experiment. Images were acquired with a Zeiss Cell Observer Spinning Disk Confocal controlled by ZEN interface with an Axio Observer Z1 inverted microscope, equipped with a CSU-X1A 5000 Spinning Disk Unit and a EMCCD camera iXon Ultra from ANDOR. For epifluorescence analysis, cells were fixed in 3% paraformaldehyde in PBS for 20 min at RT, then washed and blocked in 5% goat serum with 0.05% saponin in PBS before staining with mouse anti-EEA1 (clone 14, 610456, BD Biosciences) in 1% goat serum, 0.05% saponin in PBS using standard protocols. Images were acquired using a Zeiss Axio Imager Z1 system with Zen software. The representative microscopic images were cropped using ImageJ (NIH). The standard deviations of the image histogram from maximum intensity projections of confocal stacks were used to measure the textures of the different mutants. A ROI of fixed size was applied within an area with representative texture and the standard deviations of the grey values were measured using ImageJ. Statistical analysis was performed using Prism5 (GraphPad Software).

# 4 Results

## 4.1 The N terminus acts as an autoinhibitory module

The N terminus of EHD2 has been shown to negatively regulate its recruitment to caveolae (Shah et al., 2014). Accordingly, deletion of EHD2 N terminus results in increased localization to caveolae suggesting that it negatively regulates membrane recruitment of EHD2 (Shah et al., 2014). To test if such mechanisms exists for EHD4, mCherry-tagged EHD4$^{\Delta N}$ was transfected into HeLa cells, imaged and quantified as described in section 3.2.4.8. mCherry-tagged-EHD4$^{fl}$ served as the control. The deletion of the N terminus resulted in an increased membrane association. Many of the EHD4 positive membranous structures appeared tubulated, suggesting a high membrane remodeling activity of the EHD4$^{\Delta N}$ construct (Fig. 22). This suggests for EHD4 a similar autoinhibitory mechanism of the N terminus as for EHD2.

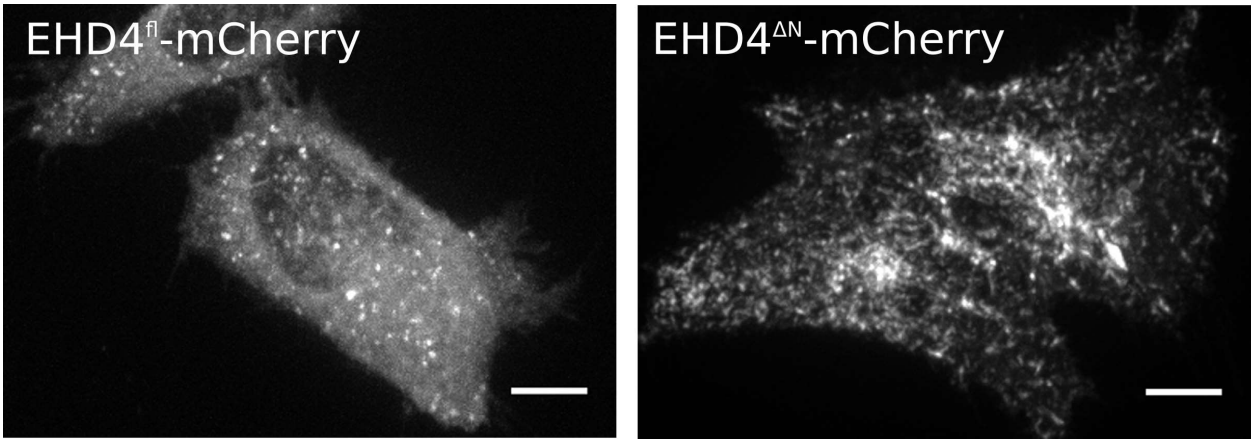


**Figure 22. N terminus negatively regulates EHD4 recruitment to membranes.** EHD4 full length and ΔN constructs were overexpressed in HeLa cells with a C-terminal mCherry tag. Deletion of the N terminus (right) increased punctate and tubular-like structures with increased membrane recruitment of the ΔN construct (right) in comparison to the full length (left). Scale bars: 10 µm. These experiments were conducted by our collaboration partner Elin Larsson with plasmids provided by me.

To determine if the increased membrane association of the N-terminally truncated EHD4 constructs also resulted in an increased recruitment to EE, EHD4$^{fl}$- and EHD4$^{\Delta N}$-mCherry

constructs were transfected into HeLa cells, immunostained against EEA1 (Early Endosome Antigen-1) and imaged as described in sections 3.2.4.8. Indeed, concomitant with increased membrane association, EHD4$^{\Delta N}$ also showed increased co-localization with EEA1, indicating an increased recruitment to EE in the absence of the N terminus (Fig. 23).

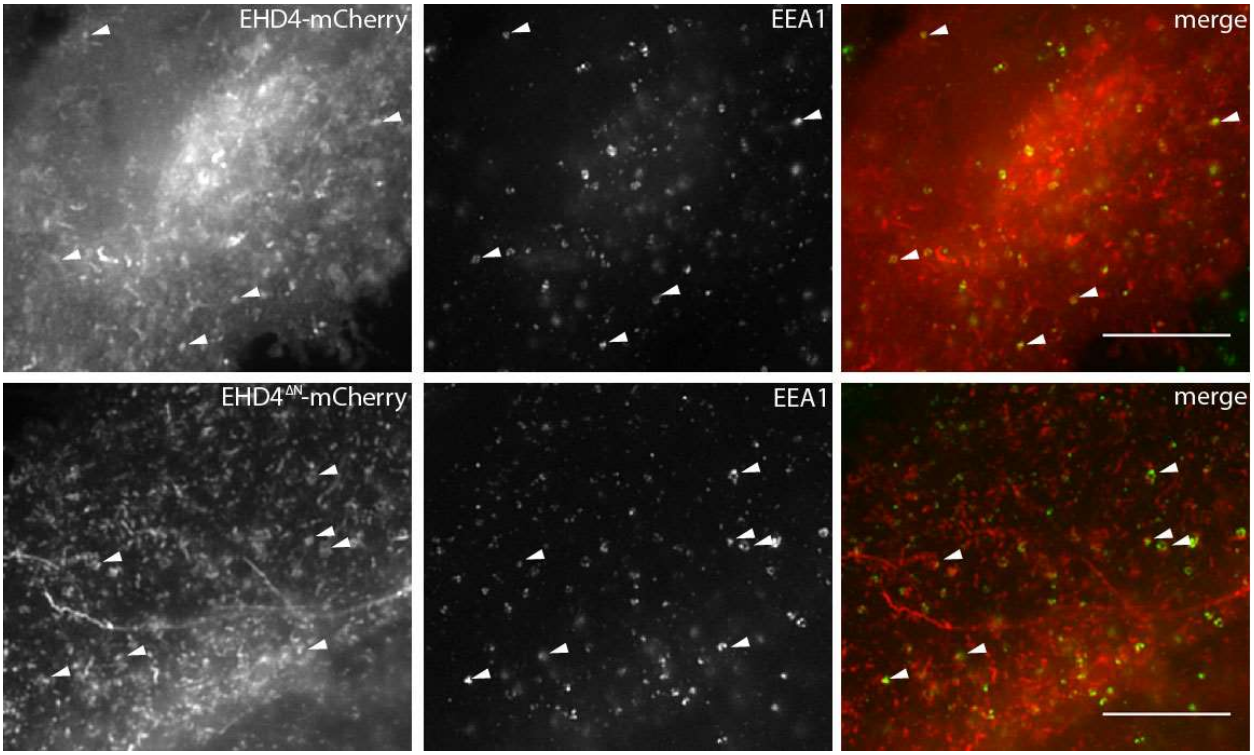


**Figure 23. Increased association of EHD4 to Early Endosomes upon N terminus deletion.** EHD4 fl and ΔN constructs were overexpressed in HeLa cells with a C-terminal mCherry tag and immunostained for endogenous EEA1. Deletion of the N terminus (bottom) increased membrane association and co-localization with Early Endosomes. Arrowheads exemplify co-localization of mCherry-tagged protein and EEA1. Scale bars: 10 µm. These experiments were conducted by our collaboration partner Elin Larsson with plasmids provided by me

In conclusion, EHD2 and EHD4 appear to use related mechanisms for regulating their membrane recruitment. In particular, the N-terminal residues appear to play an important role in regulating the recruitment of EHD2 and EHD4 to membranes by acting as an inhibitory domain when bound to the GTPase domain.

## 4.2 Establishing a purification protocol for EHD4

The N terminus of EHD family proteins is highly conserved in its sequence (Appendix H). Previous studies of EHD2 have shown that it folds back into a hydrophobic groove within the GTPase domain (Fig. 21). Moreover, it was shown that in the presence of liposomes the N terminus of EHD2 is released and can insert into membranes (Shah et al., 2014). The absence of the N terminus increases membrane recruitment in EHD2 and EHD4, which could indicate an activation upon N terminus insertion into the membrane.

To obtain insights into the putative activation mechanism of EHD proteins and mimic the situation where the N terminus is released from the GTPase domain, constructs of mouse (mm) EHD1, human (hs) EHD3 and mmEHD4 with N terminal deletions were expressed and purified as described in section 3.2.2 (Fig. 24). Purifications of the constructs were carried out in 500 mM NaCl to prevent precipitation at protein concentrations higher than 10 mg/mL. The EHD4$^{\Delta N}$ construct was chosen as the target construct due to its high expression yield and high stability. In contrast, EHD4 full length was insoluble under the same conditions.

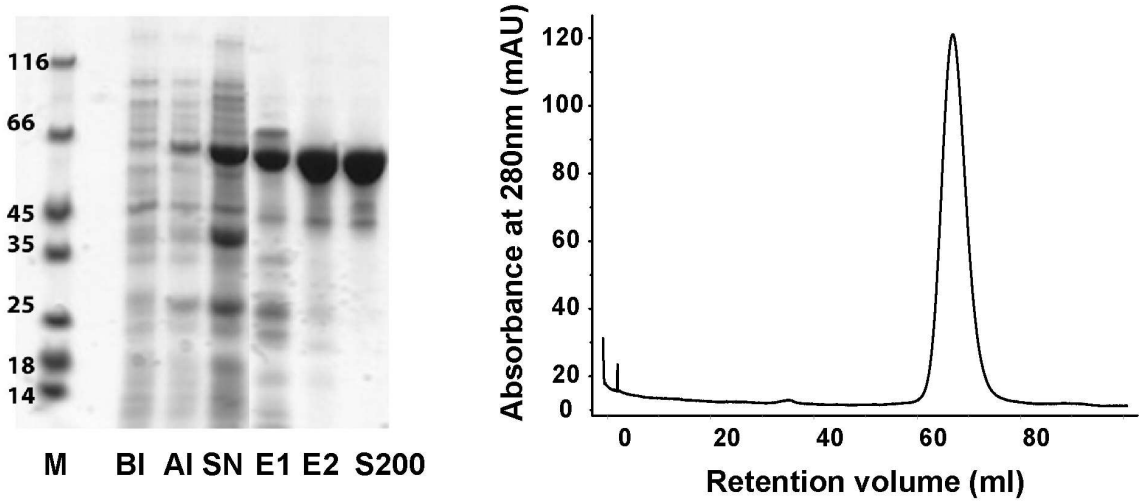


**Figure 24. Purification of the mmEHD4$^{\Delta N}$ construct.** Mouse EHD4 was expressed in *E. coli* as a His-fusion protein as described in section 3.2.2. (Left) SDS-PAGE of the purification of the mmEHD4$^{\Delta N}$ construct. M - Molecular Marker (kDa); BI - Culture before induction with IPTG; AI - Culture after induction with IPTG; SN - Soluble extract; E1 – EHD4 after elution from NiNTA-Sepharose; E2 – EHD4 after reapplication and elution from the NiNTA column; S200 - Purified EHD4 by size exclusion chromatography. Right: Size exclusion chromatography elution profile of the mmEHD4$^{\Delta N}$ construct which eluted in a discrete peak (Superdex 200 16/60).

## 4.3 Biochemical characterization of EHD4$^{\Delta N}$ construct

To biochemically characterize the EHD4$^{\Delta N}$ construct, nucleotide binding, membrane interaction, ATPase activity and membrane remodeling assays were performed. To determine if EHD4$^{\Delta N}$ was able to bind to ATP, an ITC experiment was performed by titrating the EHD4$^{\Delta N}$ construct with a nonhydrolyzable ATP analogue, ATPγS, as described in section 3.2.4.2. EHD4$^{\Delta N}$ bound to ATPγS with an affinity of 77 µM and a binding number of n=0.67 (Fig. 25A). In comparison, EHD2 binds ATP with a Kd of 13 µM. However, the affinity of EHD4 to ATP could be higher since high salt concentration (500 mM NaCl) had to be used in these experiments to prevent protein precipitation.

EHD2 was shown to bind to membranes via its helical domain independently from its nucleotide loading state. To test whether EHD4$^{\Delta N}$ also interacted with membranes, a liposome co-sedimentation assay was performed using liposomes derived from bovine brain (Folch) lipids as described in section 3.2.4.5. The construct cosedimented with liposomes, indicating that it can also interact *in vitro* with Folch liposomes (Fig. 25B).

EHD2 and other dynamin-related proteins display a stimulated nucleotide hydrolysis upon incubation with membranes (Daumke et al., 2007; Faelber et al., 2011). To determine the ATP hydrolysis rate in the presence and absence of membranes, the protein was incubated with ATP and Folch liposomes and ATPase rates were measured by an HPLC-based approach, as described in section 3.2.4.6. The ATPase activity of EHD4 was 200-fold stimulated upon addition of Folch liposomes (Fig. 25C). The stimulated ATPase rate of EHD4$^{\Delta N}$ was seven fold higher when compared with EHD2 under identical conditions.

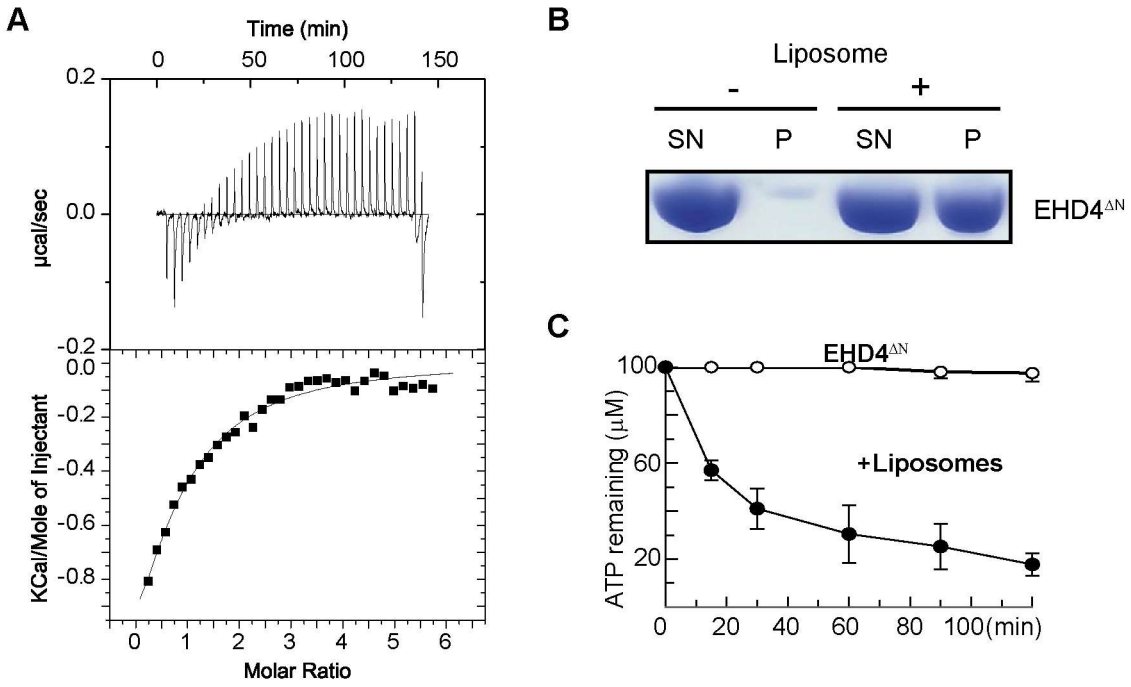


**Figure 25 Biochemical characterization of the EHD4$^{\Delta N}$ construct.** (A) EHD4$^{\Delta N}$ construct binds to ATPγS. In ITC experiments, a 2 mM ATPγS solution was titrated into a 70 µM EHD4$^{\Delta N}$ solution. The resulting heat changes were integrated and fitted to a quadratic binding model. A $K_D$ of 77 µM, with a binding number n of 0.67 was obtained. (B) Binding and cosedimentation with Folch liposomes. Liposome cosedimentation assay was performed in the presence and absence of Folch liposomes. SDS-PAGE result shows the soluble (-)/unbound (+) fraction in the supernatant (SN) and precipitated (-)/bound (+) fraction in the pellet (P). (C) Stimulated ATP hydrolysis of the EHD4$^{\Delta N}$ upon addition of Folch liposomes. ATPase assay was performed by mixing 10 µM of the EHD4$^{\Delta N}$ construct with ATP in the absence and presence of Folch liposomes and measuring the ratio ATP/ADP in solution. After 120 min of incubation, the construct hydrolyzed over 5 % of the ATP in solution in the absence of liposomes and 80 % in the presence Folch liposomes.

To determine if the enhanced EHD4$^{\Delta N}$ ATP hydrolysis rate is accompanied by membrane remodeling as observed for related dynamin family proteins, electron microscopy of EHD4 with Folch liposomes was used (section 3.2.4.7). In the absence of nucleotide, EHD4$^{\Delta N}$ bound to liposomes, but it did not tubulate them. In contrast, the addition of ATP or ATPγS resulted in membrane binding and remodeling activity of Folch liposomes. The protein tubulated vesicles of 800 nm in diameter into 80-100 nm wide tubules. In addition, EHD4$^{\Delta N}$ formed a regular and stable protein coat with apparent striations on the lipid tubule showing a diagonal pattern (Fig. 26).

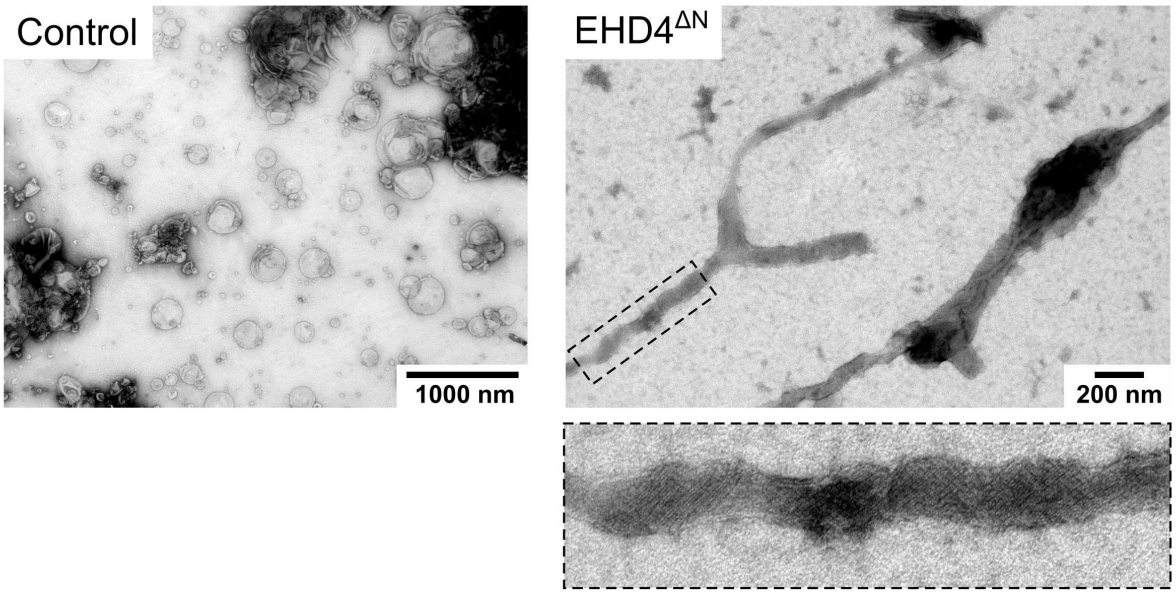


**Figure 26. EHD4$^{\Delta N}$ tubulates liposomes in the presence of ATPγS.** A membrane tubulation assay was performed by incubating EHD4$^{\Delta N}$, ATPγS and non-extruded liposomes for 20 min at RT. The samples were then analyzed by electron-microscopy using negative-staining grids prepared with 2 % uranyl acetate. In the absence of proteins, the liposomes have a round shape (left). In the presence of ATPγS, EHD4$^{\Delta N}$ tubulated liposomes (right) by forming high-order oligomers around them (see box for magnification).

In summary, these results reveal that EHD4 binds and hydrolyzes ATP, and perhaps uses the energy of ATP-binding to perform mechanical work related to membrane remodeling. Furthermore, the slow ATPase rate of EHD4 is 200-fold stimulated in the presence of membranes.

## 4.4 Structure determination of the EHD4$^{\Delta N}$ bound to ATPγS

To gain structural understanding of EHDs' active conformation EHD4$^{\Delta N}$ was crystallized in the presence of the non-hydrolyzed ATP analogue, ATPγS. Crystals were obtained using polyacrylate as the precipitant (see section 3.2.3.2*)* (Fig. 27) and reached their maximal size of 400 x 20 x 20 µm$^3$ after 1 day at 20 °C. They were transferred into a cryo solution containing glycerol (see section 3.2.3.2) and flash-cooled in liquid nitrogen

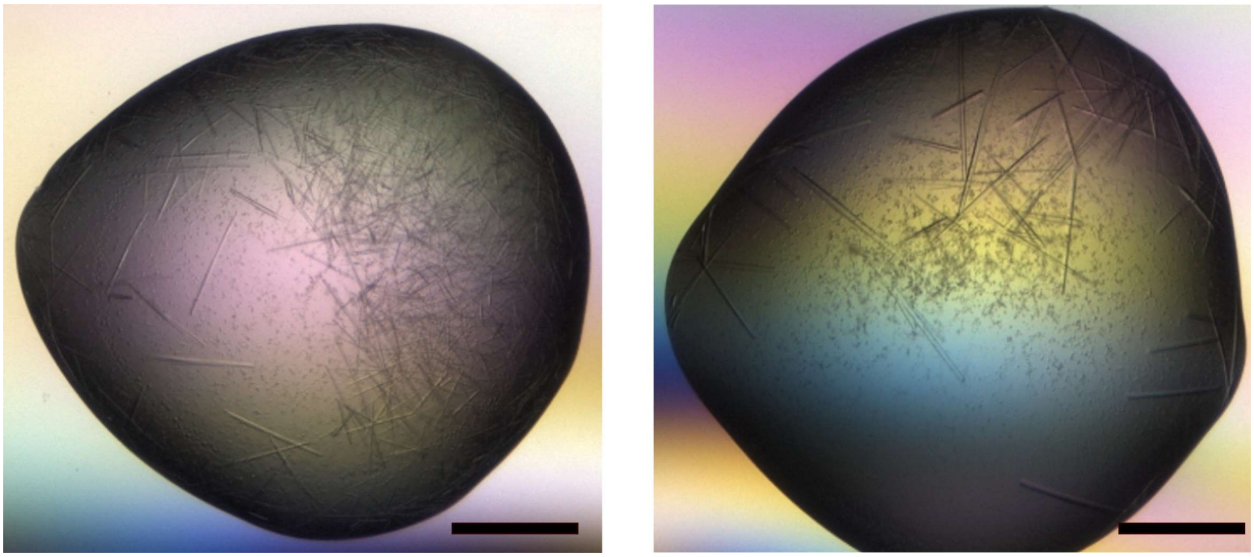

**Figure 27. Initial crystals of EHD4$^{\Delta N}$ bound to ATPγS.** Crystals were grown in 96 well-plate using the sitting-drop method. 200 nl of the reservoir solution containing containing 26% (wt/vol) sodium polyacrylate 5100, 200 mM $MgCl_2$, 100 mM Hepes/NaOH (pH 7.5) was mixed to 200 nl of the 10 mg/ml of the protein in the presence of 2 mM ATPγS and incubated for 1 day at 20 °C. Crystals were then optimized in 24 well-plate using the hanging-drop method with 2 µl drop size. Scale bars: 200 µm.

## 4.5 Structure determination

Datasets of native EHD4$^{\Delta N}$ ATPγS-bound crystals were collected at the BESSY-II electron storage ring, beamline 14.1 in Berlin-Adlershof (section 3.2.3.3). Native crystals diffracted to a maximal resolution of 2.8 Å and had a tetragonal space group $P4_22_12$ with unit cell dimensions of 199.97 X 199.97 X 41.54 Å$^3$. Assuming one molecule in the asymmetric unit, a Matthew coefficient of 3.50 Å$^3$/Da was calculated, indicating approximately 65% solvent content in the crystal. Data collection statistics of native crystals are summarized in Table 1.

**Table 1. Data collection statistics for mouse EHD4$^{\Delta N}$ bound to ATPγS**

| Data collection | EHD4$^{\Delta N}$-ATPγS |
|---|---|
| Wavelength (Å) | 0.918409 |
| Space group | $P4_22_12$ |
| Cell dimensions | |
| *a*, *b*, *c* (Å) | 199.97, 199.97, 41.54 |
| α, β, γ (°) | 90, 90, 90 |
| Resolution (Å) | 48.5-2.79 (2.96-2.79)* |
| $R_{merge}$ (%) | 9.5 (91.9) |
| $I / \sigma I$ | 20.0 (1.9) |
| Completeness (%) | 99.8 (98.6) |
| Redundancy | 7.2 |

The structure was solved by molecular replacement using separate GTPase and helical domains of EHD2 (pdb 4CID) as search models. After an initial round of rigid body refinement, the model was rebuilt in *Coot* with alternating cycles of refinement in *Phenix* with three translation, libration and screw-rotation (TLS) parameters per molecule. The electron density indicated one molecule in the asymmetric unit with clear density for the GTPase domain and helical domain. In the molecular replacement attempts the EH domain was placed at many possible sites, but no significant electron density appeared after several refinements.

Since the construct contained the EH domain, no proteolytic degradation occurred in the crystals it is likely that it is not stabilized on top of the GTPase domain as in EHD2 and it is likely disordered in the crystals. Apart from the protein molecule, 21 water, 1 magnesium ion and 1 ATPγS molecules were included in the final model. The model has an R-work of 22.7 % and an R-free of 24.3 %. In the Ramachandran plot of the model 96 % of all residues are in the most favored regions, pointing to a well refined geometry. Refinement statistics are summarized in Table 2.

**Table 2. Refinement statistics for mouse EHD4$^{\Delta N}$ bound to ATPγS**

| Refinement | EHD4$^{\Delta N}$-ATPγS |
|---|---|
| Resolution (Å) | 48.5-2.79 (2.89-2.79) |
| No. reflections | 21,733 (2,091) |
| $R_{work}$ / $R_{free}$ (%) | 22.7/24.3 (32.8/34.2) |
| **No. atoms** | |
| Protein | 3,072 |
| Ligand/ion | 32 |
| Water | 21 |
| ***B*-factors (Å$^2$)** | |
| Protein | 75.6 |
| Ligand/ion | 100.3 |
| Water | 49.6 |
| **R.m.s. deviations** | |
| Bond lengths (Å) | 0.002 |
| Bond angles (°) | 0.54 |

## 4.6 Overall architecture of the EHD4$^{\Delta N}$ ATPγS-bound structure

The overall architecture of ATPγS-bound EHD4$^{\Delta N}$ reveals a canonical GTPase and helical domain that are characteristic of dynamin proteins (Fig. 28). The GTPase domain of EHD4 has a typical GTPase domain fold with a central β-sheet surrounded by α-helices. One molecule of ATPγS occupies the canonical nucleotide-binding pocket. The switch II region is not well ordered (Fig. 28).

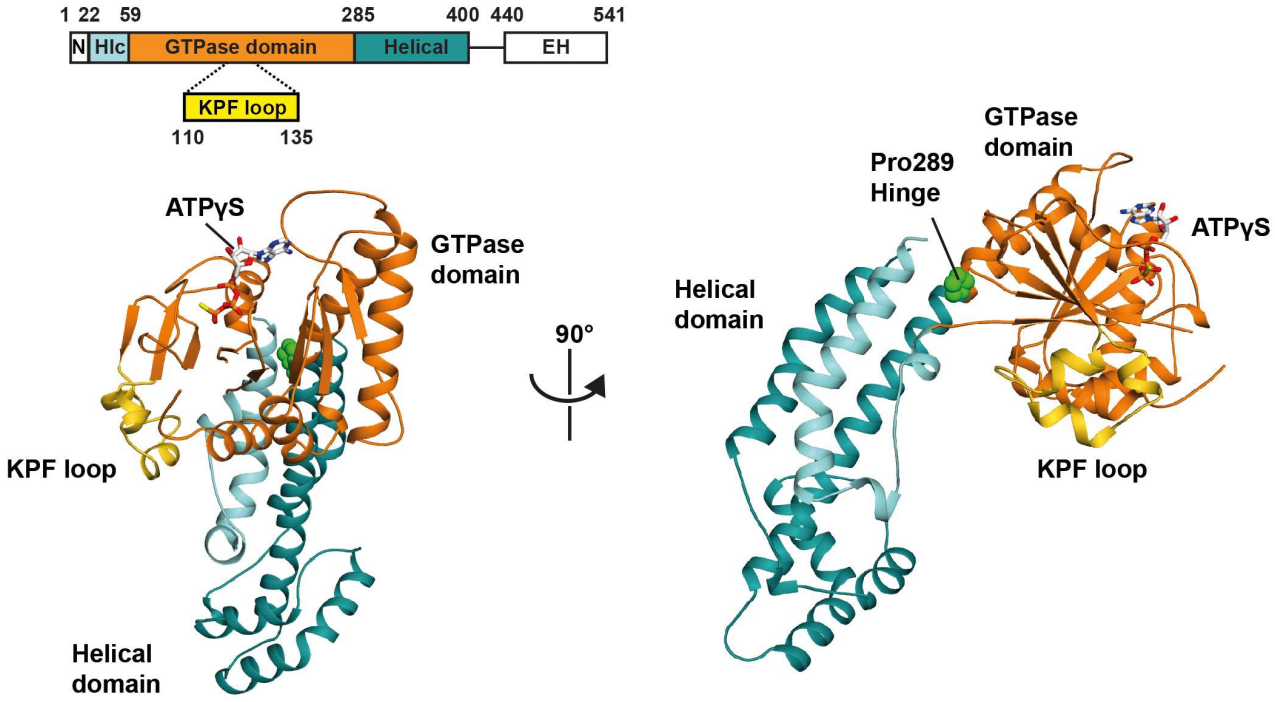


**Figure 28. Crystal structure of the EHD4$^{\Delta N}$ bound to ATPγS.** Domain architecture of the mouse EHD4 (top). Crystal structure of the monomeric EHD4$^{\Delta N}$ bound to ATPγS in ribbon-type representation is depicted from a front (left) and side (right) point of view. The protein is colored according to domain architecture (top). The GTPase domain (orange) is bound to ATPγS (represented as sticks). The helical domains are colored in cyan (N-terminal) and dark cyan (C-terminal). The conserved hinge region, Pro289, is shown in green and the conserved KPF loop is shown in yellow. Note that the EH domain is not shown in the structure because it is flexible within the crystal.

The GTPase domain of EHD4 contains all the canonical G motifs (G1-G5) involved in nucleotide-binding (Fig. 29). The main chain of Ser71 in the P-loop (G1) interacts with the β-phosphate of the ATPγS. Thr75 in the P-loop and Asp156 in the switch II (G3) bind to the $Mg^{2+}$ ion, which is crucial for nucleotide hydrolysis. Thr97 in the switch I (G2), also important for nucleotide hydrolysis, adopts an unusual conformation and points away from the nucleotide, therefore it does not interact with the $Mg^{2+}$ ion (Fig. 29). The switch II region adopts a flexible conformation and only the N-terminal part of it was resolved in the electron density. Lys223 in the G4 motif interacts with the ribose of the ATPγS molecule while Ser259 in the G5 motif interacts with the amino group of the adenine. The residue Asp225 in the G4 motif, which is responsible for mediating the specificity to the guanine base of the GTP in GTPases, does not interact with the adenosine ring. The G5 motif sequence differs among the dynamin superfamily members, but is a highly conserved within the EHD family (Appendix I). Trp261 of the G5 motif

contacts the adenosine ring through aromatic stacking interactions (Fig. 29). An overview of the nucleotide interactions are depicted in Fig. 29.

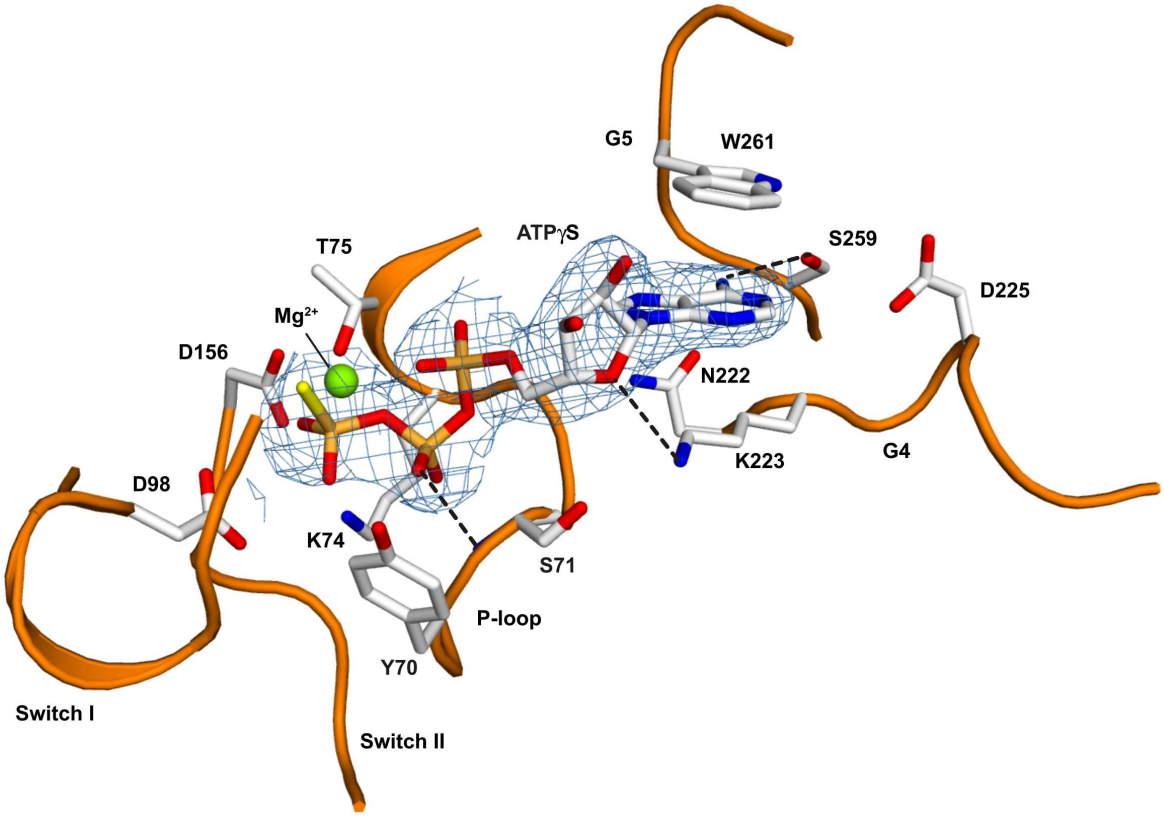


**Figure 29. Structural details of the nucleotide binding pocket in complex with ATPγS.** Detailed view into the catalytic site of the ATPγS structure, with selected residues from the five conserved nucleotide binding motifs (G1-G5) shown in stick representation. Selected hydrogen bonds are indicated by dashed lines. The final 2Fo-Fc density was contoured at 1 σ around the nucleotide.

The EHD4 molecule is a dimer in solution (Fig. 24) which is formed by a conserved interface involving helix α6 (Fig. 30B and D). Curiously, the G-interfaces of the dimer, as well as the nucleotides, point in opposite directions (Fig. 30C) .The dimer in the EHD4$^{\Delta N}$ structure corresponds to a crystallographic two-fold axis and dimerization is mediated by a highly conserved interface. This interface involves a set of hydrophobic interactions between Trp238 and residues from the adjacent monomer. Further interactions between the Arg234 and Tyr236 help to stabilize the dimer (Fig. 30D). This interface is a highly conserved in the EHD family and has already been observed in the EHD2 crystal structure (Appendix I).

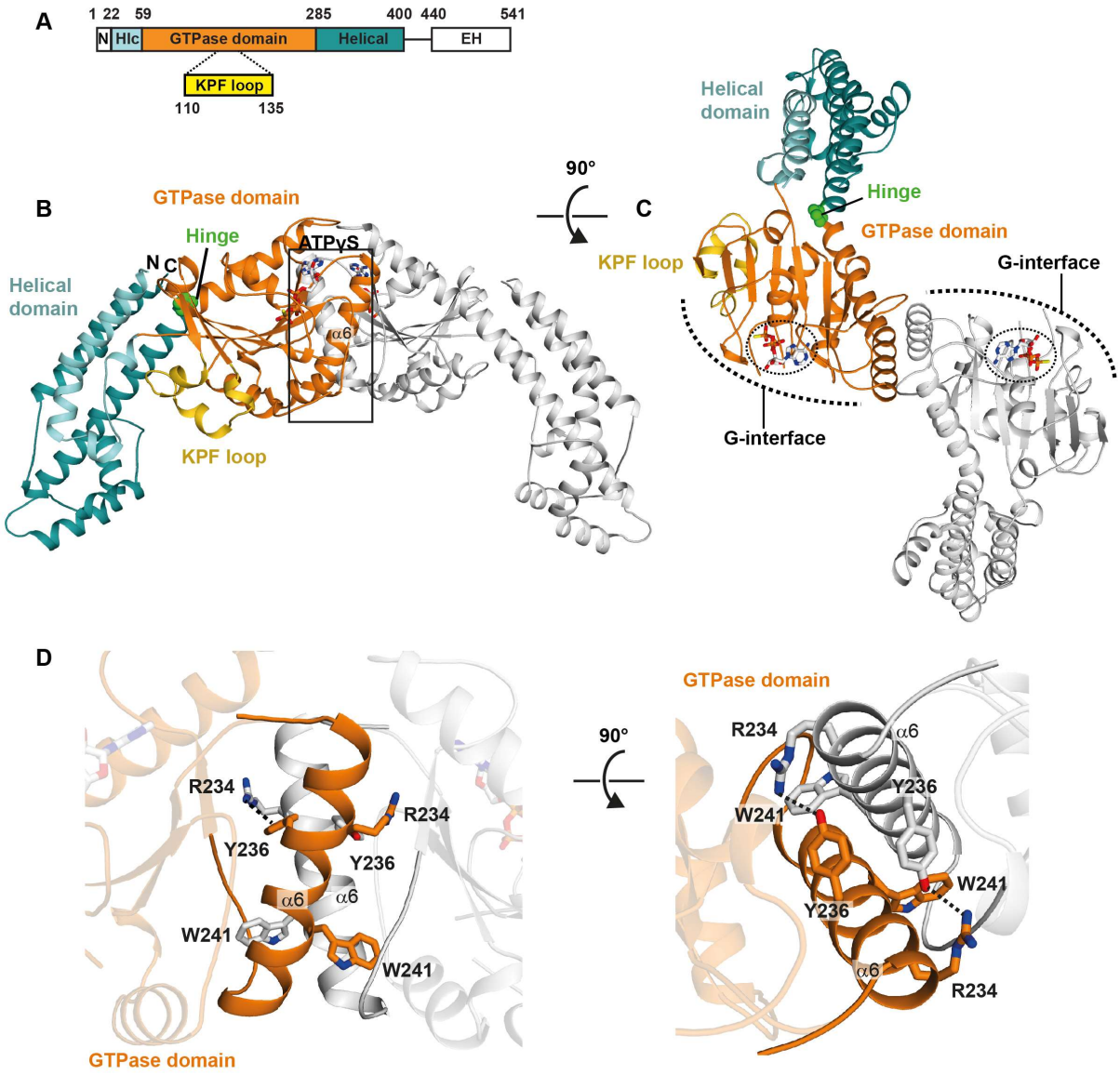


**Figure 30. Structural determinants of dimerization in the GTPase domain.** (A) Domain architecture of EHD4. The colored domains represent the domains solved in the structure. (B-C) The EHD4 dimer structure is shown as a ribbon-type representation in a side (B) and top (C) point of view. One monomer is colored according to "A" and the other in gray. The dimer is formed by an interface involving helix α6 (D) which is stabilized through charged and hydrophobic interactions. Hydrogen bonds are shown as dash lines.

The helical domain of EHD4$^{\Delta N}$ has an almost identical architecture as its counterpart in EHD2 (rmsd of 0.67 Å for 142 Cα atoms). The helical domain is composed of helix α1 and α2 from the N-terminal region and helices α8 to α12 from the C-terminal region of the GTPase domain (Fig. 30B). Although it has a similar fold to EHD2, the helical domain of EHD4 differs in its position

in relation to the GTPase domain (Fig. 30B and C). This feature will be presented in the following section.

## 4.7 Rotation of the helical domain allows membrane binding

A comparison to the EHD2 structure reveals significantly differences. The helical domains have an identical fold to EHD2, but are rotated in relation to the GTPase domain (Fig. 31A). The KPF loop is completely folded and undergoes a major conformational change. The EH domain is displaced from its autoinhibitory site and could not be resolved in the structure (Fig. 30A-C). To determine the structural relation between EHD2 and EHD4, a structural alignment was done by aligning the GTPase domain of the monomer using *Coot*. The comparison to the EHD2 structure revealed that the helical domain of EHD4 is rotated by ~50° relative to the GTPase domain around a hinge featuring Pro289 (Fig. 31A), a conserved residue in EHD proteins (Fig. 31B). This residue is in many dynamin superfamily proteins and corresponds to Pro294 in dynamin, which mediates the rotation of the BSE in relation to the GTPase domain.

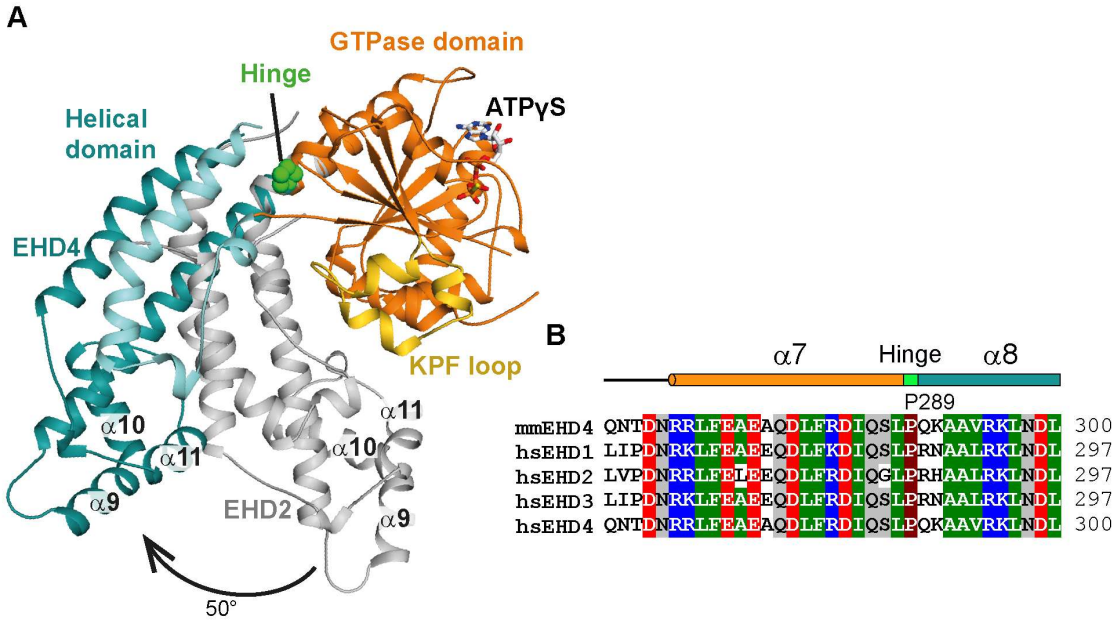


**Figure 31. The helical domain is rotated relative to the GTPase domain in EHD4.** (A) Superposition of the GTPase domains of ATPγS-bound EHD4$^{\Delta N}$ (colored) and AMPPNP-bound EHD2 (pdb 4CID), only the helical domain of EHD2 is shown (gray). The conserved Pro289 acts as the hinge for a 50° rotation of the helical domain. (B) Sequence alignment of human EHD1-4 and the mouse EHD4. Note the conserved Pro289 between the helices α7 and α8.

Rotation of the helical domain pushes the N-terminal residues of the linker to the EH domain 12 Å away (Fig. 32A). In the EHD2 structure, the linker makes prominent contacts to the GTPase domain and binds via a GPF motif to the EH domain of the opposing monomer (Fig. 32B-C). The rotation may thus displace the linker, therefore releasing the EH domain from its autoinhibitory site (Fig. 32C).

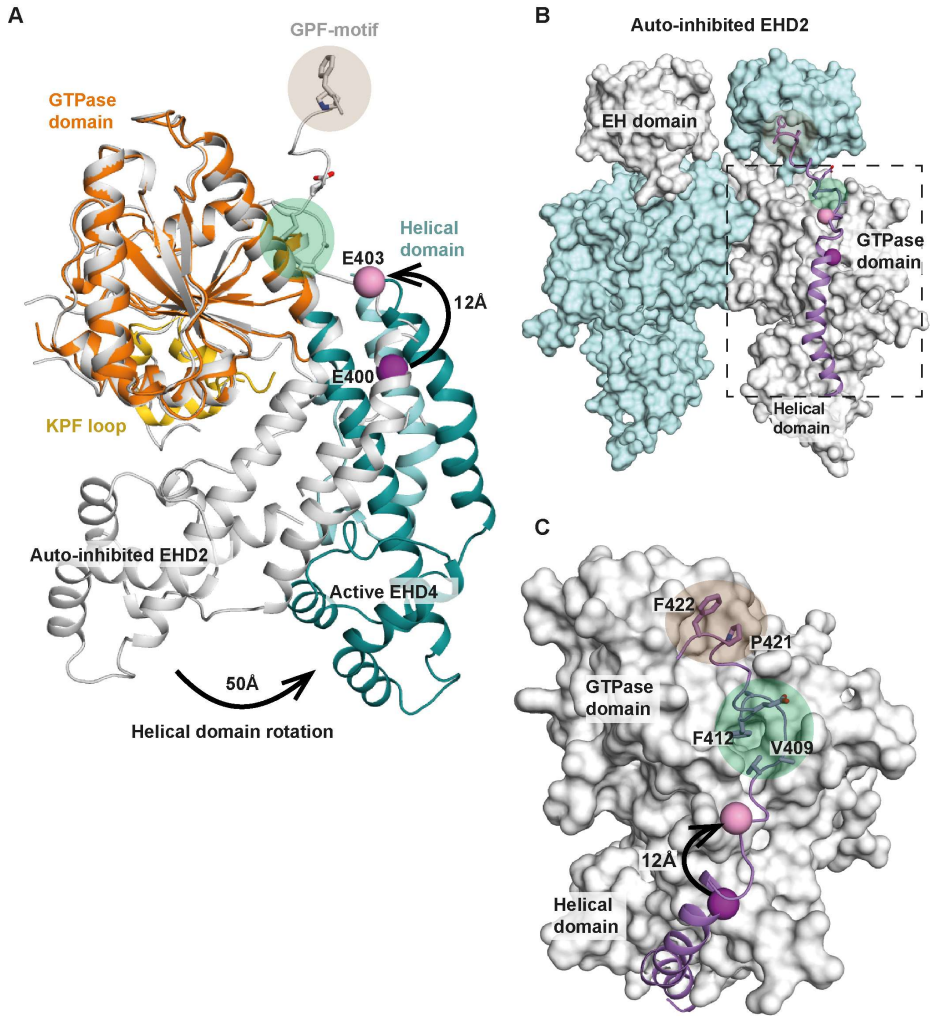


**Figure 32. Reorientation of the Helical-EH domain linker in the active conformation.** (A) The GTPase domains of EHD2 and EHD4$^{\Delta N}$ were superimposed. Highlighted is the position of Glu403 (represented as pink ball), the last resolved residue in the EHD4$^{\Delta N}$ structure, corresponding to Glu400 in EHD2 (represented as purple ball). This residue is displaced by 12 Å through the rotation of the helical domain. (B) EHD2 dimer (pdb 4CID), in which the final helix α12 and the adjacent linker is shown in purple. (C) Detailed view showing the interaction of the helical domain-EH domain linker with the GTPase domain. The displacement of Glu400/Glu403 is indicated as in A. We suggest that the rotation of the helical domain pushes the linker away from its position in the EHD2 dimer. In particular, Val409 and Phe412 will be shifted away from their hydrophobic binding pocket (marked as green circle).

Consequently, also the GPF motif (residues 420–422, marked as orange circle), which binds to the opposing EH domain, may be displaced.

The rotation also reorients the membrane binding site in α9 including Thr320, Val321, Phe322, and Lys328, which in EHD2, were shown to directly interact with the membrane (Shah et al., 2014) (Fig. 33). To understand the consequences of the rotation for membrane binding, a previously established EPR assay for EHD2 was employed as a model for the EHD family. In these experiments, a single paramagnetic spin probe is attached to a single cysteine introduced at a specific site in an otherwise cysteine-free EHD2 variant. The accessibility of the spin label towards paramagnetic spin colliders, such as oxygen and nickel ethylenediamine diacetic acid (NiEDDA), can provide information on the membrane immersion of the spinlabel (Margittai and Langen, 2006). Using this assay, it was demonstrated that not only the N-terminal part of α9 at the tip of the helical domain, but also Gln330, Leu331, and Leu333 at the C-terminal end of α9, contribute to membrane binding (Fig. 33B and C). Furthermore, it was shown that Cys356 in the adjacent helix α11 directly interacts with the membrane. In contrast, Val337 and Ala340 in α10, which is bent away from α9 and α11, did not penetrate into the membrane (Fig. 33B and C).

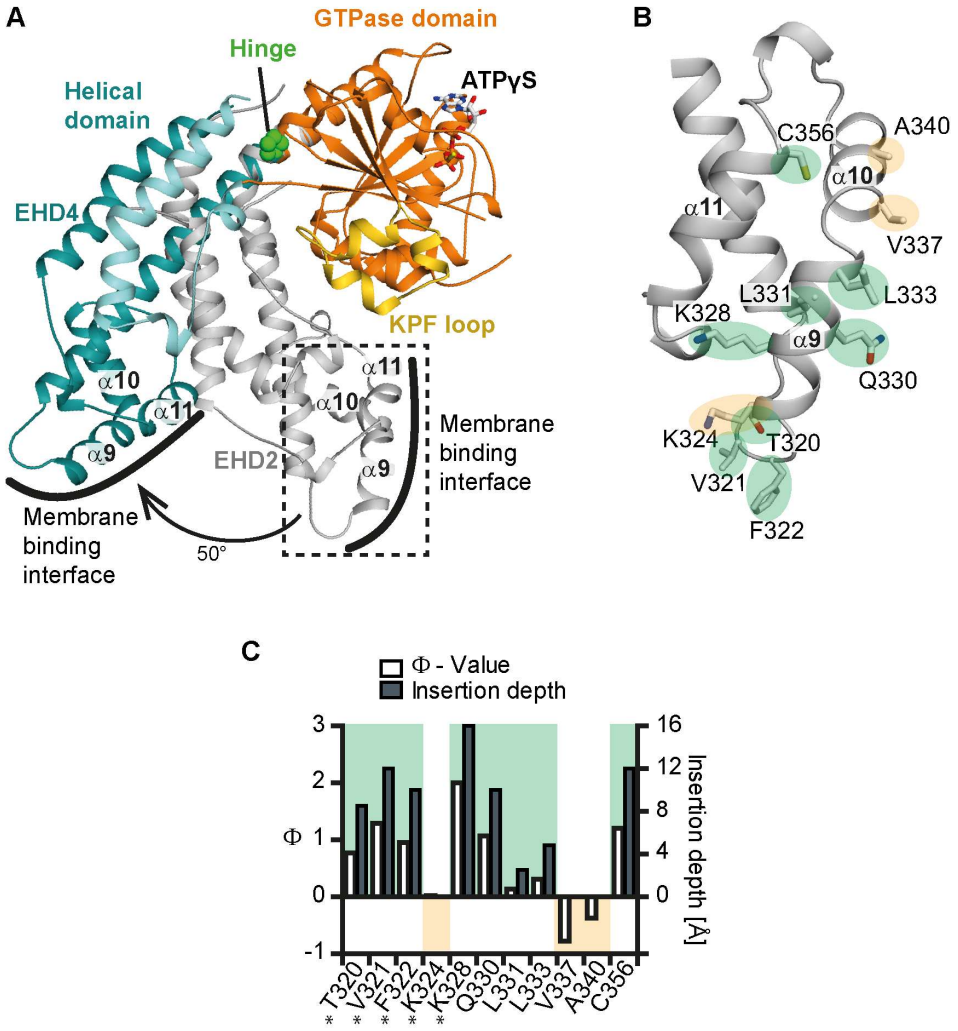


**Figure 33. The rotation of the helical domains allows membrane binding.** (A) Superposition of the GTPase domains of EHD4$^{\Delta N}$ and EHD2 as in Figure 31A. (B) Magnification of the boxed area in A showing details of the membrane binding interface of EHD2. Membrane inserting (green)/noninserting (yellow) residues are highlighted. (C) The logarithmic ratio Φ of the accessibilities of spin labels to the paramagnetic colliders $O_2$ and NiEDDA was calculated for EHD2 labeled at the indicated positions in the presence of Folch-SUVs (open bars referring to the left y axis). Results from residues 277, 320–324, and 328 (*) are from (Shah et al., 2014). Positive Φ values indicate membrane insertion based on prior calibration with spin-labeled lipids. This calibration was used to convert Φ values into membrane insertion depth of each residue (filled bars to the right y axis). According to the EPR experiments, the membrane binding site involving helices α9 and α11 is indicated as a black line in A. These experiments were conducted by our collaborators C. Shah, B. Hedge and R. Langen.

These results suggest that the membrane interaction site in EHD proteins extends along the parallel helices α9 and α11, which together with the entire helical domain, move *en bloc* during activation. In the EHD2 structure, the membrane binding sites from two opposing monomers

point away from each other (Fig. 34). In this orientation, they could not bind simultaneously towards the membrane. In contrast, in the EHD4$^{\Delta N}$ structure, the lipid binding regions reorient in a parallel fashion toward the membrane surface and could bind simultaneously towards the membrane (Fig. 34).

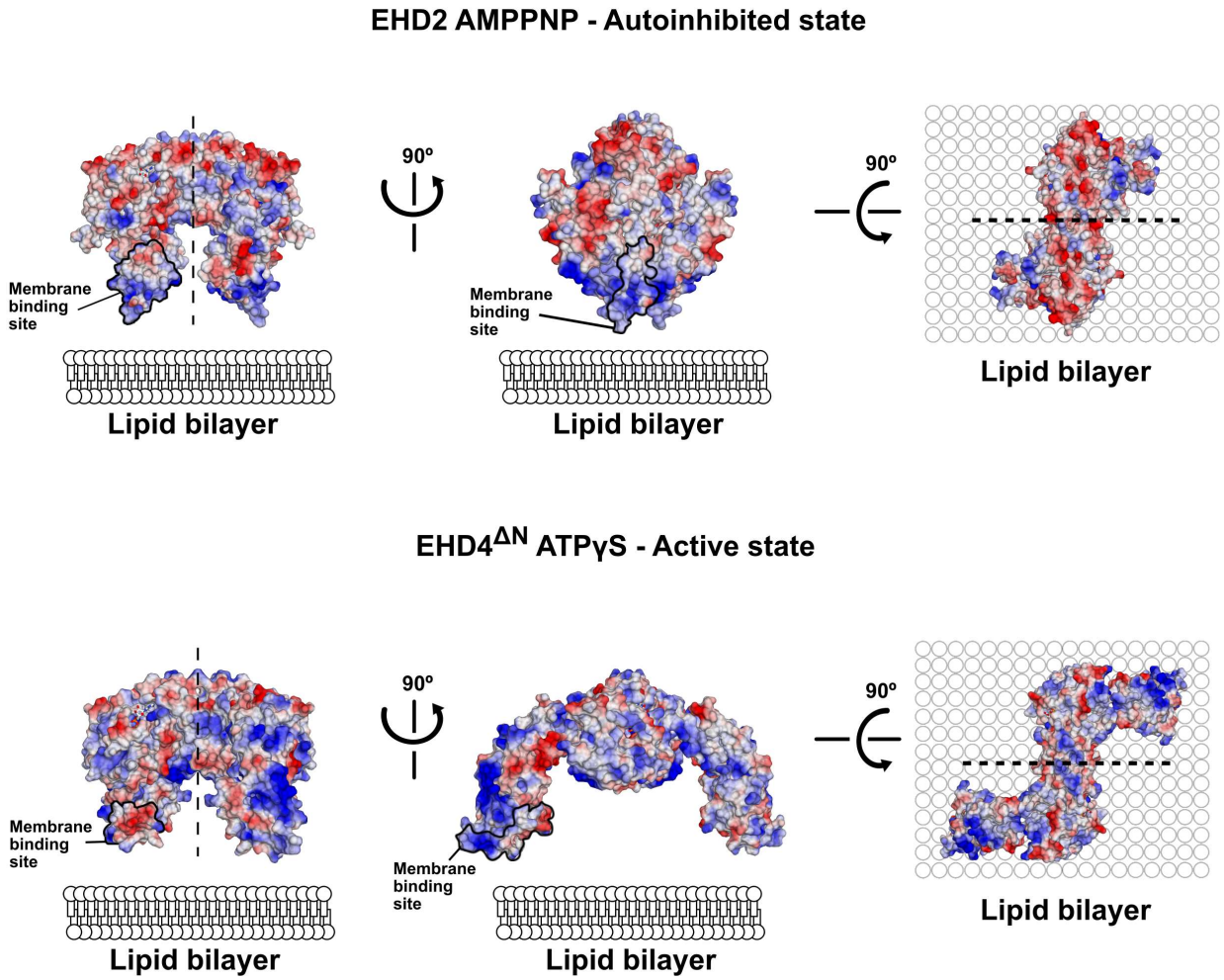


**Figure 34. The membrane binding site becomes available for membrane interaction upon rotation of the helical domain.** Electrostatic potentials (±10 kcal/mol × e, where e is the charge of an electron) were plotted on the surfaces of the EHD2 (top) and EHD4$^{\Delta N}$ (bottom) dimers, with the GTPase domains of both dimers in the same orientation. The membrane binding site of EHD2 is more positively charged compared with EHD4, possibly reflecting different lipid binding specificities These results suggest that the EHD4$^{\Delta N}$ structure represents a membrane-binding competent, active conformation.

## 4.8 The KPF loop is necessary for oligomerization

The opening of the helical domain upon activation releases interactions between the GTPase domain and the helical domain in the autoinhibited state. In the EHD2 structure, the helical domains form several salt bridges to the GTPase domain of the same monomer (Fig. 35, black box). The corresponding salt bridges are broken in the EHD4$^{\Delta N}$ structure (Fig. 35, black box). It was previously demonstrated that the N-terminal 8 amino acids in the autoinhibited EHD2 dimer folds back into a hydrophobic groove at the GTPase domain (Fig. 21) (Shah et al., 2014). In EHD4$^{\Delta N}$, the hydrophobic groove in the GTPase domain is occupied by the adjacent KPF loop, which undergoes a large-scale reorientation (Fig. 35, blue box). Residues 110-135, KPF loop, are ordered and fold into 3 α-helices, αE1-E3, towards the GTPase domain and are stabilized by many hydrophobic interactions (Fig. 35, blue box). Conserved residues in this loop, such as F125, L128 and F131, anchor the helix into this pocket, whereas in the autoinhibited EHD2 structure, the highly conserved W4 and M5 of the N terminus occupy the equivalent space (Fig. 21 and 35). These observations suggest that during the activation process, the N terminus is released and the KPF loop switches into the hydrophobic groove of the GTPase domain.

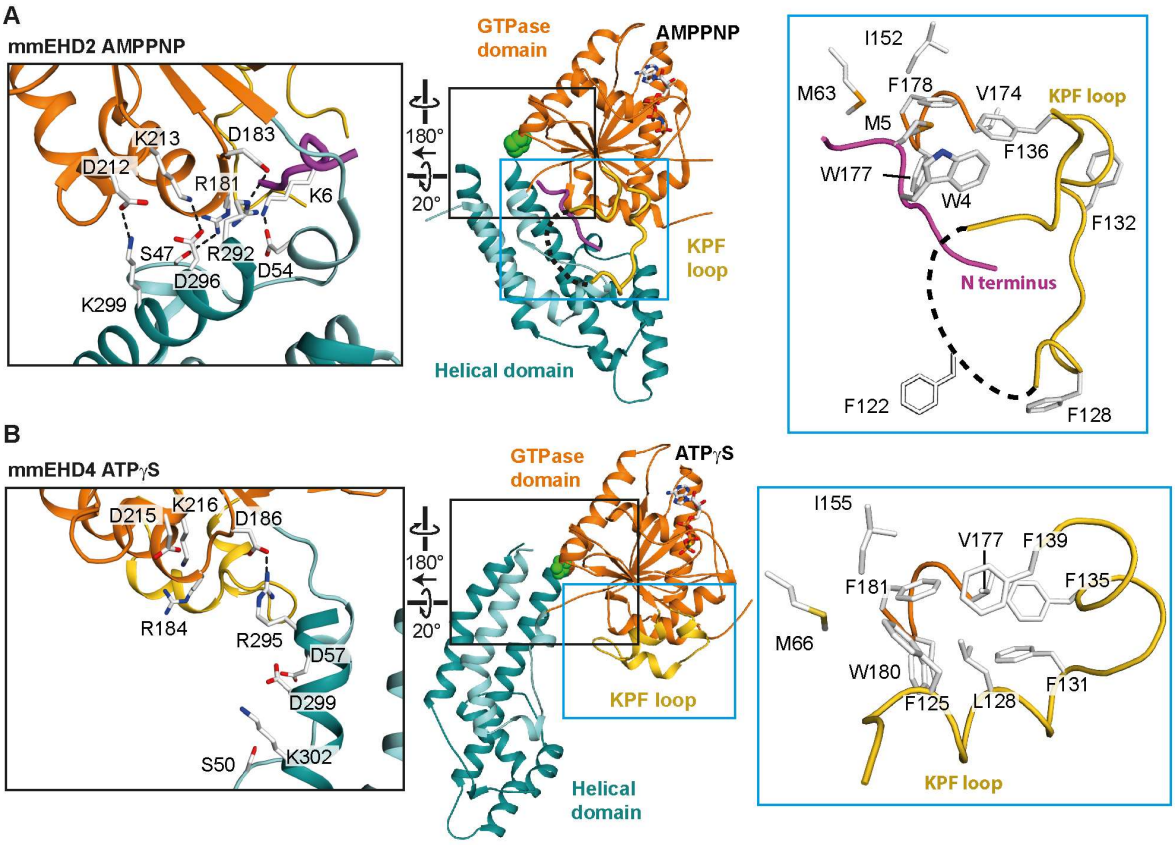


**Figure 35. The KPF loop undergoes a large-scale reorientation upon activation.** (A) Structure of EHD2 (pdb 4CID). The black box highlights the contacts of the helical domain with the GTPase domain and the N terminus in the autoinhibited state. The blue box shows the localization of the N terminus in a hydrophobic groove of the GTPase domain. (B) Structure of EHD4$^{\Delta N}$, with the same orientation of the GTPase domain as in A. The black box features the broken contacts between the helical domain and the GTPase domain in the active state. The blue box shows that the KPF loop occupies the hydrophobic groove in the GTPase domain, with Phe125, Leu128, and Phe131 (corresponding to Phe122, Leu125, and Phe128 in EHD2) acting as anchor points. Because of three extra amino acids in the N-terminal region of EHD4, the numbering of residues on EHD4 (residues 13–541) corresponds to the EHD2 residue number plus three.

## 4.9 Assembly of EHD4

The analysis of the crystal packing showed that EHD4$^{\Delta N}$ dimers assembled in a linear fashion in the crystals (Fig. 36). In these oligomers, the membrane binding sites of the helical domain were oriented in the same direction, suggesting a physiologically plausible assembly. The oligomer had the same width (90 Å) as single EHD4 filaments sometimes observed on tubulated liposomes (Fig. 26). Furthermore, the GTPase domains of adjacent EHD4$^{\Delta N}$ dimers directly opposed each other via the highly conserved G-interface, although they were separated by a

small gap (Fig. 37). Daumke and colleagues previously proposed a similar oligomerization model for EHD2, but without the rotation of the helical domains (Daumke et al., 2007). When analyzing the oligomerization determinants in these linear EHD4$^{\Delta N}$ assemblies, it was observed that the rearranged KPF loop interacted with the helical domain of the adjacent dimer via highly conserved interfaces (Fig. 38**)**.

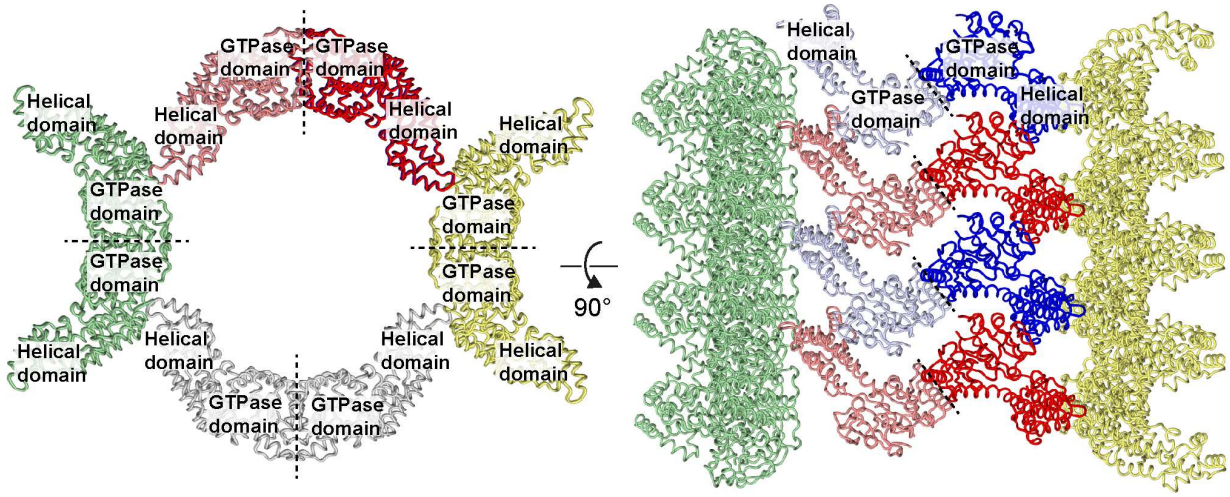


**Figure 36. Crystal packing of ATPγS-bound EHD4$^{\Delta N}$.** The crystal packing is shown in two different views. The crystals are built of four EHD4 filaments, which are rotated 90° to each other (left). Alternate dimers are colored (right) in blue and red (light/dark for the monomers).

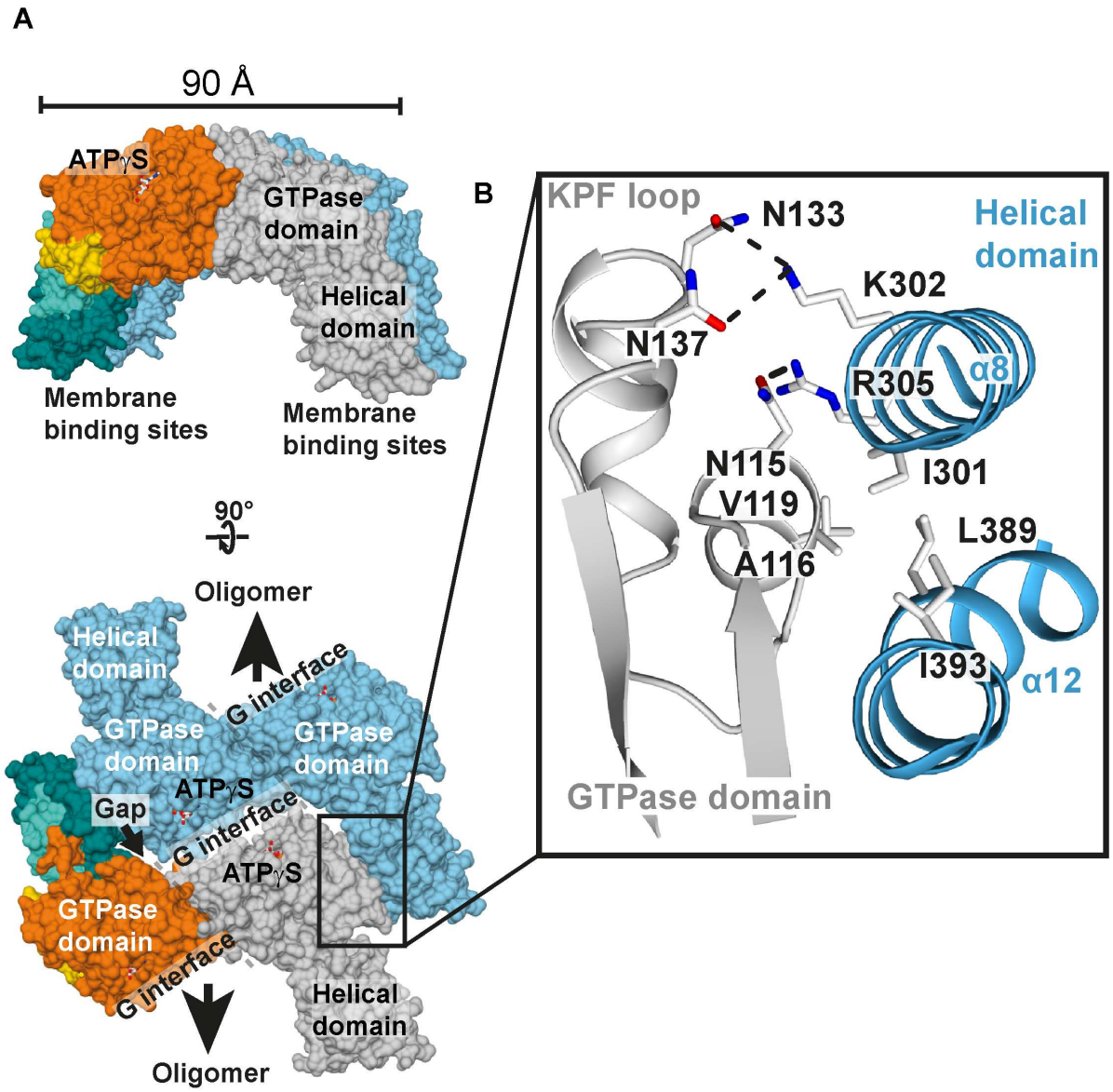


**Figure 37. Oligomerization results from a new interface between the rearranged KPF loop and the helical domain.** (A) Two views on the EHD4$^{\Delta N}$ oligomers in the crystals represented by two dimers. One dimer is colored as in Fig. 30, whereas the other is colored in light blue. Note the gap between the G-interfaces of assembling dimers. (B) Inset shows details of the oligomerization surface involving the KPF loop and the helical domain of the opposing dimer.

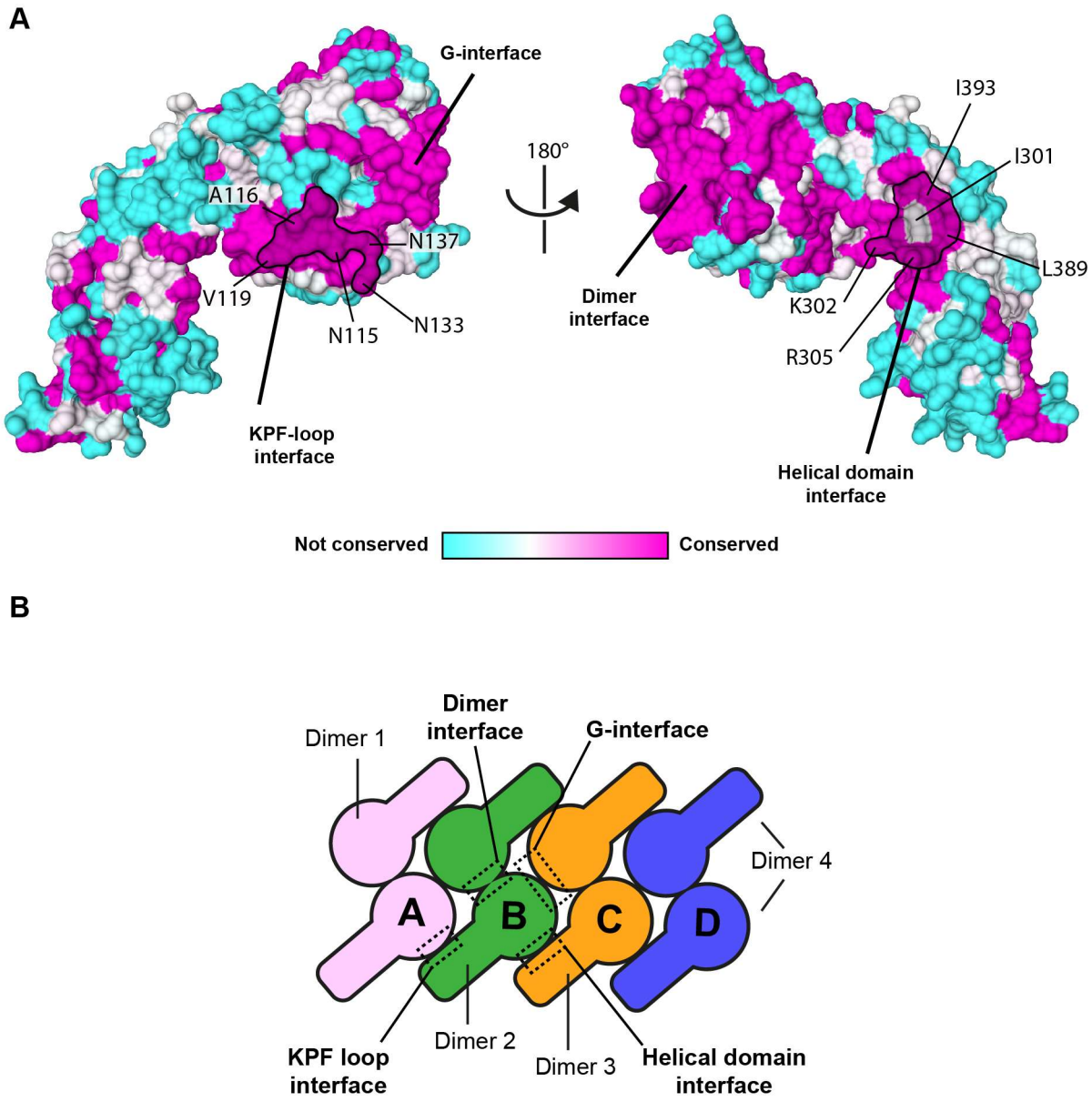


**Figure 38. Conserved interfaces in EHD proteins.** (A) Surface conservation plot of EHD4, using 39 EHD sequences from 20 different species. Conserved residues are shown in purple and nonconserved residues in cyan. Note that the oligomerization interface between the GTPase domain and helical domain is highly conserved. (B) Schematic arrangement of EHD4 dimers in the oligomer. The four conserved interfaces are depicted based on the conservation plot from A.

To probe the involvement of this new interface in oligomerization, the aim was to disrupt it by mutating several conserved residues involved in these interactions (Fig. 37). Based on the generated conservation plot, a double mutant was generated and both Lys302 and Arg305 were mutated to alanine in order to disrupt the interaction to the conserved N133 and N115, respectively (Fig. 37). The conserved residue Phe125 was also mutated to an alanine, as this mutation (F122A in EHD2) was known to affect EHD2 localization to caveolae (Moren et al., 2012). Based on the EHD4 structure, it was reasoned that the F125A mutant would prevent the large-scale reorientation the KPF loop towards the GTPase domain and consequently abolish oligomerization (Fig. 35).

Different mutants with the N-terminal deletion were overexpressed in HeLa cells and showed a severe loss of membrane recruitment (Fig. 39A and B). Similar results were also previously obtained for the F122A mutant of EHD2 (corresponding to F125A in EHD4) (Moren et al., 2012). An attempt to generate a mutant that would stabilize the oligomerization interface in the full-length EHD4 was carried by introducing the A116L and N133D mutations. These mutations were performed in order to enhance hydrophobic interactions and create an additional salt bridge to Lys302, respectively (Fig. 37). When expressed in HeLa cells, the single mutants showed similar membrane recruitment compared with EHD4 (Fig. 39A and B). Strikingly, the double mutant showed greatly enhanced membrane recruitment, consistent with an increased oligomerization activity (Fig. 39A and B ).

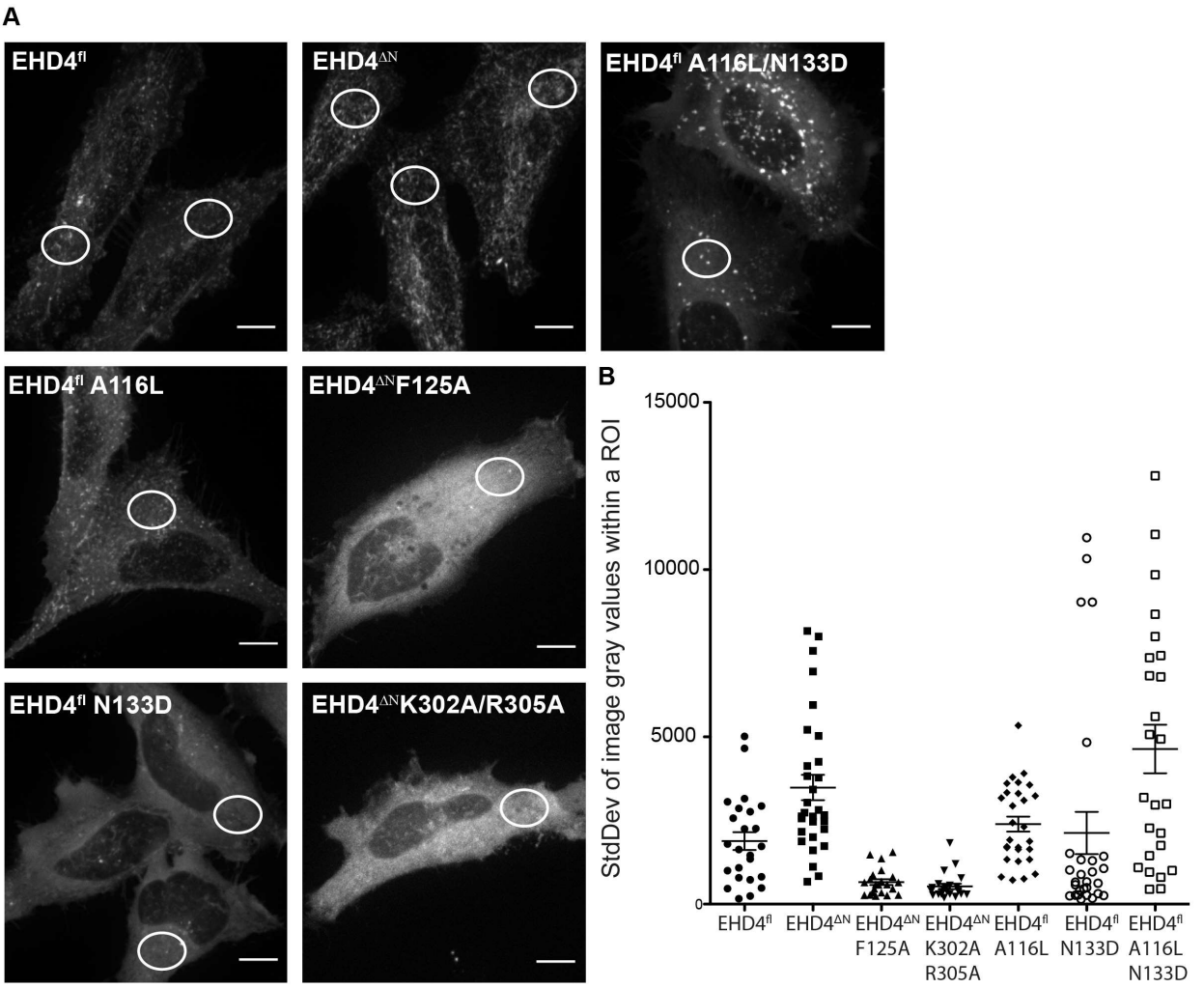


**Figure 39. Membrane recruitment of EHD4$^{\Delta N}$ mutants.** (A) Representative maximum intensity projections of live HeLa cells expressing mCherry-tagged protein as indicated. White circles illustrate typical placings of the region of interest (ROI) within the cells. (B) SD of gray values derived from one ROI per cell from at least 20 cells for each indicated construct. Error bars show SEM. Two-tailed t tests was performed on EHD4$^{\Delta N}$ to each set of data to determine significance *P ≤ 0.05, **P ≤ 0.005, ***P ≤ 0.0001. (Scale bars: 10 µm.).

An attempt to purify all mutants was carried out, but only some were soluble. The mutants F125A and K302A/R305A were purified as described in section 3.2.2. It was shown that the purified mutants could still bind to liposomes (Fig. 40A). This result show that the mutations did not affected the membrane binding site at the helical domain. In addition, the F125A completely lost its ability to remodel membranes and the K302A/R305A mutant showed reduced remodeling of membranes, indicated by the formation of less and irregular membrane tubules (Fig. 40B). Both mutants showed slightly increased basal ATPase rates, which, however, were not or only to a minor extent stimulated by the addition of liposomes (Fig. 40C).

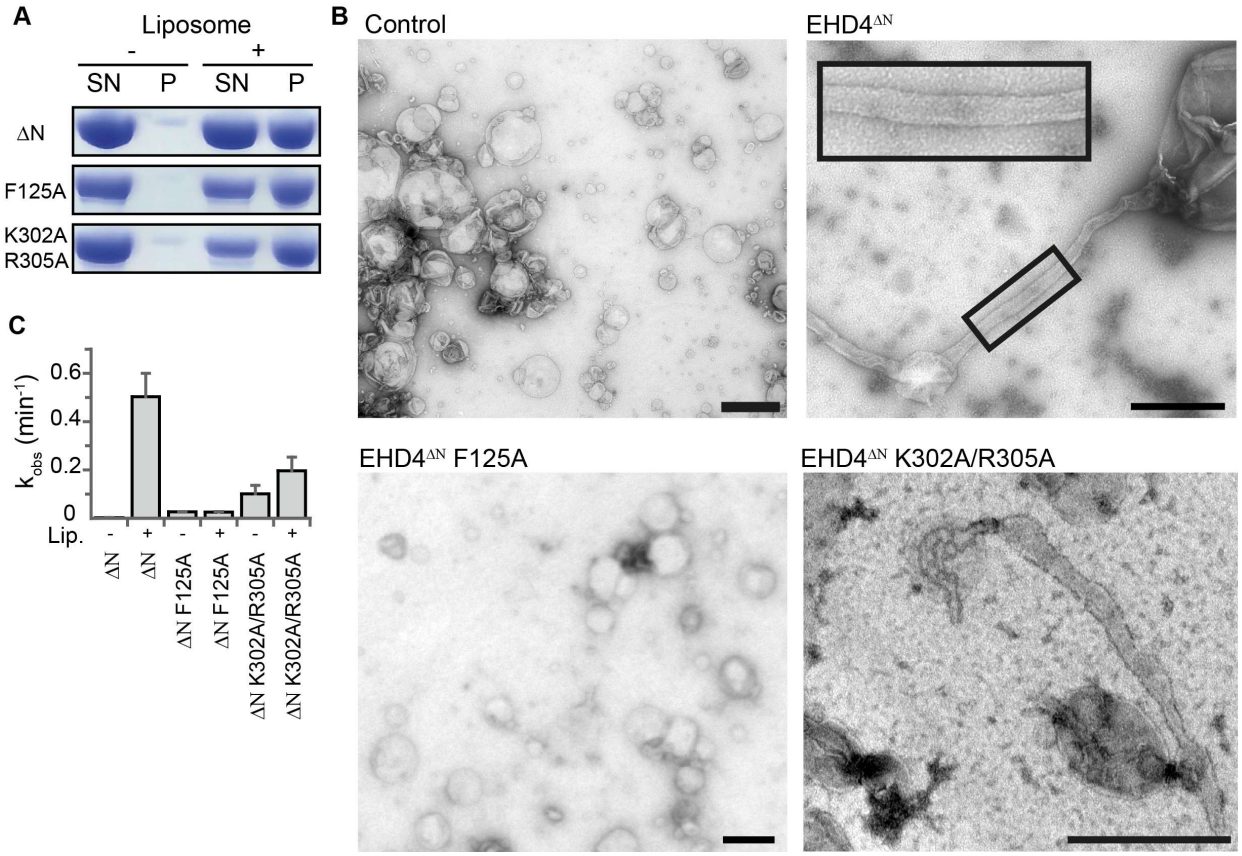


**Figure 40. Biochemical characterization of EHD4$^{\Delta N}$ mutants.** (A) Folch liposome cosedimentation assays of EHD4$^{\Delta N}$ and the indicated mutants. P, Pellet fraction; SN, supernatant. (B) Liposome tubulation experiments as in Fig. 26. (C) Basic and stimulated ATP hydrolysis reactions of EHD4$^{\Delta N}$ F125A and EHD4$^{\Delta N}$ K302A/R305A were carried out as in Fig. 25.

Taken together, these data suggest that upon membrane recruitment and release of the N terminus, the KPF loop switches into the hydrophobic groove of the GTPase domain and promotes oligomerization by interacting with the helical domain. A contact of the rearranged KPF loop with the open helical domain of the adjacent EHD dimer contributes to the regular assembly of EHDs on membranes.

## 4.10 EHD4$^{\Delta N}$ ADP-bound structure

Nucleotide hydrolysis has an important role in many proteins from the dynamin superfamily and it is critical on membrane remodeling events. It was shown for many dynamin-related proteins

that nucleotide hydrolysis drives membrane fission and fusion by inducing large conformational changes. To understand the role of the nucleotide-loading state on the helical domain movement and EH domain release, the EHD4$^{\Delta N}$ construct was crystallized in the ADP-bound state as described in section 3.2.3.1 (Fig. 41).

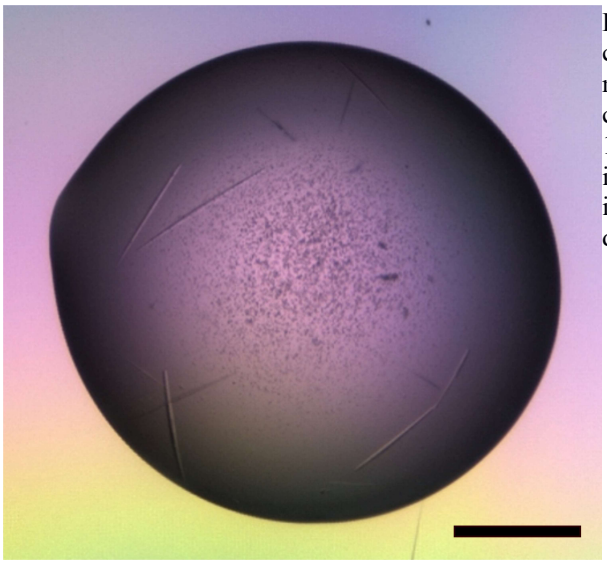

**Figure 41. Crystals of EHD4$^{\Delta N}$ bound to ADP.** Initial crystals were grown in 96 well-plate using the sitting-drop method. 200 nl of the reservoir solution containing containing 900 mM sodium malonate (pH 7) to 200 nl of the 10 mg/ml of the protein in the presence of 2mM ADP and incubated for 1 day at 20 °C. Crystals were then optimized in 24 well-plate using the hanging-drop method with 2 µl drop size. Scale bars: 200 µm.

## 4.11 Structure determination

Datasets of native EHD4$^{\Delta N}$ ADP-bound crystals were collected at the BESSY-II electron storage ring, beamline 14.1 in Berlin-Adlershof (section 3.2.3.3). Native crystals diffracted to a maximal resolution of 3.27 Å and had the same tetragonal space group as the EHD4$^{\Delta N}$ ATPγS-bound structure, $P4_22_12$, with unit cell dimensions of 199.47 X 199.47 X 41.79 Å$^3$. After an initial round of rigid body refinement, the model was rebuilt in *Coot* with alternating cycles of refinement in *Phenix* with three translation, libration and screw-rotation (TLS) parameters per molecule. Assuming one molecule in the asymmetric unit, a Matthew coefficient of 3.52 Å$^3$ /Da was calculated, indicating approximately 65 % solvent content in the crystal. Data collection statistics of native crystals are summarized in Table 3.

**Table 3. Data collection statistics of the mouse EHD4$^{\Delta N}$ bound to ADP.**

| Data collection | EHD4$^{\Delta N}$-ADP |
|---|---|
| Wavelength (Å) | 0.918409 |
| Space group | $P4_22_12$ |
| Cell dimensions | |
| *a*, *b*, *c* (Å) | 199.47, 199.47, 41.79 |
| α, β, γ (°) | 90, 90, 90 |
| Resolution (Å) | 48.4-3.27 (3.46-3.27)* |
| $R_{merge}$ (%) | 28.8 (211.5) |
| $I / \sigma I$ | 9.53 (1.02) |
| Completeness (%) | 99.5 (96.5) |
| Redundancy | 10.2 |

The structure was solved as described in section 3.2.3.4. The electron density indicated one molecule in the asymmetric unit with clear density for the GTPase domain and helical domain. The EHD4$^{\Delta N}$ structure (pdb 5MTV) was used in molecular replacement and then refined using rigid body refinement. The model was improved by several rounds of B-factor and positional refinement and manually adjusted. As observed for the EHD4$^{\Delta N}$ ATPγS-bound structure, there was no significant electron density for the EH domain. Apart from the protein molecules, 1 water, 1 magnesium ion and 1 ADP molecule were included in the final model. The model has an R-work of 20.8 % and an R-free of 25.0 % and 93.5 % of all residues are in the most favored regions of the Ramachandran plot. Refinement statistics are summarized in Table 4.

**Table 4. Refinement statistics of the mouse EHD4$^{\Delta N}$ bound to ADP**

| Refinement | EHD4$^{\Delta N}$-ADP |
|---|---|
| Resolution (Å) | 48.4-3.27 (3.4-3.27) |
| No. reflections | 13,642 (1,273) |
| $R_{work}$ / $R_{free}$ (%) | 20.8/25.0 (35.8/39.1) |
| No. atoms | |
| Protein | 3,026 |
| Ligand/ion | 28 |
| Water | 1 |
| *B*-factors (Å$^2$) | |
| Protein | 105 |
| Ligand/ion | 146 |
| Water | 87 |
| R.m.s. deviations | |
| Bond lengths (Å) | 0.003 |
| Bond angles (°) | 0.59 |

The EHD4$^{\Delta N}$ ADP-bound structure (Fig. 42) resembled the ATPγS-bound structure with an rmsd of 0.31 Å for 373 Cα atoms (Fig. 43). There are only few changes in the GTPase domain due to the different nucleotide loading state. The switch I motif was not resolved in the electron density, suggesting a flexible conformation adopted in the ADP bound state (Fig. 43).

The G2 motif of GTPases interacts with the γ-phosphate of the GTP/ATP and adopts a different conformation in the GDP/ADP-bound state. Interestingly, different conformations of the switch I define the interaction with the KPF loop. In the EHD4$^{\Delta N}$ ATPγS-state, the main chain of switch I interacts with the conserved R138 in the KPF loop. This contact is not formed in the ADP-bound state, as it adopts a flexible conformation (Fig. 43). The different conformations of switch I and KPF loop in the EHD structures suggests a possible nucleotide dependent cross-talk between these motifs which might play a role on regulating the assembly of the EHD oligomer.

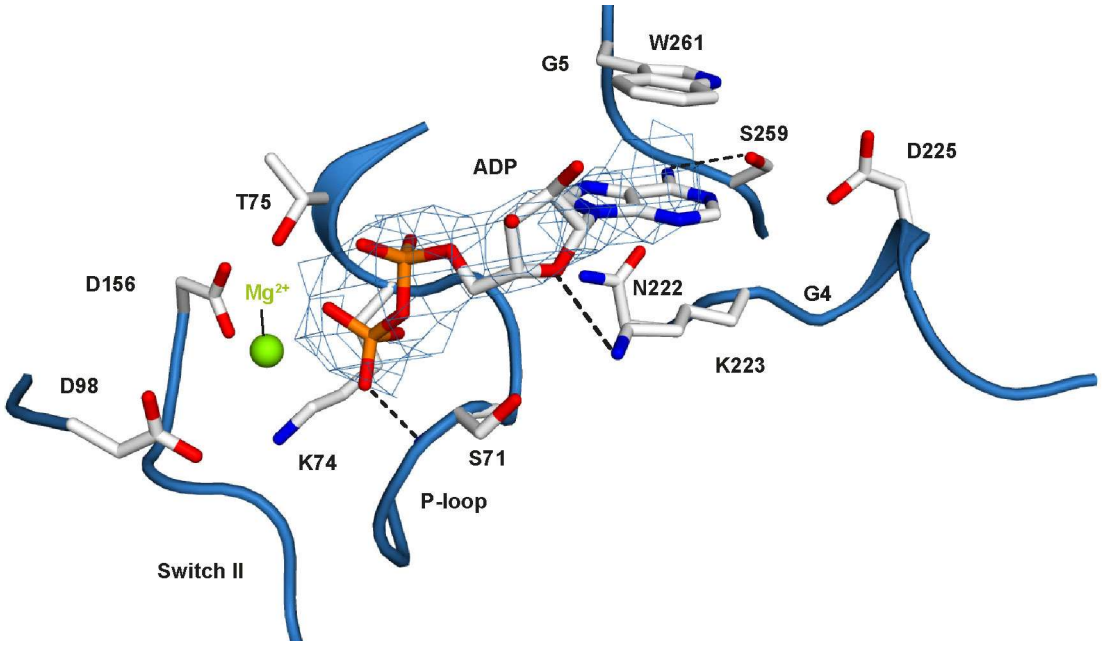


**Figure 42. Structure details of the nucleotide binding pocket complexed with ADP.** Detailed view into the catalytic site of the ADP-bound structure with selected residues from the five conserved nucleotide binding motifs (G1–G5) shown in stick representation. Hydrogen bonds are indicated by dashed lines. The final 2F o -F c density was contoured at 1 σ around the nucleotide.

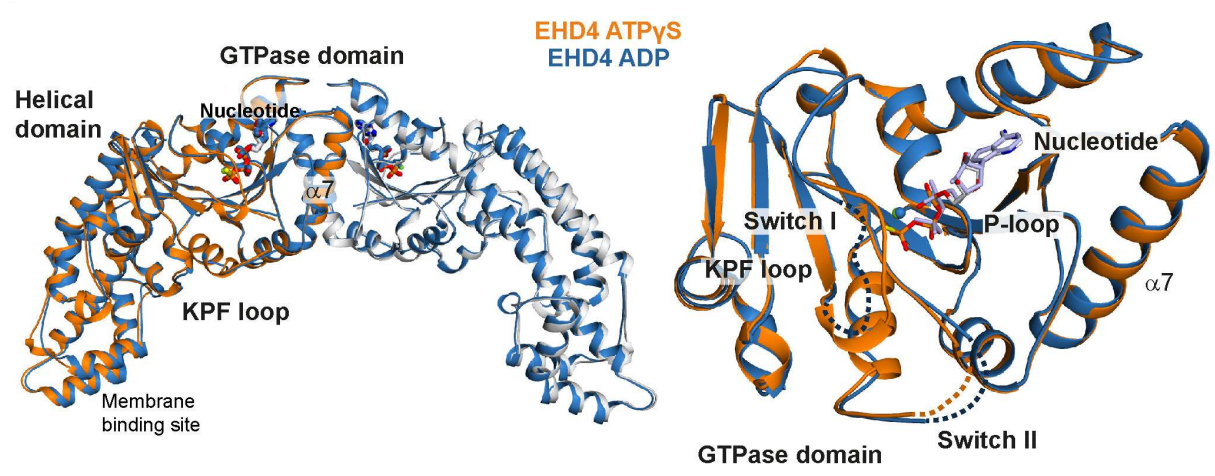


**Figure 43. Structural comparison between EHD4$^{\Delta N}$ ATPγS- and ADP-bound structures.** Crystal structure of the EHD4$^{\Delta N}$ dimer in different nucleotide states were superimposed using Coot (left). The EHD4$^{\Delta N}$ ATPγS-bound structure is colored in orange (mol A) and gray (mol B) and the EHD4$^{\Delta N}$ ADP-bound structure in blue (mol A and B). The structures showed identical fold, with the helical domains in the open conformation, KPF loop rearranged and flexible EH domains (left). A closer view of the GTPase domain monomer (right) shows a flexible switch I.

Taken together, these results showed that EHD4 has almost identical structures in two different nucleotide states, with the rotated helical domain and the EH domain displaced from its autoinhibitory site. This results support that ATP hydrolysis, in the context of the soluble EHD dimer, is not responsible for driving the major domain shifts, as described for dynamin and dynamin-related proteins. The different conformations of the switch I and its interaction with the KPF loop suggests a possible mechanism of regulation of the oligomeric assembly of EHDs.

# 5 Discussion

This work reports the active conformation of an EHD protein. Analyses of the structural data combined with structure-based functional experiments indicate how the release of autoinhibitory restraints is accomplished during membrane recruitment and remodeling. In particular, a dramatic movement of the helical domains allows membrane binding and interaction with the KPF loop for oligomerization and membrane remodeling. Ultimately, oligomerization of EHDs in the active conformation culminates in membrane remodeling, which is used in a cellular context for promoting various membrane trafficking pathways. In the following, the molecular mechanisms of membrane recruitment and activation in EHDs are discussed and compared to other dynamin superfamily members. Furthermore, by comparing the activation process to other peripheral membrane proteins, general features of activation will be elucidated.

## 5.1 Membrane binding modes in the dynamin superfamily

The recruitment of cytoplasmic proteins to cellular membranes during cell signaling and membrane trafficking is a highly regulated process (Cho and Stahelin, 2005). Membrane interaction of peripheral membrane proteins from the dynamin superfamily is critical for their cellular function (Faelber et al., 2013). Dynamin interacts with the membrane via the PH domain (Reubold et al., 2015; Srinivasan et al., 2016), MxA and DRP1 via unstructured loop regions (Anderson and Blackstone, 2013; von der Malsburg et al., 2011). Furthermore, Atlastins interact with membranes via transmembrane regions and BDLP through a hydrophobic region at the tip of their helical domains which is thought to insert as a hairpin during membrane recruitment (Byrnes et al., 2013; Low et al., 2009). To better understand the activation mechanism in EHDs, their mechanism of membrane binding is discussed in the following paragraph.

Earlier biochemical analysis indicated that EHD2 interacts with membranes through a series of hydrophobic and positively charged amino acids at helix α9 of the helical domain, which were thought to insert into the membrane and generate membrane curvature (Daumke et al., 2007). Also, mutations of lysine residues in helix α9 resulted in the loss of membrane recruitment of

EHD2 in cells (Daumke et al., 2007). Shah and colleagues used EPR measurements to identify residues in helix α9 that can insert into liposomes, thereby confirming that the membrane binding site of EHD2 involves this region (Shah et al., 2014). This study highlighted the possibility to use EPR measurements for the identification of the membrane binding region in EHDs, as previously shown for other peripheral membrane proteins (Gallop et al., 2006; Jao et al., 2010; Lai et al., 2012; Mizuno et al., 2010).

The previous results of EHD2 opened up the question whether other regions, in particular helices α10 and α11 in the helical domain, can interact with the membrane. To address this question, EPR experiments were performed by C. Shah in the group of R. Langen, using the previously established method with EHD2 as the model protein. It was shown that residues in helix α10 did not insert into liposome and therefore did not interact with the membrane. However, residue Cys356 in helix α11 deeply inserted into liposomes, thereby showing that helices α9 and α11 bind to membranes and form the membrane binding site in EHD proteins. The relevance of these findings for understanding the membrane binding mode of EHDs remained obscure until the crystal structure of EHD4 was determined (see below).

Later, Shah and colleagues studied the interaction of EHD2 N terminus' with membranes (Shah et al., 2014). This region has hydrophobic and positively charged residues which inserts into Folch liposomes. The N terminus was shown to regulate the recruitment of EHD4 and EHD2 to the membrane (Shah et al., 2014). It is still not clear if the N terminus also plays a role in lipid specificity of EHDs (Daumke et al., 2007; Simone et al., 2013), or if it can interact with proteins at or in the membrane, e.g. caveolar proteins (Moren et al., 2012). Furthermore, the deletion of the N terminus did not affect membrane binding of EHD2. In contrast, mutations in residues involved in membrane interaction in the helical domain resulted in the loss of membrane binding. Due to these results, the membrane binding sites in the helical domains was defined as the primary site whereas the N terminus comprised the secondary membrane binding site. In addition, a work published by Naslavsky and colleagues showed membrane interaction of the EHD1 EH domains with charged membranes (Naslavsky et al., 2007). Taken together, these results implicate three membrane binding sites for EHDs, with the EH domains being the tertiary binding site.

The membrane binding site of several peripheral membrane proteins confer lipid specificity and are involved in the localization to the correct membrane compartment. The PH domain of dynamin has specificity for PIP2, which is enriched at the plasma membrane and is important for the recruitment to CCVs (Kenniston and Lemmon, 2010). The B-insert of DRP1 confers specificity to cardiolipin, which is present at mitochondria and is important for the recruitment of DRP1 to the mitochondria fission site (Bustillo-Zabalbeitia et al., 2014). Daumke and colleagues showed that EHD2 binds preferentially to PIP2-containing liposomes (Daumke et al., 2007). Subsequently, it was shown that EHD2 localized at caveolae and that PIP2 was important for the recruitment of EHD2 to the plasma membrane, thereby to the caveolae (Simone et al., 2013). Several studies have shown that mammalian EHDs localize to different membrane compartments in the cell, but the underlying mechanisms have remained unclear. Furthermore, the primary membrane binding site of mammalian EHDs shares low sequence homology, which could indicate a different lipid specificity between these proteins. Taken together, it is likely that lipid specificity of the primary membrane binding site plays an important role in the localization of EHDs within cellular compartments.

## 5.2 Helical domain movement

Several crystal structures of dynamin superfamily proteins showed a variety of domain movements when bound to different nucleotides (see Appendix A). For example, GTP hydrolysis drives the movement of the BSE (Chappie and Dyda, 2013) and helical domains (Byrnes et al., 2013), which is linked to the fission and fusion of membranes (Antonny et al., 2016; Daumke and Praefcke, 2016). The underlying mechanisms of nucleotide hydrolysis driven domain rearrangements are not always completely understood. However, several structures have shown the involvement of a conserved proline residue acting as hinge for such domain movements (Chappie et al., 2011). In this thesis, the crystal structures of EHD4 revealed a large movement of the helical domain around a hinge region also involving a conserved proline. In the following paragraphs, the opening of the helical domain and its consequences to EHD proteins are discussed.

The crystal structures of EHD4$^{\Delta N}$ complexed with ATPγS and ADP showed a 50° rotation of the helical domain compared to the autoinhibited conformation (see Fig. 33 and 34). This rotation occurs around a conserved proline residue which acts as a hinge. Studies have shown that proline residues disrupt hydrogen bonding and packing of the side chains in α-helices, which dictates a kink in the structure of α-helices (Barlow and Thornton, 1988; Wilman et al., 2014). The presence of a hinge region involving a conserved proline was also described for dynamin (Chappie et al., 2010), MxA (Rennie et al., 2014), atlastin (Byrnes et al., 2013) and BDLP (Low et al., 2009), which allows large movements of helical domains and the BSE (see Figures X-Y). This shows the involvement of proline residues in α-helices of peripheral membrane proteins to allow large movements of domains in the dynamin superfamily.

The rotation of the helical domains in EHD4 aligns helices α9 and α11 from the primary membrane binding site with the membrane surface and is therefore thought to promote membrane interaction (see Fig. 33 and 34). Based on these observations, the EHD4 open conformation was defined as the active state of EHDs in this thesis, since it is able to interact with membranes. Furthermore, it was suggested that the closed EHD2 structure represents an autoinhibited conformation, since it cannot bind to membranes due to the position of the primary

membrane binding site. This proposal is in agreement with the recent published work by Hoernke and colleagues, which have described an open conformation of EHD2 helical domains bound to a flat membrane (Hoernke et al., 2017).

The opening of the helical domain appears to be a result of the release of the N terminus from the hydrophobic pocket and not of the nucleotide loading state. Thus, the EHD4 structure assumes an open conformation in both ATPγS and ADP-bound state, suggesting a link of the open conformation to the absence of the N terminus. However, it cannot be ruled out that lattice contacts in the crystal stabilize the active conformation also in the ADP-bound states. This could be analyzed, for example, by solution FRET measurements in the presence of different nucleotides, as previously done for atlastin (O'Donnell et al., 2017).

How could the N terminus regulate the conformation of the helical domain? In the autoinhibited EHD2 structure, Lys6 at the N terminus is part of an extensive network of interactions between the GTPase domain and the helical domain (see Fig. 35) which appear to stabilize the closed conformation. The release of the N terminus may weaken such interactions and favor the open conformation. In the active state, the KPF loop occupies the same hydrophobic pocket as the N terminus in the autoinhibited state. However, the KPF loop does not appear to stabilize the autoinhibited conformation but rather favor higher order oligomerization (see below). In addition, the nucleotide loading state of EHDs may contribute to the switch of the N terminus and the KPF loop in the hydrophobic pocket, and therefore influence the conformation of the helical domain (see also below). Clearly, further studies including mutagenesis data in the N terminus and KPF loop must be carried out in order to understand the series of events leading to the opening of the helical domains.

In contrast to the domain rotation observed in EHDs, the movement of the BSE of dynamin acts as a power stroke during membrane remodeling and is therefore important for dynamin-mediated membrane fission (Antonny et al., 2016; Chappie et al., 2010). For Atlastin, the movements of the helical domains as a response to hydrolysis controls the tethering and fusion of opposing ER membranes (Byrnes et al., 2013). In contrast, the movement of the helical domain of EHDs appear to regulate membrane binding.

In summary, the EHD4 crystal structure revealed insights on the membrane interaction mode of these proteins. In the autoinhibited conformation, EHD proteins are not able to interact with

membranes, in which the primary membrane binding sites are inaccessible for membrane interaction. However, in the active conformation, the helical domains align the primary membrane binding site and are able to interact with membranes.

## 5.3 Oligomerization

Oligomerization plays an important role in dynamin superfamily proteins for their cellular activity. For example, the formation of dynamin oligomers is critical for promoting membrane fission at CCVs (Faelber et al., 2013), whereas oligomerization of DRP1 and MxA is critical for mitochondrial fission (Fröhlich et al., 2013) and the antiviral activity (Gao et al., 2010). Also EHDs were shown to oligomerize around membranes in an ATP-dependent manner and to remodel membranes (Daumke et al., 2007; Shah et al., 2014). In this thesis, the mechanism of oligomerization in EHDs was described and is discussed in the following paragraphs.

Earlier, EHD2, as well as other EHDs, were shown to remodel Folch liposomes into tubules and form ring-like oligomeric structures around it (Daumke et al., 2007). Later, several studies indicated the importance of oligomerization and membrane remodeling activity for the cellular function of EHD proteins. Thus, EHD1 oligomerization around endosomal membranes was suggested to promote membrane fission (Cai et al., 2014), while EHD2 is thought to oligomerize around the caveolar neck to stabilize caveolae at the plasma membrane (Moren et al., 2012; Stoeber et al., 2012). Oligomerization of EHD3 stabilize curvature of endosomal membrane tubules (Bahl et al., 2016) and EHD4 was shown to oligomerize at micropinosomes and promote membrane fission (Shao et al., 2002).

In this thesis, the crystal packing of the EHD4$^{\Delta N}$ bound to ATPγS and ADP revealed a linear assembly of EHD4 dimers. Interestingly, the dimers were contacting each other by an interface between the KPF loop in the GTPase domain and residues in the helical domain. In the active state, the KPF loop undergoes a large-scale rearrangement, folds into the hydrophobic pocket and interacts with the opened helical domain. Mutations in the KPF loop and the helical domain compromised EHD4 oligomerization and membrane deformation.

Previously, the F122A mutation in the KPF loop in EHD2 was shown to abolish cellular membrane recruitment (Moren et al., 2012), however, the impact of this mutation to EHD2

cellular function was unclear. The EHD4 corresponding residue, Phe125, is not involved in oligomerization contacts and points towards the hydrophobic pocket, as observed in the crystal structures. This residue appear to stabilize the KPF loop at its folded conformation through a number of hydrophobic interactions with the GTPase domain (see Fig. 35). Interestingly, the F128A mutation in EHD2 does not affect localization of EHD2 to caveolae, although Phe128 (Phe131 in EHD4) also contributes to the interaction network in the hydrophobic pocket (Moren et al., 2012). These observations suggest that the Phe125 in EHD4 (Phe122 in EHD2) is critical for stabilization of the KPF loop in the hydrophobic pocket.

A model for oligomerization that involves the KPF loop was suggested by Daumke and colleagues. In their model, EHD oligomerization occurs via an interaction between the EH domain and the KPF loop of the neighboring molecule (Daumke et al., 2007). However, the data from Morén and colleagues show that the presence of the EH domain is not necessary for oligomerization (Moren et al., 2012). In this thesis, a different architecture of assembly from the previous model was revealed, therefore clarifying the role of the KPF loop in this event.

This thesis highlights another case of identifying functionally important oligomerization interfaces in the crystal lattice, in particular in the dynamin superfamily. For example, the crystal structure of the helical stalk of MxA revealed the first insights of how assembly of the dynamin stalks is achieved (Gao et al., 2010). Later, the dynamin 1 and the MxA full length structures revealed the three stalk interfaces necessary for oligomerization (Faelber et al., 2011; Gao et al., 2011) followed by the identification of oligomerization contacts in DRP1 (Fröhlich et al., 2013) and the dynamin 3 tetramer (Reubold et al., 2015).

Whereas the overall architecture of EHDs is related to dynamin, their oligomerization modes differ completely. Oligomerization of dynamin, MxA and DRP1 in helical filaments is mediated by three assembly interfaces in the helical stalk (Daumke and Praefcke, 2016). The GTPase domains contribute to assembly by mediating GTPase-dependent contacts between adjacent filaments (see Fig. 37). In this way, nucleotide binding and hydrolysis can induce the rearrangement of adjacent filaments assembled via the stalk, leading to constriction of the underlying membrane.

In contrast, EHDs use an unique interface in the GTPase domain for dimerization (Daumke et al., 2007) and use contacts between the KPF loop and the helical domains for oligomerization

(see Fig. 37). The mode of assembly of the EHD oligomers excludes the dynamin nucleotide-driven sliding model for membrane fission (Antonny et al., 2016), since nucleotide-dependent contacts are formed within and not between adjacent filaments.

In summary, the KPF loop creates an unique interface which is crucial for the formation of oligomers. The results presented in this work finally explain in details the role of the KPF loop on the oligomerization of EHDs. The unique features of the GTPase domain, the dimerization and oligomerization interfaces support a distinct mechanism for EHDs as curvature stabilizers at membranes.

## 5.4 ATP hydrolysis and the G-interface

To understand the consequences of ATP hydrolysis in the EHD family, the EHD4$^{\Delta N}$ construct was crystallized in the presence of ATPγS and ADP. Surprisinlgy, no large conformational changes were observed between the two structures. However, the switch I in the ATPγS-bound structure adopted a different conformation compared with the ADP-bound state and the EHD2 (pdb 4CID) (Fig. 44). The conserved Thr97 (Thr94 in EHD2) in switch I points away from the nucleotide in the EHD4$^{\Delta N}$ structure and adopts two different conformations in the ATP and ADP-bound states. Again in a different orientation, the threonine was shown to coordinate the $Mg^{2+}$ ion in EHD2 (Daumke et al., 2007) and, in analogy to dynamin (Chappie et al., 2010), may position a catalytic water molecule for nucleotide hydrolysis. The reorientation of switch I may be explained by a contact between the main chain of Thr96 and Arg138 from the rearranged KPF loop in the ATPγS-bound structure of EHD4$^{\Delta N}$. In the ADP-bound structure, switch I is disordered and is no longer in contact with Arg138. In addition, the Thr96-Arg138 contact may regulate hydrolysis within the EHD oligomer, since the interaction of Thr97 with Arg138 occurs only in the active-oligomerized-ATPγS-bound state, suggesting a nucleotide-dependent cross-talk between the KPF loop and the switch I. In this scenario, Thr97 may act as a sensor that couples the nucleotide loading state of EHD with a specific conformation of the KPF loop.

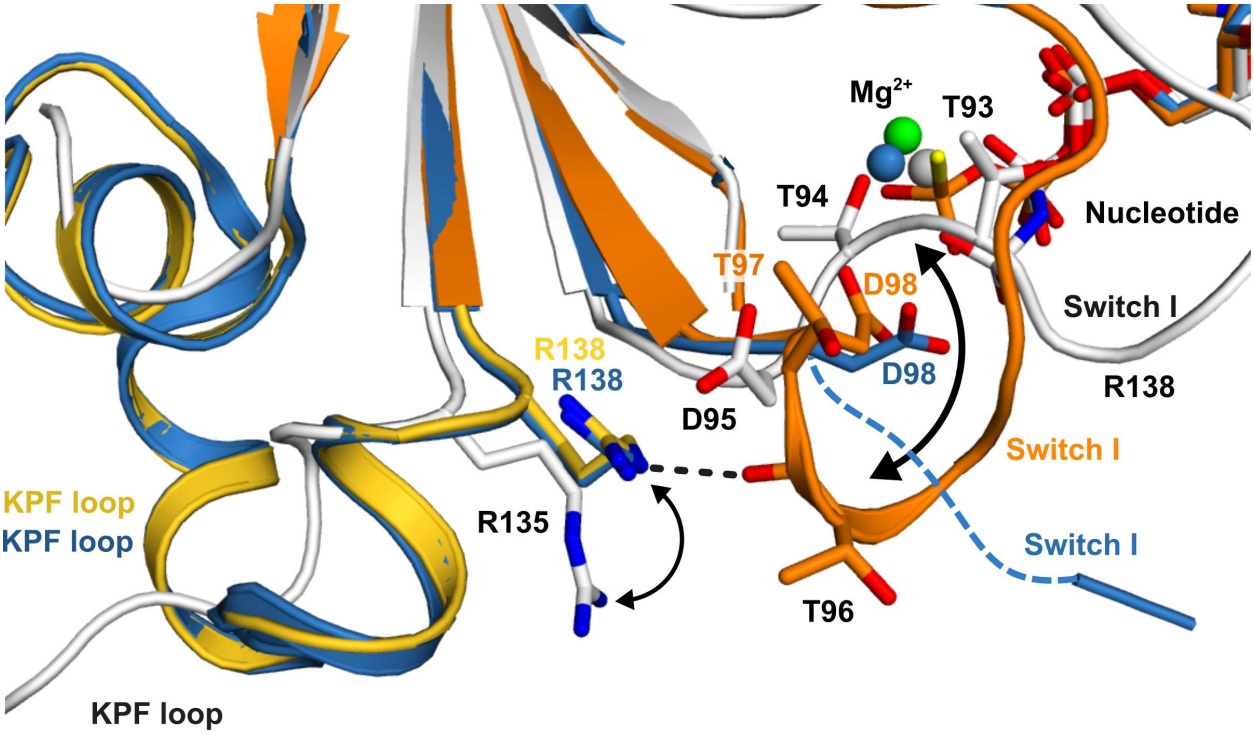


**Figure 44. Structural details of the Switch I – KPF loop cross-talk.** Superposition of the GTPase domains of AMPPNP-bound EHD2, ATPγS-bound and ADP-bound EHD4$^{\Delta N}$. In the EHD4 ATPγS-bound (colored), the KPF loop (gold) folds back into a hydrophobic pocket of the GTPase domain. Inset shows the interaction of the R138 with the backbone of the switch I in EHD4 ATPγS-bound, which is not present in EHD2 (white) nor in EHD4 ADP-bound (blue). Note in particular that the highly conserved catalytic threonine residue (T94 in EHD2; T97 in EHD4) points away from the nucleotide in EHD4$^{\Delta N}$ .

An important feature of the linear EHD4 oligomer is the position of the G–interfaces. Within the linear oligomer, the GTPase domains did not form dimers via this interface, despite being in close proximity. The G–interfaces of EHD4 dimers face each other and is possible that the GTPase domains cannot dimerize in the ATP- and ADP-bound state, but only in the transition state of nucleotide hydrolysis, as observed for dynamin and MxA (Chappie et al., 2010; Rennie et al., 2014).

With the methods used in this thesis, it was not possible to fully comprehend the mechanochemical function of nucleotide hydrolysis in EHD proteins. The challenging study of membrane bound EHD structures and of EHD proteins in complex with ADP.AlF$_4$ could bring insights into the detailed mechanism of ATP hydrolysis.

## 5.5 Autoinhibition

Earlier, Daumke and colleagues suggested that the EH domain could act as an autoinhibitory domain by sterically blocking the oligomerization through the G-interface and preventing nucleotide-stimulated hydrolysis (Daumke et al., 2007). The position of the EH domain in the EHD2 structure was described to be at the autoinhibitory site. Furthermore, in this thesis it was shown that oligomerization does not occur via the G-interfaces and that the disordered nature of the EH domain in the EHD4 structures suggests indeed an autoinhibitory activity of such domain, since oligomerization occur only in the absence of the EH domain from its autoinhibitory site.

In the EHD4 structures, the EH domain appeared flexible and no electron density was found for it, although the domain was present in the crystallized construct. The structures suggest that the opening of the helical domains dislodges the linker between the helical domain and EH domain. This linker appears to stabilize the EH domain on top of the GTPase domain in the autoinhibited structure and its release therefore favors the displacement of the EH domain (see Fig. 32). Furthermore, the displacement of the EH domain from its autoinhibitory site may also be promoted by interaction with NPF-containing proteins at the cellular target site (Giridharan et al., 2013; Guilherme et al., 2004; Moren et al., 2012). Further studies must be carried out in order to bring insights into the order of events preceding the displacement of the EH domain.

Later, Shah and colleagues showed the autoinhibitory role of the N terminus in EHD2 (Shah et al., 2014). Moreover, the position of the N-terminal residues was assigned by X-ray crystallography and EPR measurements (Shah et al., 2014). The first 8 residues of the conserved N terminus were shown to localize in the hydrophobic pocket formed between the GTPase domain and the disordered KPF loop in EHD2 (see Fig. 21). Interestingly, it was shown that the N terminus could insert into membranes, a feature that could be simulated with its deletion. Removal of the N terminus in EHD2 was shown to increase its recruitment to caveolae (Shah et al., 2014). Furthermore, the results in this thesis showed that the absence of the N terminus favors the opening of the helical domain, membrane binding and oligomerization, thereby showing the autoinhibitory role of this region in EHDs.

Recently, a study was published showing EHD2 to be highly activated in the absence of both the N terminus and EH domain, which also promoted the elongation of the caveolae neck (Fig. 45) (Hoernke et al., 2017). These studies suggest a cooperative regulatory mechanism between the N terminus and the EH domain.

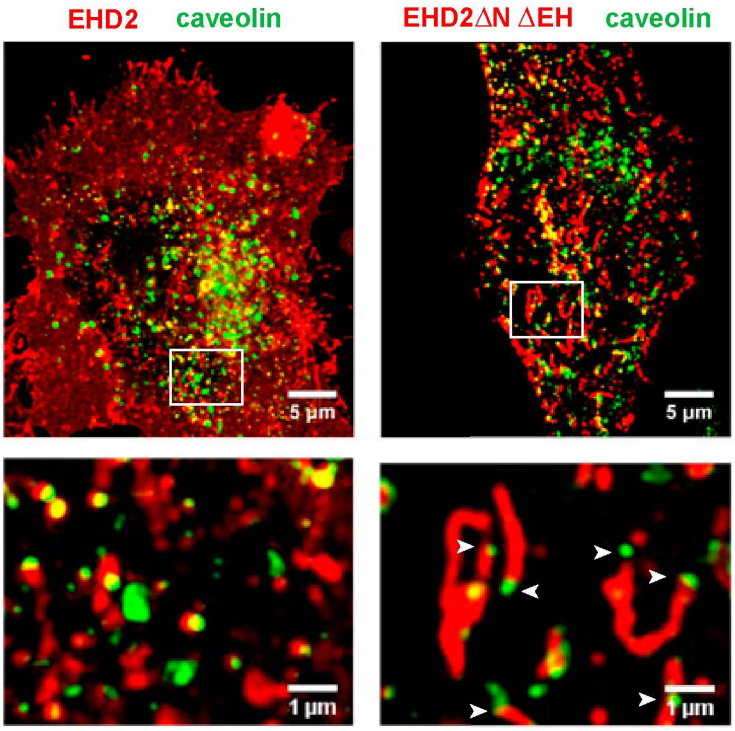


**Figure 45. Active EHD2 promotes elongation of the caveolae neck.** Representative images of caveolin 1-GFP and EHD2-mCherry or EHD2$^{\Delta N\Delta EH}$ expressing cells. Pictures below show magnifications of the indicated areas. EHD2$^{\Delta N\Delta EH}$ mutant localized at tubular elongated structures with caveolin1-GFP associated at the tips of the tubules (white arrows) (Hoernke et al., 2017).

Taken together, these results reveal specific features of autoinhibition in EHD proteins. The EH domain seems to play a role on regulation of oligomerization, in a similar way to the PH domain in dynamins, which blocks the further assembly of tetramers in the absence of membranes (Hoernke et al., 2017; Reubold et al., 2015). Also, the EH domain interacts with NPF-containing proteins, such as EHBP1 (Guilherme et al., 2004), PACSIN2 (Giridharan et al., 2013; Moren et al., 2012; Senju et al., 2015), but it was also shown to interact with the caveolar coat protein, cavin 1 (Moren et al., 2012). These interactions could have an important role in regulating the assembly of EHDs at the membrane, since in its absence, EHD2 behavior resembles the dynamin 3 ΔPH construct (Reubold et al., 2015). The interaction with EHBP1, MICAL-L1 and PACSIN2 could act as a regulator of the EHD activity, similarly to the observed interaction of DRP1 to MFF or MiD49/MiD51 (Osellame et al., 2016). Interaction to NPF-

containing proteins and/or cavin 1, appear to control the elongation of the caveolae neck, which suggests a role of the EH domain, when bound to an interaction partner, on the regulation of EHD assembly (Faelber et al., 2011; Reubold et al., 2015; Srinivasan et al., 2016).

In summary, a cooperative regulatory mechanism for the N terminus and the EH domain is suggested. The ability of those domains to interact with the membranes (Naslavsky et al., 2007; Shah et al., 2014), with other proteins (Paoluzi et al., 1998; Salcini et al., 1997) and to undergo large movements between the autoinhibited and active states show the complex level of regulation of this family of proteins. Further research is necessary to identify the sequence of events and how these domains are regulated in solution and at membranes by their interaction partners.

## 5.6 Activation model

In this section, a model of activation for EHDs based on previous results and results from this thesis is developed.

Based on the previous comparisons, the position of the N terminus, the EH domain and the orientation of the helical domains determine the activation of EHDs. In the autoinhibited cytosolic form, the N terminus is locked in the hydrophobic pocket in the GTPase domain, the helical domains are in the closed conformation with the membrane binding sites pointing away from the membrane. The KPF loop is disordered and flexible and the EH domains are located at their autoinhibitory site. Upon membrane recruitment, a series of conformational changes is triggered:

(**1**) The N terminus of EHDs is released from the GTPase domain and switches into the membrane. This switch activates EHDs, since EHD4 and EHD2 gets activated when the N terminus is removed from the protein (Fig. 22) (Shah et al., 2014).

(**2**) The helical domains rotate around the conserved Pro289. The domain rotation regulates membrane binding by adjusting the position of the primary membrane-binding site towards the membrane.

(**3**) Concomitant with the rotation of the helical domain, the linker to the EH domain is pushed from the GTPase domain. Consequently, the EH domains are displaced from their autoinhibitory

site on the GTPase domain (Fig. 32), as observed in the EHD4$^{\Delta N}$ structure. In cells, this release may be further promoted by interactions of the EH domain with NPF motif-containing binding partners, such as PACSINs, EHBP1 and MICAL-L1.

(**4**) The structural analysis shows that the KPF loop moves into the hydrophobic pocket at the GTPase domain. This rearrangement creates a conserved assembly interface with the open helical domain of the adjacent EHD dimer, therefore stabilizing the active conformation and promoting oligomerization of EHDs at the membrane.

(**5**) In addition, the nucleotide-loading state of EHDs may affect the activation by nucleotide-dependent stabilization of the N-terminal loop or the KPF loop in the GTPase domain. Supporting this hypothesis, the KPF loop and switch I interact in an ATP-dependent manner. Furthermore, the removal of the EH domain tail from the active site may allow the ATP-dependent oligomerization of EHDs in ring-like structures via the conserved G-interface, which could explain the strict ATP dependency of assembly (Shah et al., 2014). Such assembly would facilitate (**6**) a direct coupling of EHD oligomerization with the creation and stabilization of membrane curvature.

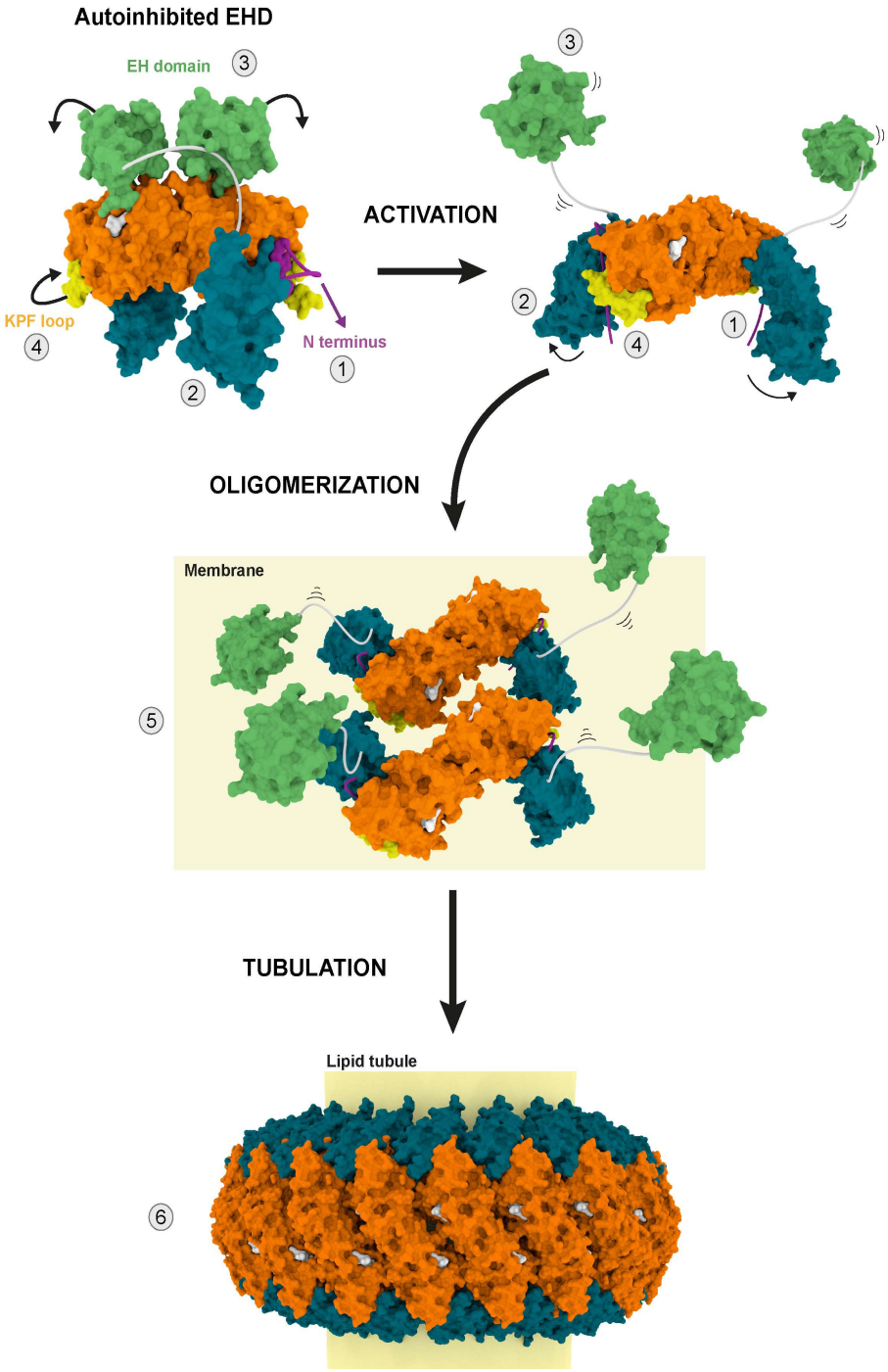


**Figure 46. Activation model of EHD proteins.** For details see section *5.6*. The numbers refer to release of the N terminus into the membrane (1), rotation of the helical domain (2), release of the EH domains from the autoinhibitory site (3), insertion of the KPF-loop into the hydrophobic pocket of the GTPase domain (4), membrane binding and oligomerization (5), and membrane tubulation (6).

## 5.7 Comparison with other peripheral membrane proteins reveals general activation features

Autoinhibition is a potent regulatory mechanism that provides tight “on-site” repression (Pufall and Graves, 2002). Activation of DNA-protein or protein-protein interactions is the most frequently observed class of autoinhibitory regulation (Trudeau et al., 2013). To date, little is known about autoinhibition on protein-membrane interactions with only a few structures of autoinhibited and active peripheral membrane proteins (McCullough et al., 2015; Misura et al., 2000; Pufall and Graves, 2002). In this section, the autoinhibitory mechanism of EHDs and other peripheral membrane proteins are compared.

### 5.7.1 Syntaxin-1A

The SNARE subunit Syntaxin-1A forms a closed autoinhibited four helix-bundle conformation and an open three helix-bundle conformation. Binding of the regulatory Munc18a/ Sec1-subunit stabilizes the autoinhibited conformation of syntaxin1A. In the open state, the released H3 helix associates with other SNARE partners to form the assembled SNARE complex (Misura et al., 2000). (Fig. 47).

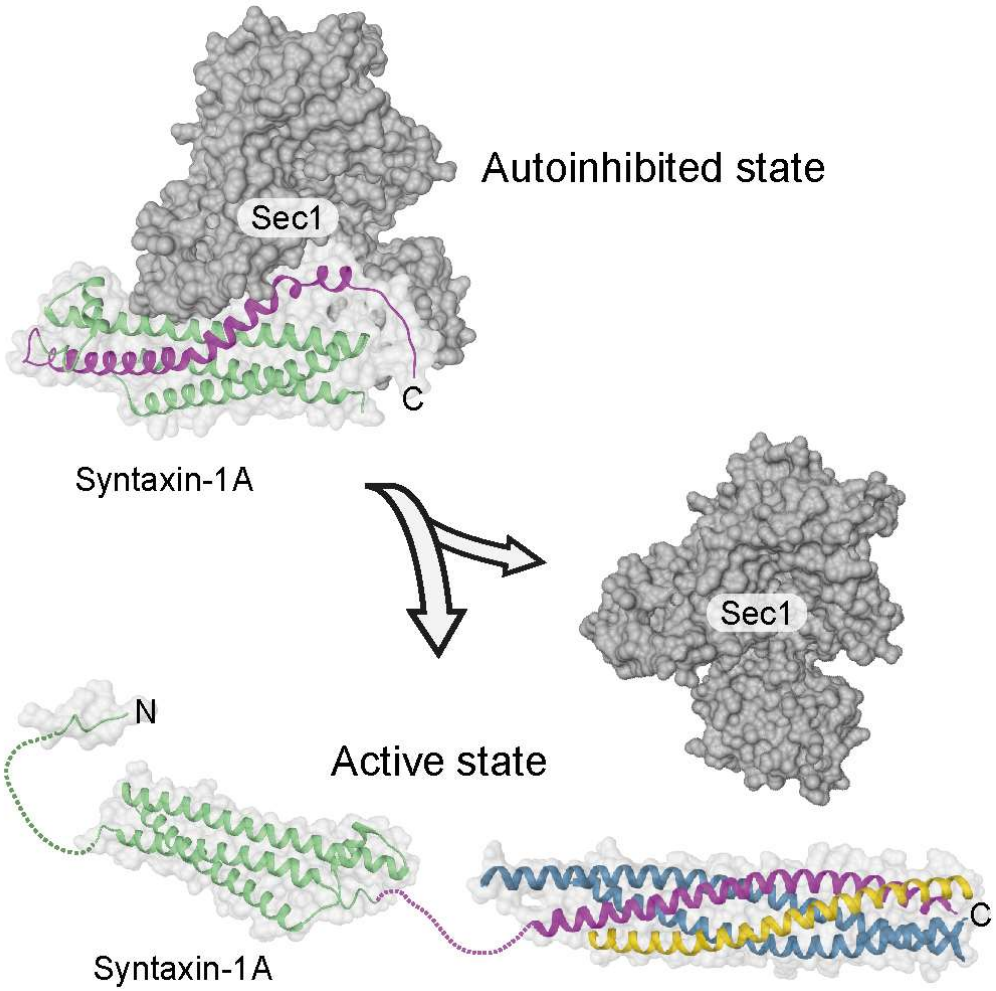


**Figure 47. Activation mechanism of the SNARE subunit Syntaxin-1A.** Model based on the structures of the autoinhibited structure of the Syntaxin-1A (pdb 3C98) and the open conformation (pdb 1S94).

Despite bearing some minor similarities, the differences between the activation mechanisms of EHDs and Syntaxin-1A are pronounced. The activation of the Syntaxin-1A consists on the SNARE complex formation, which overcomes autoinhibition by a conformational change in the Syntaxin-1A H3 and a switch from intramolecular to intermolecular interactions (Misura et al., 2000). In contrast, EHD activation consists membrane binding and oligomerization. To overcome autoinhibition it releases a set of inhibitory regions, N terminus and EH domain, and undergoes large conformational changes, helical domain and KPF loop. In a similar way to Syntaxin-1A, the N terminus and the EH domain of EHD proteins also switch from intramolecular to intermolecular interactions upon activation.

### 5.7.2 ESCRT-III

Activation of the ESCRT III-component CHMP1B promotes membrane binding and oligomerization (Fig. 48). The domain opening in the active state exposes oligomerization interfaces in CHMP1B and allows assembly of a heteromeric scaffold. The open CHMP1B conformation is then stabilized by a set of interactions along the oligomer. Each CHMP1B molecule interacts with four other CHMP1B subunits that pack together, binds to the membrane and are able to remodel it (McCullough et al., 2015).

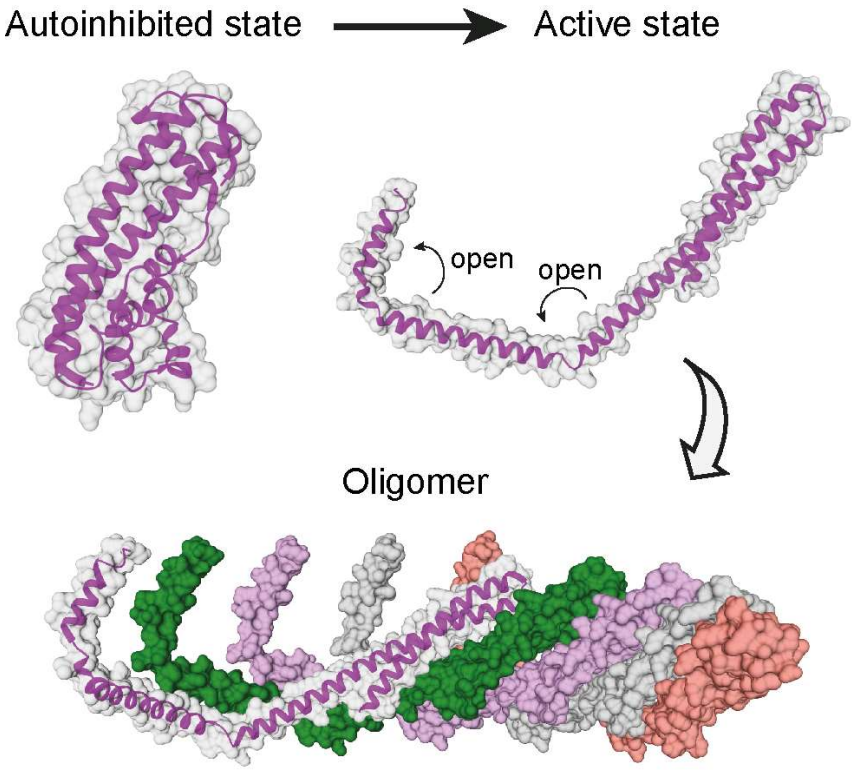


**Figure 48. Activation mechanism of the ESCRT-III component CHMP1B.** Modeled based on the crystal structure of CHMP1B in the closed state (pdb 3GGY) and the electron microscopy reconstruction of the IST1-CHMP1B in the open state (pdb 3JC1).

The activation mechanism of CHMP1B is mechanistically strikingly similar to EHD proteins. It features the coupling of membrane binding and oligomerization, which is then able to remodel membranes. Furthermore, in both systems, autoinhibition is overcome with a large conformational changes of regulatory helices, which switches from intramolecular to intermolecular interactions to form a scaffold at the membrane (McCullough et al., 2015). Thus, a parallel can be made between the helical domain of EHD proteins and CHMP1B, in which their re-localization upon activation promotes membrane interaction and oligomerization.

### 5.7.3 WASP

Activation of the WASP protein is promoted by protein-protein interaction and membrane binding. In the autoinhibited state, the CRIB domain tightly interacts with the VCA peptide (Fig. 49). The small GTPase Cdc42 binds to the CRIB domain, therefore releasing the VCA peptide to induce actin polymerization. Domain opening is further promoted by PIP2 binding (Kim et al., 2000) .

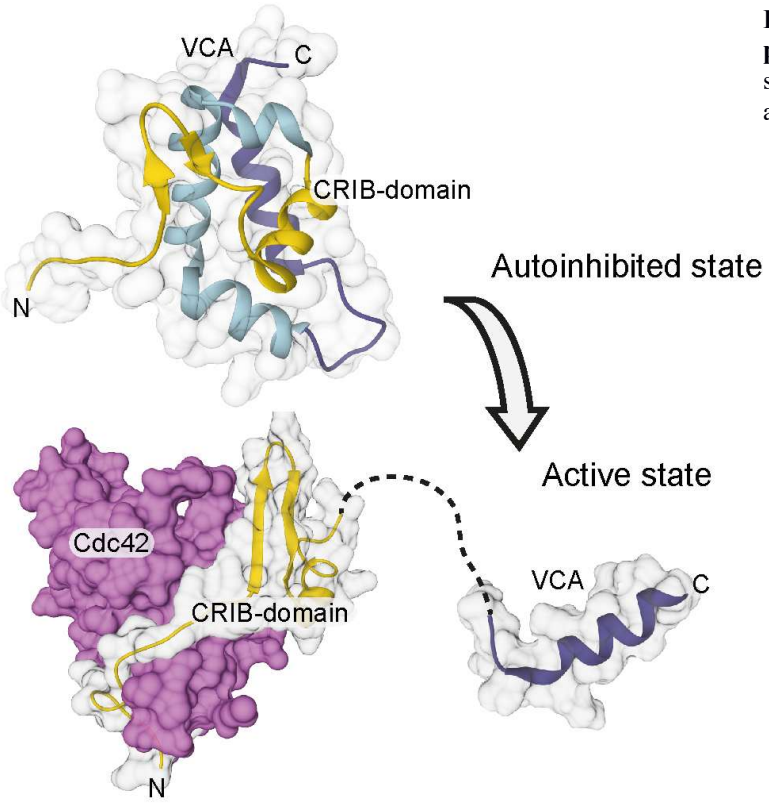


**Figure 49. Activation of the WASP protein.** Modeled based on the crystal structures of the autoinhibited (pdb 1EJ5) and active conformation (pdb 1CEE).

There are apparent differences between the activation mechanisms of EHDs and WASP proteins. The activation of the WASP follows complex formation with Cdc42 and induction of actin polymerization. It overcomes autoinhibition by releasing intramolecular interactions between the CRIB-domain and the VCA peptide and forming intermolecular interactions between the CRIB-domain and Cdc42, as well as the VCA peptide with actin. In contrast, EHD proteins overcomes autoinhibition due to the presence of membranes, without the primary need of interactions partners. The VCA peptide is comparable to the N terminus of EHD proteins, where it switches from inhibitory interactions to ligand interactions.

### 5.7.4 Syndapin/PACSIN1

The activation of the BAR domain-containing protein Syndapin/PACSIN1 involves the release of the autoinhibitory SH3 domain for membrane interaction. The crystal structure of the autoinhibited Syndapin/PACSIN-1 dimer comprising BAR and SH3 domains shows only one the autoinhibitory interface of the SH3 domain. Upon binding to proline-rich sequences of target proteins such as dynamin, the SH3 domains are released, therefore exposing the membrane binding site in the BAR domain to allow formation of a membrane-associated BAR domain scaffold (Fig. 50) (Rao et al., 2010; Wang et al., 2009).

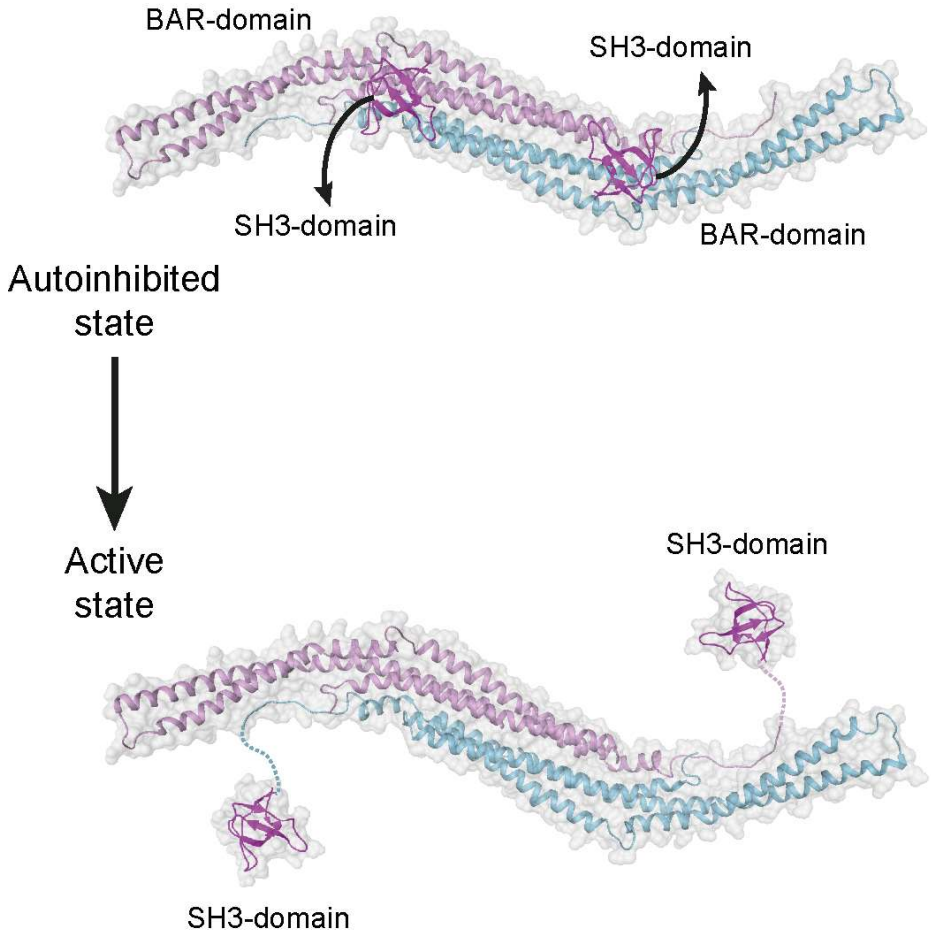


**Figure 50. Activation of the BAR domain-containing protein Syndapin/PACSIN-1.** Modeled based on the crystal structure of the autoinhibited (pdb 2X3W) Syndapin/PACSIN-1.

In similar way to EHDs, Syndapin/PACSIN1 activation features membrane binding and oligomerization. However, its activation comprises the simple release of the SH3 domain from its autoinhibitory site. This overcomes autoinhibition by interaction with PRD-containing proteins, e.g. dynamin, which is sufficient to dislodge the domain from blocking the membrane binding site (Rao et al., 2010; Wang et al., 2009). In addition, it also appears that the SH3 domain interferes with oligomerization, thereby acting similarly to the EH domain of EHD proteins.

In conclusion, comparison of autoinhibition and activation with peripheral membrane proteins show the complexity of events upon activation in EHD proteins. Regulation of membrane

binding and remodeling by the nucleotide-loading state, large domain movements and complex domain rearrangements have only been described for EHD proteins. These comparisons show the level of complexity of the activation mechanism in EHDs and highlight the challenge on working with membrane remodeling proteins.

*

In summary, this study describes a complex activation mechanism of EHD proteins. It involves several common and specific domain rearrangements and reveals new insights into how autoinhibition and activation regulates recruitment of peripheral membrane proteins to cellular membranes.

## Summary

Eps15 (epidermal growth factor receptor pathway substrate 15)-homology domain containing proteins (EHDs) comprise a family of dynamin-related mechano-chemical ATPases involved in cellular membrane trafficking. EHD proteins consist of a dynamin-related GTPase domain, a helical domain and a C-terminal Eps15-homology (EH) domain,. Previous studies have revealed the structure of the EHD2 dimer. Furthermore, the N terminal region of EHD2 was demonstrated to bind to a hydrophobic groove of the GTPase domain and to switch into the membrane in the presence of liposome, suggesting an autoinhibitory role However, the molecular mechanisms of membrane binding, oligomerization and nucleotide hydrolysis have remained obscure.

To understand the mechanism of membrane recruitment, the crystal structure of an amino-terminally truncated EHD4 dimer in complex with ATPγS and ADP were determined in this thesis. Compared with the EHD2 structure, the helical domains assume an open conformation featuring a 50° rotation relative to the GTPase domain. Using electron paramagnetic spin resonance (EPR), it was shown that the opening aligns the two membrane-binding regions in the helical domain toward the lipid bilayer, allowing membrane interaction. A loop region in the GTPase domain undergoes a large rearrangement and creates a new interface that allows oligomerization on membranes. These results suggest that the EHD4 structures represent the active EHD conformation, whereas the EHD2 structure is autoinhibited.

A model for the activation and oligomerization of EHD proteins was proposed in which a series of domain rearrangements control membrane recruitment and remodeling in the EHD family. A comparison with other peripheral membrane proteins elucidated common and specific features of this activation mechanism.

# Zusammenfassung

Epidermal growth factor receptor pathway substrate 15-homology domain containing proteins (EHDs) sind mechano-chemische ATPasen, die zur Familie der Dynamine gehören und eine wichtige Rolle im Membrantransport spielen. EHD Proteine bestehen aus einer einer Dynamin-verwandten GTPase Domäne, einer helikalen Domäne und einer C-terminalen Eps15-homology (EH) Domäne. Die Kristallstruktur des EHD2-Dimer war zu Beginn dieser Studie bekannt und zeigte die allgemeine Architektur von EHD Proteinen auf. Vorhergehende Studien konnten ausserdem zeigen, dass die N-terminale Region von EHD2 in eine hydrophobe Furche der GTPase-Domäne bindet und in der Anwesenheit von Liposomen in die Membran wechselt. Der genaue Mechanismus der Membranbindung und Oligomerisierung, und die spezifische Role der Nukleotid-Bindung für diese Prozesse waren jedoch unklar.

Es konnte gezeigt werden, dass die N-terminale Region von EHD2 in eine hydrophobe Furche der GTPase-Domäne bindet. In der Anwesenheit von Liposomen, allerdings, wird diese Region an die Membran dirigiert. Außerdem ist EHD2 ohne N-terminale Region verstärkt in Caveolae vertreten. Um die membranabhängige Aktivierung von EHDs zu verstehen, wurde in dieser Arbeit die Kristallstrukturen eines N-terminal verkürzten EHD4-Konstrukts im Komplex mit ATPγS und ADP bestimmt. Im Vergleich zur EHD2 Struktur sind die helikalen Domänen von EHD4 in einer offenen Konformation und um 50° relativ zur GTPase Domäne gedreht. Mit Hilfe von Elektronenspinresonanz Experimenten konnte gezeigt werden, dass diese Konformationsänderung die membranbindenden Regionen der helikalen Domänen mit der Lipiddoppelschicht aligniert und somit die Membraninteraktion ermöglicht. Weiterhin wird durch die Umorientierung einer Schleife in der GTPase Domäne eine neue Interaktionsfläche gebildet, die zur Oligomerisierung von EHD4 an Membranen beiträgt. Diese Ergebnisse deuten darauf hin, dass die gelösten EHD4 Strukturen die aktive EHD Konformation repräsentieren, während die EHD2 Struktur eine auto-inhibierte Variante aufzeigt.

Basierend auf diesen Erkenntnissen wurde ein Modell für die Aktivierung und Oligomerisierung von EHD Proteinen vorgeschlagen, in welchem mehrere Umlagerungen von Domänen für die Membranbindung und –remodellierung verantwortlich sind. Ein Vergleich mit

anderen peripheren Membranproteinen zeigt Gemeinsamkeiten und Unterschiede dieses Aktivierungsmechanismus auf.

# Appendix A - Dynamin superfamily structures

| Protein | PDB code | Nucleotide loading state | Species | Method | Resolution (Å) | Ref. |
|---|---|---|---|---|---|---|
| ***Dynamin*** | | | | | | |
| Dynamin-1 | 5D3Q | GDP | *Homo sapiens* | X-ray diffraction | 1.7 | (Anand et al., 2016) |
| Dynamin 1 | 4UUD 4UUK | GTP | *Homo sapiens* | cryo-EM | 12.5 | (Sundborger et al., 2014) |
| Dynamin-1 | 3ZYC | GMPPCP | *Homo sapiens* | X-ray diffraction | 2.2 | (Chappie et al., 2011) |
| Dynamin-1 | 3ZYS | GMPPCP | *Homo sapiens* | EM | 12.2 | (Chappie et al., 2011) |
| Dynamin-1 | 3SNH | Nucleotide-free | *Homo sapiens* | X-ray diffraction | 3.7 | (Faelber et al., 2011) |
| Dynamin-1 | 3ZVR | Nucleotide-free | *Rattus norvegicus* | X-ray diffraction | 3.1 | (Ford et al., 2011) |
| Dynamin-1 | 2X2E | GDP-$AlF_4$- | *Homo sapiens* | X-ray diffraction | 2.0 | (Chappie et al., 2010) |
| Dynamin-1 | 2X2F | GDP-$AlF_4$- | *Homo sapiens* | X-ray diffraction | 2.0 | (Chappie et al., 2010) |
| Dynamin-3 | 5A3F | Nucleotide-free | *Homo sapiens* | X-ray diffraction | 3.7 | (Reubold et al., 2015) |
| Dynamin A | 1JWY | GDP | *Dictyostelium discoideum* | X-ray diffraction | 2.3 | (Niemann et al., 2001) |
| Dynamin A | 1JX2 | Nucleotide-free | *Dictyostelium discoideum* | X-ray diffraction | 2.3 | (Niemann et al., 2001) |
| BDLP | 2W6D | GMPPNP | *Nostoc punctiforme* | cryo-EM | ~11 | (Low et al., 2009) |
| BDLP | 2J68 | GDP | *Nostoc punctiforme* | X-ray diffraction | 3.1 | (Low and Löwe, 2006) |

| | | | | | | |
|---|---|---|---|---|---|---|
| BDLP | 2J69 | Nucleotide-free | *Nostoc punctiforme* | X-ray diffraction | 3.0 | (Low and Löwe, 2006) |
| ***Dynamin related proteins*** | | | | | | |
| DRP1 | 3W6N | GMPPNP | *Homo sapiens* | X-ray diffraction | 2.0 | (Kishida and Sugio, 2013) |
| DRP1 | 3W6O | GMPPCP | *Homo sapiens* | X-ray diffraction | 1.9 | (Kishida and Sugio, 2013) |
| DRP1 | 3W6P | GDP-$AlF_4$- | *Homo sapiens* | X-ray diffraction | 1.7 | (Kishida and Sugio, 2013) |
| AtDRP1A | 3T34 | GDP-$AlF_4$- | *Arabidopsis thaliana* | X-ray diffraction | 2.4 | (Yan et al., 2011) |
| AtDRP1A | 3T35 | GDP | *Arabidopsis thaliana* | X-ray diffraction | 3.59 | (Yan et al., 2011) |
| LeoA | 4AUR | Nucleotide-free | *E. coli* | X-ray diffraction | 2.7 | (Michie et al., 2014) |
| ***Mx proteins*** | | | | | | |
| MxA | 5GTM | Nucleotide-free | *Homo spaiens* | X-ray diffraction | 2.9 | (Chen et al., 2017) |
| MxA | 4P4U | Nucleotide-free | *Homo sapiens* | X-ray diffraction | 1.9 | (Rennie et al., 2014) |
| MxA | 4P4S | GMPPCP | *Homo sapiens* | X-ray diffraction | 3.3 | (Rennie et al., 2014) |
| MxA | 4P4T | GDP | *Homo sapiens* | X-ray diffraction | 2.3 | (Rennie et al., 2014) |
| MxA | 3LJB | - | *Homo sapiens* | X-ray diffraction | 2.4 | (Gao et al., 2010) |
| MxA | 3SZR | Nucleotide-free form | *Homo sapiens* | X-ray diffraction | 3.5 | (Gao et al., 2011) |
| MxB | 4X0R | - | *Homo sapiens* | X-ray diffraction | 2.9 | (Xu et al., 2015) |
| ***Atlastin*** | | | | | | |

| | | | | | | |
|---|---|---|---|---|---|---|
| Sey1p | 5CA9 | GDP-$AlF_4$- | *Candida albicans* | X-ray diffraction | 2.8 | (Yan et al., 2015) |
| Sey1p | 5CB2 | GMPPNP | *Candida albicans* | X-ray diffraction | 2.9 | (Yan et al., 2015) |
| Sey1p | 5CA8 | GDP | *Candida albicans* | X-ray diffraction | 2.3 | (Yan et al., 2015) |
| Atlastin | 3X1D | GDP | *Drosophila melanogaster* | X-ray diffraction | 2.87 | (Wu et al., 2015) |
| Atlastin-1 | 4IDN,4IDP | GMPPNP | *Homo sapiens* | X-ray diffraction | 2.25, 2.59 | (Byrnes et al., 2013) |
| Atlastin-1 | 4IDO, 4IDQ | GDP-$AlF_4$- | *Homo sapiens* | X-ray diffraction | 2.09, 2.3 | (Byrnes et al., 2013) |
| Atlastin-1 | 3QNU, 3QOF | GDP | *Homo sapiens* | X-ray diffraction | 2.8, 2.8 | (Bian et al., 2011) |
| Atlastin-1 | 3Q5D, 3Q5E | GDP | *Homo sapiens* | X-ray diffraction | 2.7, 3.01 | (Byrnes and Sondermann, 2011) |
| Atlastin-3 | 5VGR | GDP | *Homo sapiens* | X-ray diffraction | 2.1 | Unpublished |
| ***Mitofusin*** | | | | | | |
| Mitofusin-1 | 5GOM | GDP-$AlF_4$- | *Homo sapiens* | X-ray diffraction | 2.8 | (Cao et al., 2017) |
| Mitofusin-1 | 5GO4 | Nucleotide-free | *Homo sapiens* | X-ray diffraction | 2.2 | (Cao et al., 2017) |
| Mitofusin-1 | 5GOE | GDP | *Homo sapiens* | X-ray diffraction | 1.8 | (Cao et al., 2017) |
| Mitofusin-1 | 5GOF | GTP | *Homo sapiens* | X-ray diffraction | 1.6 | (Cao et al., 2017) |
| Mitofusin-1 | 5GNS | GTP | *Homo sapiens* | X-ray diffraction | 2.7 | Unpublished |
| ***GBP1*** | | | | | | |
| GBP1 | 1DG3 | Nucleotide-free | *Homo sapiens* | X-ray diffraction | 1.8 | (Prakash et al., 2000) |
| GBP1 | 1F5N | GMPPNP | *Homo sapiens* | X-ray diffraction | 1.7 | (Prakash et al., 2000) |
| GBP1 | 2B8W | GMP-$AlF_4$- | *Homo* | X-ray | 2.22 | (Ghosh et |

| | | | | | | |
|---|---|---|---|---|---|---|
| | | | *sapiens* | diffraction | | al., 2006) |
| GBP1 | 2B92 | GDP-$AlF_3$ | *Homo sapiens* | X-ray diffraction | 3.2 | (Ghosh et al., 2006) |
| GBP1 | 2BC9 | GMPPNP | *Homo sapiens* | X-ray diffraction | 2.8 | (Ghosh et al., 2006) |
| GBP1 | 2D4H | GMP | *Homo sapiens* | X-ray diffraction | 2.9 | (Ghosh et al., 2006) |
| ***EHD*** | | | | | | |
| EHD1 | 2JQ6 | - | *Homo sapiens* | Solution NMR | - | (Kieken et al., 2007) |
| EHD2 | 2QPT | AMPPNP | *Mus musculus* | X-ray diffraction | 3.1 | (Daumke et al., 2007) |
| EHD2 | 4CID | AMPPNP | *Mus musculus* | X-ray diffraction | 3.0 | (Shah et al., 2014) |
| EHD4 | 5MTV | ATPγS | *Mus musculus* | X-ray diffraction | 2.79 | (Melo et al., 2017) |
| EHD4 | 5MVF | ADP | *Mus musculus* | X-ray diffraction | 3.27 | (Melo et al., 2017) |
| ***Irga6*** | | | | | | |
| Irga6 | 5FPH | GMPPNP | *Mus musculus* | X-ray diffraction | 3.2 | (Schulte et al., 2016) |
| Irga6 | 4LV5, 4LV8 | GDP | *Mus musculus* | X-ray diffraction | 1.7 | Unpublished |

# Appendix B - List of instruments

| Instruments | Manufacturer |
|---|---|
| Thermocycler TGradient | Biometra, Göttingen, D |
| Thermocycler TPersonal | Biometra, Göttingen, D |
| Agarose Gel Electrophoresis System | OLS, Bremen, D |
| SDS PAGE System Xcell Sure Lock | Invitrogen, Darmstadt, D |
| Western Blot Module Xcell II | Invitrogen, Darmstadt, D |
| Thermomixer Comfort | Eppendorf, Hamburg, D |
| Amicon centrifugal filter devices | Millipore, Billerica, USA |
| Photometer BioPhotometer | Eppendorf, Hamburg, D |
| Photometer NanoDrop 2000 | Thermo Scientific, Dreieich, D |
| Benchtop Centrifuge 5415 R | Eppendorf, Hamburg, D |
| Benchtop Centrifuge 5415 D | Eppendorf, Hamburg, D |
| Benchtop Centrifuge 5804 R | Eppendorf, Hamburg, D |
| Fluidizer M-110L | Pneumatic Microfluidics, Newton, USA |
| Centrifuge Avanti J-26 XP | Beckman Coulter, Krefeld, D |
| Ultracentrifuge Optima L-100K | Beckman Coulter, Krefeld, D |
| Ultracentrifuge Optima TLX | Beckman Coulter, Krefeld, D |
| Chromatography column GSTrap HP 1 mL | GE Healthcare, Piscataway, USA |
| Chromatography column HisTrap HP 1 mL | GE Healthcare, Piscataway, USA |
| Chromatography column material GSH Sepharose 4B | GE Healthcare, Piscataway, USA |
| Chromatography column material Ni Sepharose HP | GE Healthcare, Piscataway, USA |
| Chromatography columns Superdex 75 16/60, 26/60 | GE Healthcare, Piscataway, USA |
| Chromatography columns Superdex 200 16/60, 26/60 | GE Healthcare, Piscataway, USA |
| Chromatography columns XK 16/20, XK 26/20 | GE Healthcare, Piscataway, USA |
| Desalting columns PD-10 | GE Healthcare, Piscataway, USA |
| Peristaltic Pump Reglo Analog ISM827B | Ismatec, Glattbrugg, CH |
| Äkta Prime Plus | GE Healthcare, Piscataway, USA |
| Äkta FPLC | GE Healthcare, Piscataway, USA |
| Äkta Purifier | GE Healthcare, Piscataway, USA |
| RALS Viscotec RImax | Malvern, Malvern, UK |
| DLS Zetasizer Nano ZS90 | Malvern, Malvern, UK |
| CD spectropolarimeter J-720 | Jasco, Tokyo, J |
| HPLC Infinity 1260 | Agilent Technologies, Santa Clara, USA |
| Hypersil ODS guard column | Agilent Technologies, Santa Clara, USA |
| Reversed-phase ODS-2 Hypersil HPLC column | Thermo Scientific, Dreieich, D |
| Isothermal Titration Calorimeter VP-ITC | GE Healthcare, Piscataway, USA |
| Fluorescence Spectrophotometer Varian Cary Eclipse | Agilent Technologies, Santa Clara, USA |
| pH-Meter | Mettler-Toledo, Gießen, D |
| Scales | Sartorius, Göttingen, D |

| | |
|---|---|
| Shaker Incubator Innova44 | New Brunswick Scientific, Edison, USA |
| Matrix Hydra II 96-well liquid handling system | Thermo Scientific, Dreieich, D |
| crystallization plate storage and imaging system | Rock Imager Formulatrix, Waltham, USA |
| EPR Spectrometer Elexsys E500 | Bruker BioSpin, Billerica, USA |
| EPR Spectrometer Elexsys E580 | Bruker BioSpin, Billerica, USA |
| Binocular Microscope MZ 7.5 | Leica, Wetzlar, D |
| Zeiss EM910 | Carl Zeiss, Oberkochen, D |

# Appendix C - List of chemicals

| Chemical / Enzyme / Kit | Cat. No | Manufacturer |
|---|---|---|
| 10 x cloned Pfu reaction buffer | 600153-82 | Stratagene, La Jolla, USA |
| 2-Log DNA ladder | N3200S | NEB, Frankfurt a. M., D |
| Acetic Acid | 3783.5 | Roth, Karlsruhe, D |
| Acetone | 9372.2 | Roth, Karlsruhe, D |
| Acetonitrile | CN20.2 | Roth, Karlsruhe, D |
| Additive Screen | HR2-428 | Hampton Research, Aliso Viejo, USA |
| Agarose | 2267.3 | Roth, Karlsruhe, D |
| Ammonium acetate | 9689 | Sigma-Aldrich, Steinheim, D |
| Ammonium chloride | 9700 | Sigma-Aldrich, Steinheim, D |
| Ammonium citrate dibasic | 9833 | Sigma-Aldrich, Steinheim, D |
| Ammonium fluoride | 9737 | Sigma-Aldrich, Steinheim, D |
| Ammonium formate | 9735 | Sigma-Aldrich, Steinheim, D |
| Ammonium iodide | 9874 | Sigma-Aldrich, Steinheim, D |
| Ammonium nitrate | 9889 | Sigma-Aldrich, Steinheim, D |
| Ammonium phosphate monobasic | 9709 | Sigma-Aldrich, Steinheim, D |
| Ammonium sulfate | 9212.2 | Roth, Karlsruhe, D |
| Autoinduction medium | 71491-5 | Novagen, Darmstadt, D |
| BamHI | R0136S | NEB, Frankfurt a. M., D |
| Boric acid | 5935.2 | Roth, Karlsruhe, D |
| Calcium acetate Hydrate | 21056 | Sigma-Aldrich, Steinheim, D |
| Calcium chloride | A119.1 | Roth, Karlsruhe, D |
| Chloramphenicol | 3886.3 | Roth, Karlsruhe, D |
| Coomassie 108rilliant blue R 250 (C.I. 42660) | 3862.2 | Roth, Karlsruhe, D |
| di-Ammonium hydrogen phosphate | 9839 | Sigma-Aldrich, Steinheim, D |
| di-Potassium hydrogen phosphate anhydrous | P749.2 | Roth, Karlsruhe, D |
| di-Sodium hydrogen phosphate anhydrous | P030.2 | Roth, Karlsruhe, D |
| DMEM | E15-877 | PAA, Pasching, A |
| DNAse I | 04 716 728 001 | Roche, Mannheim, D |
| DpnI | R0176S | NEB, Frankfurt a. M., D |
| DTT | 6908.2 | Roth, Karlsruhe, D |
| EcoRI | R0101S | NEB, Frankfurt a. M., D |
| EDTA | 8040.2 | Roth, Karlsruhe, D |

| | | |
|---|---|---|
| Ethanol | 5054.2 | Roth, Karlsruhe, D |
| Ethidium bromide | 2218.1 | Roth, Karlsruhe, D |
| Fetal bovine serum | A11-211 | PAA laboratories, Pasching, A |
| GDP | NU-1172S | Jena Bioscience, Jena, D |
| GeneAmp© dNTPs | N8080007 | Roche Molecular, Branchburg, USA |
| Glutathione SepharoseTM 4B | 27-4574-01 | Amersham, Piscatawy, USA |
| Glycerol | 3783.1 | Roth, Karlsruhe, D |
| GSH reduced | 3541 | Calbiochem, Darmstadt, D |
| GTP | NU-1012-1G | Jena Bioscience, Jena, D |
| Guanidinehydrochloride | 37.1 | Roth, Karlsruhe, D |
| HEPES | 9105.4 | Roth, Karlsruhe, D |
| HindIII | R0104S | NEB, Frankfurt a. M., D |
| Imidazole | 3899.3 | Roth, Karlsruhe, D |
| Isopropanol | 9866.5 | Roth, Karlsruhe, D |
| Kanamycinsulfate | T823.4 | Roth, Karlsruhe, D |
| Lithium acetate Dihydrate | 62393 | Sigma-Aldrich, Steinheim, D |
| Lithium citrate tribasic Tetrahydrate | 62484 | Sigma-Aldrich, Steinheim, D |
| Lithium nitrate | 62574 | Sigma-Aldrich, Steinheim, D |
| Magnesium acetate Tetrahydrate | 63049 | Sigma-Aldrich, Steinheim, D |
| Magnesium chloride Hexahydrate | 63065 | Sigma-Aldrich, Steinheim, D |
| Magnesium formate Dihydrate | 793 | Sigma-Aldrich, Steinheim, D |
| Magnesium nitrate | 237175-100G | Sigma-Aldrich, Steinheim, D |
| Magnesium sulfate Heptahydrate | 63138 | Sigma-Aldrich, Steinheim, D |
| Malonic acid | 63290 | Sigma-Aldrich, Steinheim, D |
| Mark12TM unstained standard | LC5677 | Life Techologies, Karlsruhe, D |
| Methanol | 4627.5 | Roth, Karlsruhe, D |
| MPD | 68340 | Sigma-Aldrich, Steinheim, D |
| Ni Sepharose HP | 71-5027-67 AD | GE Healthcare, München, D |
| NuPAGE© LDS Sample Buffer (4x) | NP0007 | Life Techologies, Karlsruhe, D |
| NuPAGE© MES SDS Buffer Kit | NP0060 | Life Techologies, Karlsruhe, D |
| NuPAGE© MOPS SDS Buffer Kit | NP0050 | Life Techologies, Karlsruhe, D |
| PBS | H15-002 | PAA, Pasching, A |
| Pefabloc© SC-Protease inhibitor | A154.2 | Roth, Karlsruhe, D |
| PEG 1000 | 81188 | Sigma-Aldrich, Steinheim, D |
| PEG 2000MME | 81321 | Sigma-Aldrich, Steinheim, D |
| PEG 3350 | 88276 | Sigma-Aldrich, Steinheim, D |
| PEG 400 | 91893 | Sigma-Aldrich, Steinheim, D |
| PEG 4000 | 95904 | Sigma-Aldrich, Steinheim, D |
| PEG 500MME | 71578 | Sigma-Aldrich, Steinheim, D |
| PEG 8000 | 89510 | Sigma-Aldrich, Steinheim, D |
| Penicillin-Streptomycin | 15140-122 | Life Techologies, Karlsruhe, D |
| Pfu DNA polymerase | 600153 | Stratagene, La Jolla, USA |
| pGEX-6-P1 | 27-4597-01 | GE Healthcare, München, D |
| Potassium acetate | 60035 | Sigma-Aldrich, Steinheim, D |

| | | |
|---|---|---|
| Potassium chloride | 6781.3 | Roth, Karlsruhe, D |
| Potassium citrate tribasic monohydrate | 25107 | Sigma-Aldrich, Steinheim, D |
| Potassium dihydrogen phosphate | 3904.1 | Roth, Karlsruhe, D |
| Potassium fluoride | 60239 | Sigma-Aldrich, Steinheim, D |
| Potassium formate | 60246 | Sigma-Aldrich, Steinheim, D |
| Potassium iodide | 60400 | Sigma-Aldrich, Steinheim, D |
| Potassium nitrate | 60414 | Sigma-Aldrich, Steinheim, D |
| Potassium phosphate | 3904.3 | Roth, Karlsruhe, D |
| Potassium sulfate | 60528 | Sigma-Aldrich, Steinheim, D |
| Potassium thiocyanate | 60517 | Sigma-Aldrich, Steinheim, D |
| PreScissionTM Protease | 27-0843-01 | GE Healthcare, München, D |
| QIAprepTM Spin Miniprep Kit | 27106 | Qiagen, Hilden, D |
| QIAquick gel extraction kit | 28704 | Qiagen, Hilden, D |
| Fect transfection kit | P001.3 | Roth, Karlsruhe, D |
| Sodium acetate Trihydrate | 71188 | Sigma-Aldrich, Steinheim, D |
| Sodium chloride | 9265.2 | Roth, Karlsruhe, D |
| Sodium citrate tribasic Dihydrate | 71402 | Sigma-Aldrich, Steinheim, D |
| Sodium di-hydrogen phosphate 2-hydrate | T879.1 | Roth, Karlsruhe, D |
| Sodium fluoride | 71519 | Sigma-Aldrich, Steinheim, D |
| Sodium hydroxide | 6771.1 | Roth, Karlsruhe, D |
| Sodium nitrate | 71755 | Sigma-Aldrich, Steinheim, D |
| Sodium sulfate Decahydrate | 71969 | Sigma-Aldrich, Steinheim, D |
| Sodium tartrate dibasic dihydrate | 71994 | Sigma-Aldrich, Steinheim, D |
| Sodium thiocyanate | 71938 | Sigma-Aldrich, Steinheim, D |
| T4 DNA ligase | M0202S | NEB, Frankfurt a. M., D |
| Terrific-Broth medium | HP61.1 | Roth, Karlsruhe, D |
| Tetrabutylammonium bromide | 86860-500G | Sigma-Aldrich, Steinheim, D |
| The Classics II Suite | 130723 | Qiagen, Hilden, D |
| The Classics Suite | 130701 | Qiagen, Hilden, D |
| The JSCG+ Suite | 130720 | Qiagen, Hilden, D |
| The MPD Sutie | 130706 | Qiagen, Hilden, D |
| The pHClear II Suite | 130710 | Qiagen, Hilden, D |
| Trichloromethane | 6340.2 | Roth, Karlsruhe, D |
| Tryptone/peptone | 8952.2 | Roth, Karlsruhe, D |
| Uranyl acetate dihydrate | 73943 | Sigma-Aldrich, Steinheim, D |
| Western Blotting Detection Reagent Amersham ECL Prime | RPN2232 | GE Healthcare, München, D |
| XhoI | R0146L | NEB, Frankfurt a. M., D |
| Yeast extract | 2363.2 | Roth, Karlsruhe, D |
| Zinc acetate Dihydrate | 96459 | Sigma-Aldrich, Steinheim, D |

# Appendix D - List of enzymes

| Enzyme | Manufacturer |
|---|---|
| DNAse I | Roche, Mannheim, D |
| GST-PreScission Protease | GE Healthcare, Piscataway, USA |
| Pfu DNA Polymerase | EURx, Gdansk, PL |
| Restiction Endonucleases | New England Biolabs, Frankfurt am Main, D |
| T4 DNA Ligase | New England Biolabs, Frankfurt am Main, D |

# Appendix E - List of kits

| Kit | Manufacturer |
|---|---|
| 2-Log DNA ladder | New England Biolabs, Frankfurt am Main, D |
| Unstained Protein Molecular Weight Marker | Fermentas, St. Leon-Rot, D |
| Mark 12 unstained protein standard | life technologies, Carlsbad, USA |
| Bradford protein assay | Bio-Rad, München, D |
| GeneAmp dNTPs | Roche, Mannheim, D |
| NuPAGE LDS Sample Buffer (4x) | life technologies, Carlsbad, USA |
| NuPAGE MES SDS Buffer | life technologies, Carlsbad, USA |
| NuPAGE MOPS SDS Buffer | life technologies, Carlsbad, USA |
| NuPAGE Novex 4-12% Bis-Tris | life technologies, Carlsbad, USA |
| QIAprep Spin Miniprep Kit | Qiagen, Hilden, D |
| QIAquick PCR Purification Kit | Qiagen, Hilden, D |
| QIAquick Gel Extraction Kit | Qiagen, Hilden, D |
| QuickChange | Agilent Technologies, Santa Clara, USA |
| Additive Screen | Hampton Research, Aliso Viejo, USA |
| The Classics Suite | Qiagen, Hilden, D |
| The JSCG+ Suite | Qiagen, Hilden, D |
| The PEGs Suite | Qiagen, Hilden, D |
| The PEGs II Suite | Qiagen, Hilden, D |
| The ProComplex Suite | Qiagen, Hilden, D |

# Appendix F - List of medium

| Medium | Components |
|---|---|
| **Luria-Bertani (LB)** | 5 g/l yeast extract<br>10 g/l tryptone<br>5 g/l NaCl |
| | 12.8 g/l Na2HPO4<br>4 g/l KH2PO4<br>1 g/l NaCl |
| | 50 mg/l EDTA<br>5 mg/l FeSO4<br>0.5 mg/l ZnCl2<br>0.1 mg/l CoSO4<br>0.1 mg/l CuCl2<br>0.1 mg/l H3 BO3 |
| | 1 mM MgSO4<br>0.3 mM CaCl2 |
| | 2 g/l glucose<br>0.5 g/l NH4Cl<br>1.5 mg/l Thiamin<br>1.5 mg/l Biotin |
| **Terrific Broth (TB)** | ordered from Carl Roth (HP61.1) |
| | ordered from Thermofisher |
| **DMEM medium** | Scientific |

# Appendix G - List of buffers

| Buffer | Components |
|---|---|
| **Resuspension buffer** | 50 mM HEPES pH 7.5<br>500 mM NaCl<br>2.5 mM β-mercaptoethanol<br>250 µM Pefabloc<br>1 µg/mL DNase I<br>1 mM MgCl2<br>25 mM imidazole |
| **Equilibration buffer** | 50 mM HEPES pH 7.5<br>500 mM NaCl<br>2.5 mM β-mercaptoethanol<br>25 mM imidazole |
| **Washing buffer** | 50 mM HEPES pH 7.5<br>700 mM NaCl<br>2.5 mM β-mercaptoethanol<br>30 mM imidazole<br>5 mM KH2 PO4<br>5 mM K2 HPO4<br>1 mM ATP |
| **Dialysis Buffer** | 50 mM HEPES pH 7.5<br>500 mM NaCl<br>2.5 mM β-mercaptoethanol<br>1 mM MgCl2 |
| **Elution buffer I** | 50 mM HEPES pH 7.5<br>300 mM NaCl<br>2.5 mM β-mercaptoethanol<br>300 mM imidazole |
| **Elution buffer II** | 50 mM HEPES pH 7.5<br>300 mM NaCl<br>2.5 mM β-mercaptoethanol<br>50 mM imidazole |
| **SEC buffer** | 50 mM HEPES pH 7.5<br>500 mM NaCl<br>2.5 mM β-mercaptoethanol<br>1 mM MgCl2 |
| **Liposome Buffer** | 20 mM HEPES pH 7.5<br>300 mM NaCl<br>1 mM DTT |

| | |
|---|---|
| **ATPase Buffer** | 20 mM HEPES pH 7.5<br>300 mM NaCl<br>2.5 mM β-mercaptoethanol<br>0.5 mM MgCl2 |
| **HPLC Buffer** | 100 mM potassium phosphate buffer pH 6.5<br>10 mM tetrabutylammonium bromide<br>7.5% acetonitrile |

# Appendix H - List of constructs

| Protein | Residues (Start-End) | Species | Plasmid | Mutation |
|---|---|---|---|---|
| EHD1 (Q9WVK4) | 1-534 | *Mus musculus* | pSKB_LNB/pGEX_6P1 | |
| | 1-417 | *Mus musculus* | pSKB_LNB/pGEX_6P1 | |
| | 1-404 | *Mus musculus* | pSKB_LNB/pGEX_6P1 | |
| | 1-369 | *Mus musculus* | pSKB_LNB/pGEX_6P1 | |
| | 16-534 | *Mus musculus* | pSKB_LNB/pGEX_6P1 | |
| | 16-417 | *Mus musculus* | pSKB_LNB/pGEX_6P1 | |
| | 16-404 | *Mus musculus* | pSKB_LNB/pGEX_6P1 | |
| | 16-369 | *Mus musculus* | pSKB_LNB/pGEX_6P1 | |
| | 47-534 | *Mus musculus* | pSKB_LNB/pGEX_6P1 | |
| | 47-417 | *Mus musculus* | pSKB_LNB/pGEX_6P1 | |
| | 47-404 | *Mus musculus* | pSKB_LNB/pGEX_6P1 | |
| | 47-369 | *Mus musculus* | pSKB_LNB/pGEX_6P1 | |
| EHD2 (Q8BH64) | 1-418 | *Mus musculus* | pSKB_LNB/pGEX_6P1 | |
| | 1-373 | *Mus musculus* | pSKB_LNB/pGEX_6P1 | |
| | 16-418 | *Mus musculus* | pSKB_LNB/pGEX_6P1 | |
| | 16-373 | *Mus musculus* | pSKB_LNB/pGEX_6P1 | |
| | 47-418 | *Mus musculus* | pSKB_LNB/pGEX_6P1 | |
| | 47-373 | *Mus musculus* | pSKB_LNB/pGEX_6P1 | |
| EHD3 (Q9NZN3) | 1-535 | *Homo sapiens* | pSKB_LNB/pGEX_6P1 | |
| | 1-417 | *Homo sapiens* | pSKB_LNB/pGEX_6P1 | |
| | 1-404 | *Homo sapiens* | pSKB_LNB/pGEX_6P1 | |
| | 1-369 | *Homo sapiens* | pSKB_LNB/pGEX_6P1 | |
| | 13-534 | *Homo sapiens* | pSKB_LNB/pGEX_6P1 | |
| | 13-417 | *Homo sapiens* | pSKB_LNB/pGEX_6P1 | |
| | 13-404 | *Homo sapiens* | pSKB_LNB/pGEX_6P1 | |
| | 13-369 | *Homo sapiens* | pSKB_LNB/pGEX_6P1 | |
| | 47-535 | *Homo sapiens* | pSKB_LNB/pGEX_6P1 | |
| | 47-417 | *Homo sapiens* | pSKB_LNB/pGEX_6P1 | |
| | 47-404 | *Homo sapiens* | pSKB_LNB/pGEX_6P1 | |
| | 47-369 | *Homo sapiens* | pSKB_LNB/pGEX_6P1 | |
| EHD4 (Q9EQP2) | 22-541 | *Mus musculus* | pSKB_LNBp/GEX_6P1 | |
| | 22-541 | *Mus musculus* | pSKB_LNBp | F125A and K302A/R305A |
| | 1-541 | *Mus musculus* | mCherry-N1 | A116L, N133D and A116L/N133D |

| | | | |
|---|---|---|---|
| 22-541 | *Mus musculus* | mCherry-N1 | F125A and K302A/R305A |
| 22-420 | *Mus musculus* | pSKB_LNB/pGEX_6P1 | |
| 22-404 | *Mus musculus* | pSKB_LNB/pGEX_6P1 | |
| 22-372 | *Mus musculus* | pSKB_LNB/pGEX_6P1 | |
| 50-541 | *Mus musculus* | pSKB_LNB/pGEX_6P1 | |
| 50-420 | *Mus musculus* | pSKB_LNB/pGEX_6P1 | |
| 50-404 | *Mus musculus* | pSKB_LNB/pGEX_6P1 | |
| 50-372 | *Mus musculus* | pSKB_LNB/pGEX_6P1 | |

# Appendix I - Sequence alignment of EHD proteins

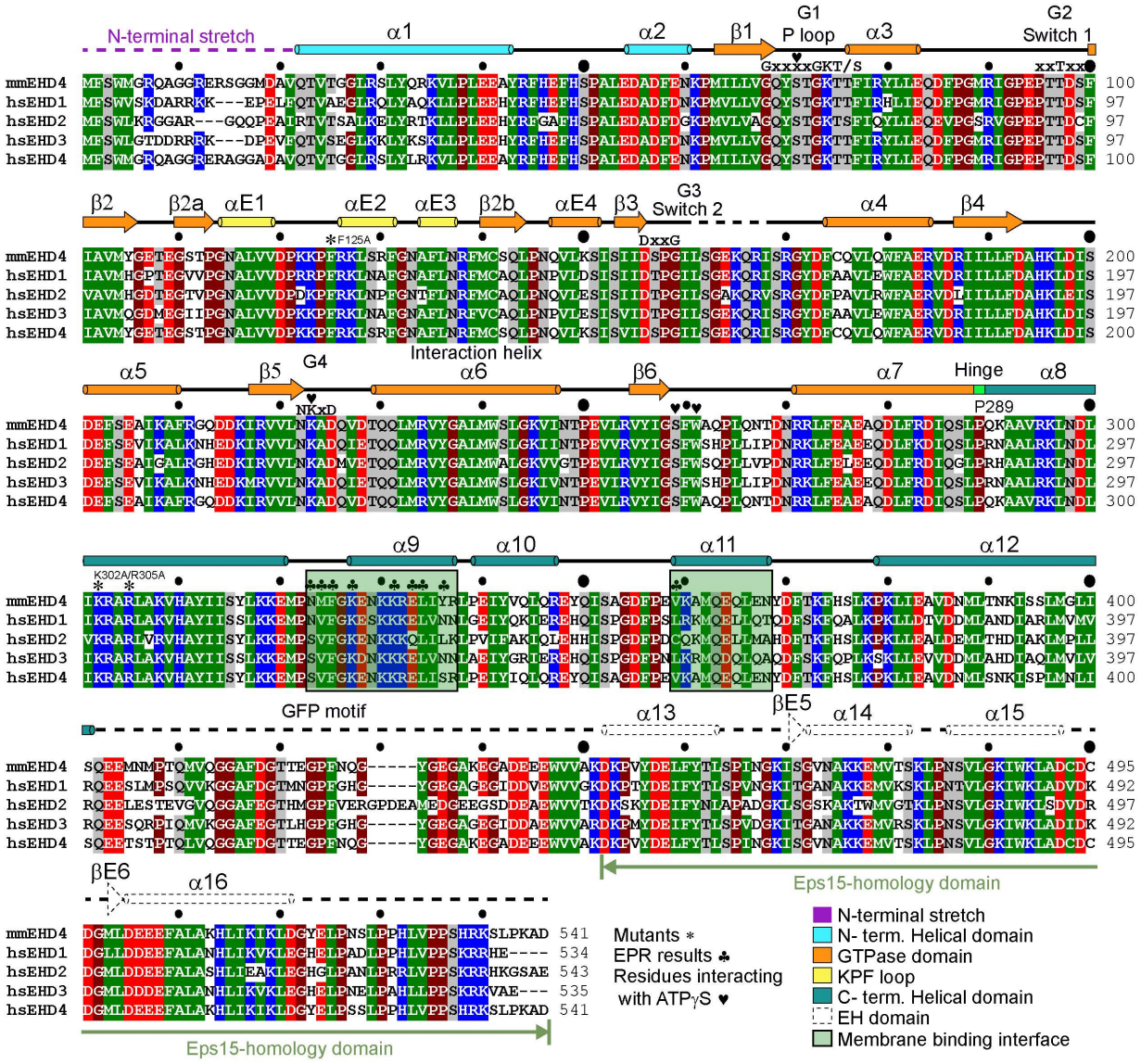


**Sequence alignment of the crystallized mmEHD4 and human EHDs.** Amino acid sequences of Mus musculus (mm) EHD4 (Q9EQP2), Homo sapiens (hs) EHD1 (Q9H4M9), hsEHD2 (Q9NZN4), hsEHD3 (Q9NZN3), and hsEHD4 (Q9H223) were aligned by using CLUSTAL W and manually adjusted. Residues with a conservation greater than 70% are color-coded (D, E in red; R, K, H in blue N, Q, S, T in gray; A, L, I, V, F, Y, W, M, C in green and P, G in brown). α-Helices are shown as cylinders and β-strands as arrows. The secondary structure of the EH domain is from PDB ID code 4CID. The domains are colored as in Fig. 1E. Mutated residues in this study are indicated with an asterisk (*), residues interacting with the membrane are indicated with a clover (♣), and residues interacting with ATPγS are indicated with a heart (♥).

# References


Adams, P.D., Afonine, P.V., Bunkoczi, G., Chen, V.B., Davis, I.W., Echols, N., Headd, J.J., Hung, L.W., Kapral, G.J., Grosse-Kunstleve, R.W., et al. (2010). PHENIX: a comprehensive Python-based system for macromolecular structure solution. Acta Crystallogr Biol Crystallogr *66*, 213–221.

Adl, S.M., Simpson, A.G.B., Lane, C.E., Lukeš, J., Bass, D., Bowser, S.S., Brown, M.W., Burki, F., Dunthorn, M., Hampl, V., et al. (2012). The revised classification of eukaryotes. J. Eukaryot. Microbiol. *59*, 429–493.

Altenbach, C., Greenhalgh, D.A., Khorana, H.G., and Hubbell, W.L. (1994). A collision gradient method to determine the immersion depth of nitroxides in lipid bilayers: application to spin-labeled mutants of bacteriorhodopsin. Proc Natl Acad Sci U A *91*, 1667–1671.

Anand, R., Eschenburg, S., and Reubold, T.F. (2016). Crystal structure of the GTPase domain and the bundle signalling element of dynamin in the GDP state. Biochem. Biophys. Res. Commun. *469*, 76–80.

Anderson, C.A., and Blackstone, C. (2013). SUMO wrestling with Drp1 at mitochondria. EMBO J. *32*, 1496–1498.

Antonny, B., Burd, C., De Camilli, P., Chen, E., Daumke, O., Faelber, K., Ford, M., Frolov, V.A., Frost, A., Hinshaw, J.E., et al. (2016). Membrane fission by dynamin: what we know and what we need to know. EMBO J. *35*, 2270–2284.

Bahl, K., Xie, S., Spagnol, G., Sorgen, P., Naslavsky, N., and Caplan, S. (2016). EHD3 Protein Is Required for Tubular Recycling Endosome Stabilization, and an Asparagine-Glutamic Acid Residue Pair within Its Eps15 Homology (EH) Domain Dictates Its Selective Binding to NPF Peptides. J. Biol. Chem. *291*, 13465–13478.

Ban, T., Heymann, J.A.W., Song, Z., Hinshaw, J.E., and Chan, D.C. (2010). OPA1 disease alleles causing dominant optic atrophy have defects in cardiolipin-stimulated GTP hydrolysis and membrane tubulation. Hum. Mol. Genet. *19*, 2113–2122.

Barlow, D.J., and Thornton, J.M. (1988). Helix geometry in proteins. J. Mol. Biol. *201*, 601–619.

Barylko, B. (1998). Synergistic Activation of Dynamin GTPase by Grb2 and Phosphoinositides. J. Biol. Chem. *273*, 3791–3797.

Barylko, B., Wang, L., Binns, D.D., Ross, J.A., Tassin, T.C., Collins, K.A., Jameson, D.M., and Albanesi, J.P. (2010). The Proline/Arginine-Rich Domain Is a Major Determinant of Dynamin Self-Activation. Biochemistry (Mosc.) *49*, 10592–10594.

Bethoney, K.A., King, M.C., Hinshaw, J.E., Ostap, E.M., and Lemmon, M.A. (2009). A possible effector role for the pleckstrin homology (PH) domain of dynamin. Proc. Natl. Acad. Sci. *106*, 13359–13364.

Bian, X., Klemm, R.W., Liu, T.Y., Zhang, M., Sun, S., Sui, X., Liu, X., Rapoport, T.A., and Hu, J. (2011). Structures of the atlastin GTPase provide insight into homotypic fusion of endoplasmic reticulum membranes. Proc Natl Acad Sci U A.

Bonifacino, J.S., and Glick, B.S. (2004). The mechanisms of vesicle budding and fusion. Cell *116*, 153–166.

Brandt, T., Cavellini, L., Kühlbrandt, W., and Cohen, M.M. (2016). A mitofusin-dependent docking ring complex triggers mitochondrial fusion *in vitro*. eLife *5*.

Braun, A., Pinyol, R., Dahlhaus, R., Koch, D., Fonarev, P., Grant, B.D., Kessels, M.M., and Qualmann, B. (2005). EHD proteins associate with syndapin I and II and such interactions play a crucial role in endosomal recycling. Mol Biol Cell *16*, 3642–3658.

Bustillo-Zabalbeitia, I., Montessuit, S., Raemy, E., Basañez, G., Terrones, O., and Martinou, J.-C. (2014). Specific Interaction with Cardiolipin Triggers Functional Activation of Dynamin-Related Protein 1. PLoS ONE *9*, e102738.

Byrnes, L.J., and Sondermann, H. (2011). Structural basis for the nucleotide-dependent dimerization of the large G protein atlastin-1/SPG3A. Proc Natl Acad Sci U A.

Byrnes, L.J., Singh, A., Szeto, K., Benvin, N.M., O'Donnell, J.P., Zipfel, W.R., and Sondermann, H. (2013). Structural basis for conformational switching and GTP loading of the large G protein atlastin. EMBO J *32*, 369–384.

Cai, B., Xie, S., Caplan, S., and Naslavsky, N. (2014). GRAF1 forms a complex with MICAL-L1 and EHD1 to cooperate in tubular recycling endosome vesiculation. Front Cell Dev Biol *2*, 22.

Campelo, F., McMahon, H.T., and Kozlov, M.M. (2008). The hydrophobic insertion mechanism of membrane curvature generation by proteins. Biophys J *95*, 2325–2339.

Cao, Y.-L., Meng, S., Chen, Y., Feng, J.-X., Gu, D.-D., Yu, B., Li, Y.-J., Yang, J.-Y., Liao, S., Chan, D.C., et al. (2017). MFN1 structures reveal nucleotide-triggered dimerization critical for mitochondrial fusion. Nature *542*, 372–376.

Caplan, S., Naslavsky, N., Hartnell, L.M., Lodge, R., Polishchuk, R.S., Donaldson, J.G., and Bonifacino, J.S. (2002). A tubular EHD1-containing compartment involved in the recycling of major histocompatibility complex class I molecules to the plasma membrane. EMBO J *21*, 2557–2567.

Chappie, J.S., and Dyda, F. (2013). Building a fission machine - structural insights into dynamin assembly and activation. J. Cell Sci. *126*, 2773–2784.

Chappie, J.S., Acharya, S., Leonard, M., Schmid, S.L., and Dyda, F. (2010). G domain dimerization controls dynamin's assembly-stimulated GTPase activity. Nature *465*, 435–440.

Chappie, J.S., Mears, J.A., Fang, S., Leonard, M., Schmid, S.L., Milligan, R.A., Hinshaw, J.E., and Dyda, F. (2011). A pseudoatomic model of the dynamin polymer identifies a hydrolysis-dependent powerstroke. Cell *147*, 209–222.

Chen, V.B., Arendall, W.B., III, Headd, J.J., Keedy, D.A., Immormino, R.M., Kapral, G.J., Murray, L.W., Richardson, J.S., and Richardson, D.C. (2010). MolProbity: all-atom structure validation for macromolecular crystallography. Acta Crystallogr Biol Crystallogr *66*, 12–21.

Chen, Y., Zhang, L., Graf, L., Yu, B., Liu, Y., Kochs, G., Zhao, Y., and Gao, S. (2017). Conformational dynamics of dynamin-like MxA revealed by single-molecule FRET. Nat. Commun. *8*, 15744.

Cho, W., and Stahelin, R.V. (2005). Membrane-protein interactions in cell signaling and membrane trafficking. Annu. Rev. Biophys. Biomol. Struct. *34*, 119–151.

Chung, C.T., Niemela, S.L., and Miller, R.H. (1989). One-step preparation of competent Escherichia coli: transformation and storage of bacterial cells in the same solution. Proc Natl Acad Sci U A *86*, 2172–2175.

Clinton, R.W., Francy, C.A., Ramachandran, R., Qi, X., and Mears, J.A. (2016). Dynamin-related Protein 1 Oligomerization in Solution Impairs Functional Interactions with Membrane-anchored Mitochondrial Fission Factor. J. Biol. Chem. *291*, 478–492.

Cook, T., Mesa, K., and Urrutia, R. (1996). Three dynamin-encoding genes are differentially expressed in developing rat brain. J. Neurochem. *67*, 927–931.

Cook, T.A., Urrutia, R., and McNiven, M.A. (1994). Identification of dynamin 2, an isoform ubiquitously expressed in rat tissues. Proc. Natl. Acad. Sci. *91*, 644–648.

Daumke, O., and Praefcke, G.J. (2016). Mechanisms of GTP hydrolysis and conformational transitions in the dynamin superfamily. Biopolymers *105*, 580–593.

Daumke, O., and Roux, A. (2017). Mitochondrial Homeostasis: How Do Dimers of Mitofusins Mediate Mitochondrial Fusion? Curr. Biol. CB *27*, R353–R356.

Daumke, O., Lundmark, R., Vallis, Y., Martens, S., Butler, P.J., and McMahon, H.T. (2007). Architectural and mechanistic insights into an EHD ATPase involved in membrane remodelling. Nature *449*, 923–927.

Dick, A., Graf, L., Olal, D., von der Malsburg, A., Gao, S., Kochs, G., and Daumke, O. (2015). Role of Nucleotide Binding and GTPase Domain Dimerization in Dynamin-like Myxovirus Resistance Protein A for GTPase Activation and Antiviral Activity. J. Biol. Chem. *290*, 12779–12792.

Doherty, K.R., Demonbreun, A., Wallace, G.Q., Cave, A., Posey, A.D., Heretis, K., Pytel, P., and McNally, E.M. (2008). The endocytic recycling protein EHD2 interacts with myoferlin to regulate myoblast fusion. J Biol Chem.

Durieux, A.-C., Prudhon, B., Guicheney, P., and Bitoun, M. (2010). Dynamin 2 and human diseases. J. Mol. Med. *88*, 339–350.

Emsley, P., Lohkamp, B., Scott, W.G., and Cowtan, K. (2010). Features and development of Coot. Acta Crystallogr Biol Crystallogr *66*, 486–501.

Faelber, K., Posor, Y., Gao, S., Held, M., Roske, Y., Schulze, D., Haucke, V., Noé, F., and Daumke, O. (2011). Crystal structure of nucleotide-free dynamin. Nature *477*, 556–560.

Faelber, K., Gao, S., Held, M., Posor, Y., Haucke, V., Noe, F., and Daumke, O. (2013). Oligomerization of dynamin superfamily proteins in health and disease. Prog Mol Biol Transl Sci *117*, 411–443.

Ferguson, K.M., Lemmon, M.A., Schlessinger, J., and Sigler, P.B. (1994). Crystal structure at 2.2 A resolution of the pleckstrin homology domain from human dynamin. Cell *79*, 199–209.

Ford, M.G.J., Jenni, S., and Nunnari, J. (2011). The crystal structure of dynamin. Nature *477*, 561–566.

Fröhlich, C., Grabiger, S., Schwefel, D., Faelber, K., Rosenbaum, E., Mears, J., Rocks, O., and Daumke, O. (2013). Structural insights into oligomerization and mitochondrial remodelling of dynamin 1-like protein. EMBO J. *32*, 1280–1292.

Gallop, J.L., Jao, C.C., Kent, H.M., Butler, P.J., Evans, P.R., Langen, R., and McMahon, H.T. (2006). Mechanism of endophilin N-BAR domain-mediated membrane curvature. EMBO J *25*, 2898–2910.

Gao, S., von der Malsburg, A., Paeschke, S., Behlke, J., Haller, O., Kochs, G., and Daumke, O. (2010). Structural basis of oligomerization in the stalk region of dynamin-like MxA. Nature *465*, 502–506.

Gao, S., von der Malsburg, A., Dick, A., Faelber, K., Schröder, G.F., Haller, O., Kochs, G., and Daumke, O. (2011). Structure of Myxovirus Resistance Protein A Reveals Intra- and Intermolecular Domain Interactions Required for the Antiviral Function. Immunity *35*, 514–525.

Gasper, R., Meyer, S., Gotthardt, K., Sirajuddin, M., and Wittinghofer, A. (2009). It takes two to tango: regulation of G proteins by dimerization. Nat Rev Mol Cell Biol *10*, 423–429.

Ghosh, A., Praefcke, G.J.K., Renault, L., Wittinghofer, A., and Herrmann, C. (2006). How guanylate-binding proteins achieve assembly-stimulated processive cleavage of GTP to GMP. Nature *440*, 101–104.

Giridharan, S.S.P., Cai, B., Vitale, N., Naslavsky, N., and Caplan, S. (2013). Cooperation of MICAL-L1, syndapin2, and phosphatidic acid in tubular recycling endosome biogenesis. Mol. Biol. Cell *24*, 1776–1790.

Grant, B.D., and Caplan, S. (2008). Mechanisms of EHD/RME-1 protein function in endocytic transport. Traffic *9*, 2043–2052.

Grant, B.D., and Donaldson, J.G. (2009). Pathways and mechanisms of endocytic recycling. Nat. Rev. Mol. Cell Biol. *10*, 597–608.

Gruenberg, J. (2001). The endocytic pathway: a mosaic of domains. Nat. Rev. Mol. Cell Biol. *2*, 721–730.

Gudmundsson, H., Hund, T.J., Wright, P.J., Kline, C.F., Snyder, J.S., Qian, L., Koval, O.M., Cunha, S.R., George, M., Rainey, M.A., et al. (2010). EH Domain Proteins Regulate Cardiac Membrane Protein Targeting. Circ. Res. *107*, 84–95.

Guilherme, A., Soriano, N.A., Bose, S., Holik, J., Bose, A., Pomerleau, D.P., Furcinitti, P., Leszyk, J., Corvera, S., and Czech, M.P. (2004). EHD2 and the novel EH domain binding protein EHBP1 couple endocytosis to the actin cytoskeleton. J Biol Chem *279*, 10593–10605.

Haller, O., and Kochs, G. (2011). Human MxA Protein: An Interferon-Induced Dynamin-Like GTPase with Broad Antiviral Activity. J. Interferon Cytokine Res. *31*, 79–87.

Haller, O., Gao, S., von der Malsburg, A., Daumke, O., and Kochs, G. (2010). Dynamin-like MxA GTPase: structural insights into oligomerization and implications for antiviral activity. J Biol Chem *285*, 28419–28424.

Haslam, R.J., Koide, H.B., and Hemmings, B.A. (1993). Pleckstrin domain homology. Nature *363*, 309–310.

Heymann, J.A.W., and Hinshaw, J.E. (2009). Dynamins at a glance. J. Cell Sci. *122*, 3427–3431.

Hinshaw, J.E., and Schmid, S.L. (1995). Dynamin self-assembles into rings suggesting a mechanism for coated vesicle budding. Nature *374*, 190–192.

Hoernke, M., Mohan, J., Larsson, E., Blomberg, J., Kahra, D., Westenhoff, S., Schwieger, C., and Lundmark, R. (2017). EHD2 restrains dynamics of caveolae by an ATP-dependent, membrane-bound, open conformation. Proc. Natl. Acad. Sci. *114*, E4360–E4369.

Hoppins, S., Lackner, L., and Nunnari, J. (2007). The Machines that Divide and Fuse Mitochondria. Annu. Rev. Biochem. *76*, 751–780.

Ingerman, E., Perkins, E.M., Marino, M., Mears, J.A., McCaffery, J.M., Hinshaw, J.E., and Nunnari, J. (2005). Dnm1 forms spirals that are structurally tailored to fit mitochondria. J Cell Biol *170*, 1021–1027.

Jahn, R., Lang, T., and Südhof, T.C. (2003). Membrane Fusion. Cell *112*, 519–533.

Jao, C.C., Hegde, B.G., Gallop, J.L., Hegde, P.B., McMahon, H.T., Haworth, I.S., and Langen, R. (2010). Roles of Amphipathic Helices and the Bin/Amphiphysin/Rvs (BAR) Domain of Endophilin in Membrane Curvature Generation. J Biol Chem *285*, 20164–20170.

Jovic, M., Naslavsky, N., Rapaport, D., Horowitz, M., and Caplan, S. (2007). EHD1 regulates beta1 integrin endosomal transport: effects on focal adhesions, cell spreading and migration. J. Cell Sci. *120*, 802–814.

Kabsch, W. (2010). XDS. Acta Crystallogr Biol Crystallogr *66*, 125–132.

Kenniston, J.A., and Lemmon, M.A. (2010). Dynamin GTPase regulation is altered by PH domain mutations found in centronuclear myopathy patients. EMBO J. *29*, 3054–3067.

Kieken, F., Jovi?, M., Naslavsky, N., Caplan, S., and Sorgen, P.L. (2007). EH domain of EHD1. J. Biomol. NMR *39*, 323–329.

Kim, A.S., Kakalis, L.T., Abdul-Manan, N., Liu, G.A., and Rosen, M.K. (2000). Autoinhibition and activation mechanisms of the Wiskott-Aldrich syndrome protein. Nature *404*, 151–158.

Kishida, H., and Sugio, S. (2013). Crystal structure of GTPase domain fused with minimal stalks from human dynamin-1-like protein (Dlp1) in complex with several nucleotide analogues. Curr Top Pept Protein Res *14*, 67.

Krug, M., Weiss, M.S., Heinemann, U., and Müller, U. (2012). XDSAPP : a graphical user interface for the convenient processing of diffraction data using XDS. J Appl Crystallogr *45*, 568–572.

Kuo, H.J., Tran, N.T., Clary, S.A., Morris, N.P., and Glanville, R.W. (2001). Characterization of EHD4, an EH domain-containing protein expressed in the extracellular matrix. J Biol Chem *276*, 43103–43110.

Labbé, K., Murley, A., and Nunnari, J. (2014). Determinants and Functions of Mitochondrial Behavior. Annu. Rev. Cell Dev. Biol. *30*, 357–391.

Lai, C.L., Jao, C.C., Lyman, E., Gallop, J.L., Peter, B.J., McMahon, H.T., Langen, R., and Voth, G.A. (2012). Membrane binding and self-association of the epsin N-terminal homology domain. J Mol Biol *423*, 800–817.

Lee, D.W., Zhao, X., Scarselletta, S., Schweinsberg, P.J., Eisenberg, E., Grant, B.D., and Greene, L.E. (2005). ATP binding regulates oligomerization and endosome association of RME-1 family proteins. J Biol Chem *280*, 17213–17220.

Lemmon, M.A. (2007). Pleckstrin homology (PH) domains and phosphoinositides. Biochem. Soc. Symp. *74*, 81.

Li, G., and Zhang, X.C. (2004). GTP hydrolysis mechanism of Ras-like GTPases. J. Mol. Biol. *340*, 921–932.

Liu, R., and Chan, D.C. (2017). OPA1 and cardiolipin team up for mitochondrial fusion. Nat. Cell Biol.

Liu, T.Y., Bian, X., Romano, F.B., Shemesh, T., Rapoport, T.A., and Hu, J. (2015). Cis and trans interactions between atlastin molecules during membrane fusion. Proc. Natl. Acad. Sci. *112*, E1851–E1860.

Losón, O.C., Liu, R., Rome, M.E., Meng, S., Kaiser, J.T., Shan, S., and Chan, D.C. (2014). The Mitochondrial Fission Receptor MiD51 Requires ADP as a Cofactor. Structure *22*, 367–377.

Low, H.H., and Löwe, J. (2006). A bacterial dynamin-like protein. Nature *444*, 766–769.

Low, H.H., Sachse, C., Amos, L.A., and Löwe, J. (2009). Structure of a bacterial dynamin-like protein lipid tube provides a mechanism for assembly and membrane curving. Cell *139*, 1342–1352.

von der Malsburg, A., Abutbul-Ionita, I., Haller, O., Kochs, G., and Danino, D. (2011). Stalk domain of the dynamin-like MxA GTPase protein mediates membrane binding and liposome tubulation via the unstructured L4 loop. J Biol Chem *286*, 37858–37865.

Marg, A., Schoewel, V., Timmel, T., Schulze, A., Shah, C., Daumke, O., and Spuler, S. (2012). Sarcolemmal Repair Is a Slow Process and Includes EHD2: EHD2 in Membrane Repair. Traffic *13*, 1286–1294.

Margittai, M., and Langen, R. (2006). Spin labeling analysis of amyloids and other protein aggregates. Methods Enzym. *413*, 122–139.

Marks, B., Stowell, M.H., Vallis, Y., Mills, I.G., Gibson, A., Hopkins, C.R., and McMahon, H.T. (2001). GTPase activity of dynamin and resulting conformation change are essential for endocytosis. Nature *410*, 231–235.

McBride, H.M., and Frost, A. (2016). Cell biology: Double agents for mitochondrial division. Nature *540*, 43–44.

McCoy, A.J., Grosse-Kunstleve, R.W., Adams, P.D., Winn, M.D., Storoni, L.C., and Read, R.J. (2007). Phaser crystallographic software. J Appl Crystallogr *40*, 658–674.

McCullough, J., Clippinger, A.K., Talledge, N., Skowyra, M.L., Saunders, M.G., Naismith, T.V., Colf, L.A., Afonine, P., Arthur, C., Sundquist, W.I., et al. (2015). Structure and membrane remodeling activity of ESCRT-III helical polymers. Science *350*, 1548–1551.

McMahon, H.T., and Gallop, J.L. (2005). Membrane curvature and mechanisms of dynamic cell membrane remodelling. Nature *438*, 590–596.

Melo, A.A., Hegde, B.G., Shah, C., Larsson, E., Isas, J.M., Kunz, S., Lundmark, R., Langen, R., and Daumke, O. (2017). Structural insights into the activation mechanism of dynamin-like EHD ATPases. Proc. Natl. Acad. Sci. *114*, 5629–5634.

Michie, K.A., Boysen, A., Low, H.H., M?ller-Jensen, J., and L?we, J. (2014). LeoA, B and C from Enterotoxigenic Escherichia coli (ETEC) Are Bacterial Dynamins. PLoS ONE *9*, e107211.

Misura, K.M., Scheller, R.H., and Weis, W.I. (2000). Three-dimensional structure of the neuronal-Sec1-syntaxin 1a complex. Nature *404*, 355–362.

Mizuno, N., Jao, C.C., Langen, R., and Steven, A.C. (2010). Multiple modes of endophilin-mediated conversion of lipid vesicles into coated tubes: implications for synaptic endocytosis. J Biol Chem.

Moren, B., Shah, C., Howes, M.T., Schieber, N.L., McMahon, H.T., Parton, R.G., Daumke, O., and Lundmark, R. (2012). EHD2 regulates caveolar dynamics via ATP-driven targeting and oligomerization. Mol Biol Cell *23*, 1316–1329.

Moss, T.J., Andreazza, C., Verma, A., Daga, A., and McNew, J.A. (2011). Membrane fusion by the GTPase atlastin requires a conserved C-terminal cytoplasmic tail and dimerization through the middle domain. Proc. Natl. Acad. Sci. *108*, 11133–11138.

Naslavsky, N. (2004). Rabenosyn-5 and EHD1 Interact and Sequentially Regulate Protein Recycling to the Plasma Membrane. Mol. Biol. Cell *15*, 2410–2422.

Naslavsky, N., and Caplan, S. (2011). EHD proteins: key conductors of endocytic transport. Trends Cell Biol *21*, 122–131.

Naslavsky, N., Rahajeng, J., Sharma, M., Jovic, M., and Caplan, S. (2006). Interactions between EHD proteins and Rab11-FIP2: a role for EHD3 in early endosomal transport. Mol Biol Cell *17*, 163–177.

Naslavsky, N., Rahajeng, J., Chenavas, S., Sorgen, P.L., and Caplan, S. (2007). EHD1 and Eps15 interact with phosphatidylinositols via their Eps15 homology domains. J Biol Chem *282*, 16612–16622.

Naslavsky, N., McKenzie, J., Altan-Bonnet, N., Sheff, D., and Caplan, S. (2009). EHD3 regulates early-endosome-to-Golgi transport and preserves Golgi morphology. J Cell Sci *122*, 389–400.

Nickels, J.D., Smith, J.C., and Cheng, X. (2015). Lateral organization, bilayer asymmetry, and inter-leaflet coupling of biological membranes. Chem. Phys. Lipids *192*, 87–99.

Niemann, H.H., Knetsch, M.L.W., Scherer, A., Manstein, D.J., and Kull, F.J. (2001). Crystal structure of a dynamin GTPase domain in both nucleotide-free and GDP-bound forms. EMBO J. *20*, 5813–5821.

O'Donnell, J.P., Cooley, R.B., Kelly, C.M., Miller, K., Andersen, O.S., Rusinova, R., and Sondermann, H. (2017). Timing and Reset Mechanism of GTP Hydrolysis-Driven Conformational Changes of Atlastin. Struct. Lond. Engl. 1993 *25*, 997–1010.e4.

Osellame, L.D., Singh, A.P., Stroud, D.A., Palmer, C.S., Stojanovski, D., Ramachandran, R., and Ryan, M.T. (2016). Cooperative and independent roles of the Drp1 adaptors Mff, MiD49 and MiD51 in mitochondrial fission. J. Cell Sci. *129*, 2170–2181.

Paduch, M., Jeleń, F., and Otlewski, J. (2001). Structure of small G proteins and their regulators. Acta Biochim. Pol. *48*, 829–850.

Pant, S., Sharma, M., Patel, K., Caplan, S., Carr, C.M., and Grant, B.D. (2009). AMPH-1/Amphiphysin/Bin1 functions with RME-1/Ehd1 in endocytic recycling. Nat Cell Biol *11*, 1399–1410.

Paoluzi, S., Castagnoli, L., Lauro, I., Salcini, A.E., Coda, L., Fre', S., Confalonieri, S., Pelicci, P.G., Fiore, P.P.D., and Cesareni, G. (1998). Recognition specificity of individual EH domains of mammals and yeast. EMBO J *17*, 6541–6550.

Park, M. (2004). Recycling Endosomes Supply AMPA Receptors for LTP. Science *305*, 1972–1975.

Park, S.Y., Ha, B.G., Choi, G.H., Ryu, J., Kim, B., Jung, C.Y., and Lee, W. (2004). EHD2 interacts with the insulin-responsive glucose transporter (GLUT4) in rat adipocytes and may participate in insulin-induced GLUT4 recruitment. Biochemistry (Mosc.) *43*, 7552–7562.

Parton, R.G., and Collins, B.M. (2016). Unraveling the architecture of caveolae. Proc. Natl. Acad. Sci. *113*, 14170–14172.

Pettersen, E.F., Goddard, T.D., Huang, C.C., Couch, G.S., Greenblatt, D.M., Meng, E.C., and Ferrin, T.E. (2004). UCSF Chimera--a visualization system for exploratory research and analysis. J Comput Chem *25*, 1605–1612.

Picciano, J.A., Ameen, N., Grant, B.D., and Bradbury, N.A. (2003). Rme-1 regulates the recycling of the cystic fibrosis transmembrane conductance regulator. AJP Cell Physiol. *285*, C1009–C1018.

Posey, A.D., Pytel, P., Gardikiotes, K., Demonbreun, A.R., Rainey, M., George, M., Band, H., and McNally, E.M. (2011). Endocytic recycling proteins EHD1 and EHD2 interact with fer-1-like-5 (Fer1L5) and mediate myoblast fusion. J Biol Chem *286*, 7379–7388.

Praefcke, G.J.K., and McMahon, H.T. (2004). The dynamin superfamily: universal membrane tubulation and fission molecules? Nat Rev Mol Cell Biol *5*, 133–147.

Prakash, B., Praefcke, G.J.K., Renault, L., Wittinghofer, A., and Herrmann, C. (2000). Structure of human guanylate-binding protein 1 representing a unique class of GTP-binding proteins. Nature *403*, 567–571.

Pufall, M.A., and Graves, B.J. (2002). Autoinhibitory domains: modular effectors of cellular regulation. Annu. Rev. Cell Dev. Biol. *18*, 421–462.

Ramachandran, R., Pucadyil, T.J., Liu, Y.-W., Acharya, S., Leonard, M., Lukiyanchuk, V., and Schmid, S.L. (2009). Membrane Insertion of the Pleckstrin Homology Domain Variable Loop 1 Is Critical for Dynamin-catalyzed Vesicle Scission. Mol. Biol. Cell *20*, 4630–4639.

Rao, Y., Ma, Q., Vahedi-Faridi, A., Sundborger, A., Pechstein, A., Puchkov, D., Luo, L., Shupliakov, O., Saenger, W., and Haucke, V. (2010). Molecular basis for SH3 domain regulation of F-BAR-mediated membrane deformation. Proc Natl Acad Sci U A *107*, 8213–8218.

Rennie, M.L., McKelvie, S.A., Bulloch, E.M., and Kingston, R.L. (2014). Transient dimerization of human MxA promotes GTP hydrolysis, resulting in a mechanical power stroke. Structure *22*, 1433–1445.

Reubold, T.F., Eschenburg, S., Becker, A., Leonard, M., Schmid, S.L., Vallee, R.B., Kull, F.J., and Manstein, D.J. (2005). Crystal structure of the GTPase domain of rat dynamin 1. Proc Natl Acad Sci U A *102*, 13093–13098.

Reubold, T.F., Faelber, K., Plattner, N., Posor, Y., Ketel, K., Curth, U., Schlegel, J., Anand, R., Manstein, D.J., Noe, F., et al. (2015). Crystal structure of the dynamin tetramer. Nature *525*, 404–408.

Ross, J.L., Ali, M.Y., and Warshaw, D.M. (2008). Cargo transport: molecular motors navigate a complex cytoskeleton. Curr. Opin. Cell Biol. *20*, 41–47.

Roux, A., Uyhazi, K., Frost, A., and Camilli, P.D. (2006). GTP-dependent twisting of dynamin implicates constriction and tension in membrane fission. Nature *441*, 528–531.

Salcini, A.E., Confalonieri, S., Doria, M., Santolini, E., Tassi, E., Minenkova, O., Cesareni, G., Pelicci, P.G., and Fiore, P.P.D. (1997). Binding specificity and in vivo targets of the EH domain, a novel protein-protein interaction module. Genes Dev *11*, 2239–2249.

Saraste, M., Sibbald, P.R., and Wittinghofer, A. (1990). The P-loop--a common motif in ATP- and GTP-binding proteins. Trends Biochem Sci *15*, 430–434.

Scheffzek, K., and Welti, S. (2012). Pleckstrin homology (PH) like domains - versatile modules in protein-protein interaction platforms. FEBS Lett. *586*, 2662–2673.

Scheffzek, K., Ahmadian, M.R., Kabsch, W., Wiesmüller, L., Lautwein, A., Schmitz, F., and Wittinghofer, A. (1997). The Ras-RasGAP complex: structural basis for GTPase activation and its loss in oncogenic Ras mutants. Science *277*, 333–338.

Schulte, K., Pawlowski, N., Faelber, K., Fr?hlich, C., Howard, J., and Daumke, O. (2016). The immunity-related GTPase Irga6 dimerizes in a parallel head-to-head fashion. BMC Biol. *14*.

Sengupta, S., George, M., Miller, K.K., Naik, K., Chou, J., Cheatham, M.A., Dallos, P., Naramura, M., Band, H., and Zheng, J. (2009). EHD4 and CDH23 Are Interacting Partners in Cochlear Hair Cells. J. Biol. Chem. *284*, 20121–20129.

Senju, Y., Rosenbaum, E., Shah, C., Hamada-Nakahara, S., Itoh, Y., Yamamoto, K., Hanawa-Suetsugu, K., Daumke, O., and Suetsugu, S. (2015). Phosphorylation of PACSIN2 by protein kinase C triggers the removal of caveolae from the plasma membrane. J Cell Sci *128*, 2766–2780.

Shah, C., Hegde, B.G., Moren, B., Behrmann, E., Mielke, T., Moenke, G., Spahn, C.M., Lundmark, R., Daumke, O., and Langen, R. (2014). Structural insights into membrane interaction and caveolar targeting of dynamin-like EHD2. Structure *22*, 409–420.

Shao, Y., Akmentin, W., Toledo-Aral, J.J., Rosenbaum, J., Valdez, G., Cabot, J.B., Hilbush, B.S., and Halegoua, S. (2002). Pincher, a pinocytic chaperone for nerve growth factor/TrkA signaling endosomes. J Cell Biol *157*, 679–691.

Sharma, M., Naslavsky, N., and Caplan, S. (2008). A role for EHD4 in the regulation of early endosomal transport. Traffic *9*, 995–1018.

Sharma, M., Giridharan, S.S., Rahajeng, J., Naslavsky, N., and Caplan, S. (2009). MICAL-L1 links EHD1 to tubular recycling endosomes and regulates receptor recycling. Mol Biol Cell *20*, 5181–5194.

Simone, L.C., Caplan, S., and Naslavsky, N. (2013). Role of Phosphatidylinositol 4,5-Bisphosphate in Regulating EHD2 Plasma Membrane Localization. PLoS ONE *8*, e74519.

Smith, C.A. (2004). The Cell Fate Determinant Numb Interacts with EHD/Rme-1 Family Proteins and Has a Role in Endocytic Recycling. Mol. Biol. Cell *15*, 3698–3708.

Soulet, F., Yarar, Defne, Marilyn, Leonard, and Schmid, S.L. (2005). SNX9 Regulates Dynamin Assembly and Is Required for Efficient Clathrin-mediated Endocytosis. Mol. Biol. Cell *16*, 2058–2067.

Srinivasan, S., Dharmarajan, V., Reed, D.K., Griffin, P.R., and Schmid, S.L. (2016). Identification and function of conformational dynamics in the multidomain GTPase dynamin. EMBO J. *35*, 443–457.

Steven, A.C., Baumeister, W., Johnson, L.N., and Perham, R.N. (2016). Molecular biology of assemblies and machines (New York, NY: Garland Science).

Stoeber, M., Stoeck, I.K., Hanni, C., Bleck, C.K., Balistreri, G., and Helenius, A. (2012). Oligomers of the ATPase EHD2 confine caveolae to the plasma membrane through association with actin. EMBO J *31*, 2350–2364.

Stowell, M.H., Marks, B., Wigge, P., and McMahon, H.T. (1999). Nucleotide-dependent conformational changes in dynamin: evidence for a mechanochemical molecular spring. Nat Cell Biol *1*, 27–32.

Sundborger, A.C., and Hinshaw, J.E. (2014). Regulating dynamin dynamics during endocytosis. F1000Prime Rep. *6*.

Sundborger, A., Fang, S., Heymann, J., Ray, P., Chappie, J., and Hinshaw, J. (2014). A Dynamin Mutant Defines a Superconstricted Prefission State. Cell Rep. *8*, 734–742.

Sweitzer, S.M., and Hinshaw, J.E. (1998). Dynamin undergoes a GTP-dependent conformational change causing vesiculation. Cell *93*, 1021–1029.

Takei, K., McPherson*, P.S., Schmid, S.L., and Camilli, P.D. (1995). Tubular membrane invaginations coated by dynamin rings are induced by GTP-γS in nerve terminals. Nature *374*, 186–190.

Trudeau, T., Nassar, R., Cumberworth, A., Wong, E.T.C., Woollard, G., and Gsponer, J. (2013). Structure and Intrinsic Disorder in Protein Autoinhibition. Structure *21*, 332–341.

Vetter, I.R., and Wittinghofer, A. (2001). The guanine nucleotide-binding switch in three dimensions. Science *294*, 1299–1304.

Wang, Q., Navarro, M.V.A.S., Peng, G., Molinelli, E., Goh, S.L., Judson, B.L., Rajashankar, K.R., and Sondermann, H. (2009). Molecular mechanism of membrane constriction and tubulation mediated by the F-BAR protein Pacsin/Syndapin. Proc Natl Acad Sci U A *106*, 12700–12705.

Wang, S., Tukachinsky, H., Romano, F.B., and Rapoport, T.A. (2016). Cooperation of the ER-shaping proteins atlastin, lunapark, and reticulons to generate a tubular membrane network. eLife *5*.

Watson, H. (2015). Biological membranes. Essays Biochem. *59*, 43–69.

Wenger, J., Klinglmayr, E., Fröhlich, C., Eibl, C., Gimeno, A., Hessenberger, M., Puehringer, S., Daumke, O., and Goettig, P. (2013). Functional Mapping of Human Dynamin-1-Like GTPase Domain Based on X-ray Structure Analyses. PLoS ONE *8*, e71835.

Wilman, H.R., Shi, J., and Deane, C.M. (2014). Helix kinks are equally prevalent in soluble and membrane proteins: Helix Kinks in Soluble and Membrane Helices. Proteins Struct. Funct. Bioinforma. *82*, 1960–1970.

Wu, F., Hu, X., Bian, X., Liu, X., and Hu, J. (2015). Comparison of human and Drosophila atlastin GTPases. Protein Cell *6*, 139–146.

Xu, B., Kong, J., Wang, X., Wei, W., Xie, W., and Yu, X.-F. (2015). Structural insight into the assembly of human anti-HIV dynamin-like protein MxB/Mx2. Biochem. Biophys. Res. Commun. *456*, 197–201.

Xu, Y., Shi, H., Wei, S., Wong, S.H., and Hong, W. (2004). Mutually exclusive interactions of EHD1 with GS32 and Syndapin II. Mol. Membr. Biol. *21*, 269–277.

Yan, L., Ma, Y., Sun, Y., Gao, J., Chen, X., Liu, J., Wang, C., Rao, Z., and Lou, Z. (2011). Structural basis for mechanochemical role of Arabidopsis thaliana dynamin-related protein in membrane fission. J. Mol. Cell Biol. *3*, 378–381.

Yan, L., Sun, S., Wang, W., Shi, J., Hu, X., Wang, S., Su, D., Rao, Z., Hu, J., and Lou, Z. (2015). Structures of the yeast dynamin-like GTPase Sey1p provide insight into homotypic ER fusion. J. Cell Biol. *210*, 961–972.

Zheng, J., Cahill, S.M., Lemmon, M.A., Fushman, D., Schlessinger, J., and Cowburn, D. (1996). Identification of the Binding Site for Acidic Phospholipids on the PH Domain of Dynamin: Implications for Stimulation of GTPase Activity. J. Mol. Biol. *255*, 14–21.

# Acknowledgments

I would like to thank Oliver Daumke for the opportunity, supervision and patience during this journey. He recruited me and trust me with such a challenging project. Working with him was an incredible time and a great learning period. Many thanks to the whole Daumke and Heinemann lab for all their support and contributions.

Special thanks to Vivian, with whom I had a great experience and could face many challenges. She was essential during all this work. Many thanks to Chris van Hoorn, a great friend with whom I had an amazing time in the lab. He taught me many things and his presence made the lab always a pleasant place. Working with these two was definitely one of the highlights of my stay in the Daumke lab. Also, many thanks to Elena for working so hard, for being so patient and kind during all moments.

Many thanks to Manuel and Marie, with whom I shared the office and the lab all these years. We had many great discussions which contributed to my scientific and personal development. Also, they help me so many times and made my stay in Berlin and in the lab much more pleasant.

Many thanks to Daniel, Alexej and Jeff for all the nice moments and all their contributions to this project, their nice tips were always very helpful.

Thanks to my lovely wife, no words can describe your contributions to my life and to this work. Many thanks to my family for everything they have done and all their support at all times.